

Fatigue Behavior of Multi-Spot Welded Joints in Thermoplastic Composites

Effects of Spot Arrangement in a Four-Spot Joint

C.A. Meijerman

Delft University of Technology

Fatigue Behavior of Multi-Spot Welded Joints in Thermoplastic Composites

Effects of Spot Arrangement in a Four-Spot Joint

by

C.A. Meijerman

in fulfillment of the requirements for the degree of

Master of Science
in Aerospace Engineering

at the Delft University of Technology
to be defended publicly on Friday January 15th, 2021 at 2:00 PM.

Thesis committee:	Dr. C.D. Rans	TU Delft, Chairholder
	Dr. I. Fernandez Villegas	TU Delft, Daily supervisor
	Dr. J.J.E. Teuwen	TU Delft
	Dr.-Ing. S.G.P. Castro	TU Delft

An electronic version of this thesis is available at <http://repository.tudelft.nl/>.

Acknowledgments

Where do I even begin...

In all fairness, I should be thanking every single person who has entered my life at any point and helped shape me into the person that I am today. Lucky as I may count myself, these are far too many names to list here and I will therefore only highlight the most important ones below.

I want to extend my deepest gratitude to my parents Marga and Bert who, during these challenging times, made me realize what unconditional love and support feels like. Likewise, I want to thank Arie and Anja who have come to feel like second family to me over these past years. It is heartwarming to know how all you wish for me is to find happiness in the adventures that are yet to come, and my deepest wish is that I get to give back a lot of happiness and positivity in doing so!

A huge thanks goes out to both my supervisors. Calvin, for making me see how 'ruined' data can still easily lead to valuable findings if only you think outside the box a little more. Irene, for sharing with me her passion for welding and for including me in all the goings-on of the welding group. Both of you, for showing me support and kindness at times when circumstances were tough.

I want to thank Dave for everything he has done for me in the lab. Together we have fought the dreaded I/O error many times (22 times! I have had to report them all) and we have had many good chats during my time in the lab. I should of course thank my study friends, for providing me with some well-needed coffee breaks and questionable music advice. An honorable mention goes out to Linda, who has read more of my report than almost anyone else and has been giving me on-point feedback every time.

Lastly, I want to thank the person who has been keeping me sane for all this time. Hugo, you have been right there with me through it all, cheering me on during the highs and pulling me through the lows. I am so grateful for your endless patience and support and for having you in my life. I cannot wait until we will finally get to celebrate this one as well!

Krista Meijerman
Delft, December 2020

Contents

Summary	v
List of Figures	vi
List of Tables	ix
Nomenclature	x
1 Introduction	1
2 Theoretical Background	2
2.1 Welding of thermoplastic composites	2
2.1.1 Advantages over traditional joining methods	2
2.1.2 Existing techniques	3
2.1.3 State of commercial application	3
2.2 Ultrasonic welding	4
2.2.1 Main principles and components	4
2.2.2 Process parameters	5
2.2.3 Determination of optimum process parameters	5
2.2.4 Control strategy for multi-spot welding	7
2.3 Fatigue of single lap joints	7
2.3.1 Structural design concepts	8
2.3.2 Arrangement effects in multi-spot welded steel joints	10
3 Research Definition	12
3.1 Problem statement	12
3.2 Scope and research questions	13
3.3 Hypotheses	14
3.3.1 Fatigue life	14
3.3.2 Failure modes	14
3.3.3 Damage evolution	14
4 Methodology	17
4.1 Geometries, test matrix and nomenclature	17
4.2 Specimen production	18
4.2.1 Manufacturing of adherends	18
4.2.2 Ultrasonic spot welding	19
4.3 Experimental test methods	20
4.3.1 Static failure load determination	20
4.3.2 Fatigue testing	21
4.4 Data acquisition and processing	23
4.4.1 Microscopy and image processing	23
4.4.2 Cyclic load and displacement data	25
4.4.3 Digital image correlation	25

5	Results	28
5.1	Surface microscopy	29
5.2	Quasi-static test results	32
5.3	Fatigue test results	32
5.3.1	Fatigue life	32
5.3.2	Cyclic load and displacement data	33
5.3.3	Digital image correlation	39
5.4	Single spot weld laminate comparison	45
6	Discussion	46
6.1	Weld quality and consistency	46
6.1.1	Laminate variations and effects	46
6.1.2	Control strategy transferability	49
6.1.3	Main findings	51
6.2	Initial damage in column joints	51
6.3	Fatigue behavior of four-spot welded joints	54
6.3.1	Fatigue life	54
6.3.2	Failure modes	55
6.3.3	Damage evolution	58
6.3.4	Comparison to steel joints	63
7	Conclusions and Recommendations	65
7.1	Conclusions	65
7.2	Recommendations	67
	Bibliography	68
A	Fracture Surfaces and Welded Areas	71
B	Out-of-Plane Displacement at Spot Locations over Time	78

Summary

Welding is a joining method for thermoplastic composites that offers multiple advantages over the more traditional methods of mechanical fastening and adhesive bonding. A particularly promising welding technique is ultrasonic welding, which features very short process times as a result of the high heating rates that can be achieved. This welding technique is not yet being applied commercially, but is hypothesized to offer potential for improved damage tolerance over the more commonly used induction and resistance welding.

Both are continuous welding techniques, whereas ultrasonic welding is traditionally a spot welding technique. In a multi-spot welded joint, evolving damage will need to re-initiate in subsequent spots. This provides the joint with a potentially damage-arresting feature: the fact that damage initiation will need to occur multiple times might delay overall damage evolution through the joint compared to a continuous welded joint, where damage initiation needs to occur only once.

This work is a first exploratory step into the domain of fatigue of multi-spot welded joints in thermoplastic composites. Existing research on the fatigue behavior of four-spot welded steel joints in various layouts serves as the main reference throughout this research: the methodology from this research is transferred to four-spot welded joints in thermoplastic composites.

By comparing fatigue behavior across both materials, it is evaluated to what extent existing knowledge and design rules for steel could potentially be transferred to thermoplastic composites. In future work, this research could be expanded upon and damage tolerance behavior could be explored by repeating these experiments with damage artificially introduced into the joints.

Differences were observed in the results obtained for thermoplastic composite and steel joints. Most notably, in steel joints the dominant failure mode was seen to change from spot fracture to sheet fracture at higher fatigue lives. In thermoplastic composites, the joints consistently showed spot fracture across all load levels. A different interrelation between layout performances was seen in the steel and thermoplastic composite joints, assumed to be a result of localized material strengthening in the steel joints from interference of adjacent heat-affected zones. These results indicate that existing knowledge on multi-spot welded joints in steel cannot be readily transferred to thermoplastic composites, as failure modes and material mechanisms may differ.

It was discovered that, when one spot failed prematurely as a result of existing damage in the joint, the remaining layout no longer seemed to have an effect on fatigue life performance. This is expected to be a result of asymmetry in the remaining joint layout, as one spot would always become a preferred location for damage initiation and subsequent evolution. Therefore, subsequent damage evolution would only be restricted by that one spot, up to the point where the shear strength of the joint was exceeded.

For any future work, a recommendation is made to repeat the performed experiments at a lower load level and artificially introduce damage into the joint. This way, the path of damage evolution can be monitored as damage progresses through more spots subsequently, before the shear strength of the joint is ultimately exceeded. In monitoring this path of damage evolution and the time spent between crack initiation and propagation, the damage-arresting potential of multi-spot welded joints can be truly explored.

List of Figures

2	Theoretical Background	2
2.1	Diffusion of polymer chains across the weld interface.	2
2.2	Classification of welding techniques according to heating mechanism.	3
2.3	Schematic of the main ultrasonic welding process components.	4
2.4	Example power and displacement curves for the ultrasonic welding process.	6
2.5	Stages in the welding process and their power and displacement characteristics.	6
2.6	The three modes of crack opening.	8
2.7	Example of a typical stress-life curve.	9
2.8	Geometries of the steel spot welded specimens tested for fatigue life.	10
2.9	Stress-life curves for different four-spot arrangements in steel welded joints.	11
3	Research Definition	12
3.1	Schematic images of a four-spot column, row and square joint layout.	13
3.2	Predicted path of damage evolution for ideal spot welds.	15
3.3	Predicted damage evolution due to spot weld imperfection.	15
4	Methodology	17
4.1	Geometries of the spot welded fatigue life specimens.	18
4.2	Spot weld numbering conventions.	19
4.3	Structure of a 5-harness satin weave.	19
4.4	Press control cycle for consolidation of CF/PPS laminates.	19
4.5	Schematic of the used welding setup.	20
4.6	Bolt-tightened clamps as used for fatigue testing.	22
4.7	Sandpaper mesh used for grip tabs.	22
4.8	Welded area determination using the Keyence VR-5000 microscope and ImageJ.	23
4.9	Schematic representation of warpage in a rectangular plate.	24
4.10	Height image obtained from the Keyence VR-5000, indicating warpage.	24
4.11	Angle of misalignment ϕ between two line segments.	24
4.12	Steps in cleaning up the raw peak-valley load and displacement data.	26
4.13	Example line graph showing out-of-plane displacement.	27
4.14	Example graph showing out-of-plane displacement at spot locations over time.	27
5	Results	28
5.1	Welded areas as derived from microscopy images, split out into individual spots.	29
5.2	Example roughness image of a deeper-than-usual circular imprint.	30
5.3	Welded area by spot weld location for the three different joint layouts.	30
5.4	Warp angle of the top and bottom adherends of each specimen.	31
5.5	Load-displacement curves of the quasi-static test specimens.	32
5.6	Stress-life diagram showing all three joint layouts.	33
5.7	Effect of machine downtime, resulting from incidental network errors.	34
5.8	Effect of a low DIC interval on peak displacement values.	34
5.9	Shape comparison of cyclic displacement data to base CF/PPS material.	35
5.10	Cyclic peak load and displacement data – C_FL1.	35
5.11	Cyclic peak load and displacement data – C_FL2.	36
5.12	Cyclic peak load and displacement data – C_FL3.	36
5.13	Cyclic peak load and displacement data – R_FL1.	37
5.14	Cyclic peak load and displacement data – R_FL2.	37
5.15	Cyclic peak load and displacement data – S_FL1.	38

5.16	Cyclic peak load and displacement data – S_FL2.	38
5.17	Out-of-plane displacement with time over longitudinal center-line – C_FL2.	39
5.18	Out-of-plane displacement with time over longitudinal center-line – C_FL3.	39
5.19	Out-of-plane displacement with time over transverse center-line – R_FL1.	40
5.20	Out-of-plane displacement with time over transverse center-line – R_FL2.	40
5.21	Out-of-plane displacement with time over longitudinal line (s2, s4) – S_FL1.	41
5.22	Out-of-plane displacement with time over longitudinal line (s1, s3) – S_FL1.	41
5.23	Out-of-plane displacement with time over transverse line (s1, s2) – S_FL1.	42
5.24	Out-of-plane displacement with time over transverse line (s3, s4) – S_FL1.	42
5.25	Out-of-plane displacement with time over longitudinal line (s2, s4) – S_FL2.	43
5.26	Out-of-plane displacement with time over longitudinal line (s1, s3) – S_FL2.	43
5.27	Out-of-plane displacement with time over transverse line (s1, s2) – S_FL2.	44
5.28	Out-of-plane displacement with time over transverse line (s3, s4) – S_FL2.	44
5.29	Load-displacement data of the single spot welds used for laminate comparison.	45
6	Discussion	46
6.1	Visual comparison between single spot welds on the three laminates.	47
6.2	Welded area versus warp angle for all four-spot welded specimens.	49
6.3	Welded area versus warp angle, split by layout and individual spots.	50
6.4	Dissipated welding energy versus welded area.	51
6.5	Total welding time versus welded area.	51
6.6	Quasi-static load-displacement graph of the column specimen.	52
6.7	Column: Out-of-plane displacement with increasing load at spot locations.	53
6.8	Column: Out-of-plane displacement with increasing load over longitudinal center-line.	53
6.9	Fatigue life diagram with linear regression line for the column specimens.	54
6.10	Fracture surfaces encountered in s1 of column joints tested under various conditions.	56
6.11	Roughness image of a spot that underwent quasi-static testing.	56
6.12	Roughness image of a spot that underwent quasi-static testing with regular pausing.	57
6.13	Roughness image of a spot that underwent cyclic testing with regular pausing.	57
6.14	Peak displacement during the final 2,000 cycles of column specimen lifetime.	58
6.15	Overview images of the fracture surfaces of the column specimens.	59
6.16	Peak displacement during the final 2,000 cycles of row specimen lifetime.	60
6.17	Overview images of the fracture surfaces of the row specimens.	61
6.18	Peak displacement during the final 5,000 cycles of square specimen lifetime.	62
6.19	Overview images of the fracture surfaces of the square specimens.	62
6.20	Side-by-side stress-life diagrams for steel and TPC adherends.	63
A	Fracture Surfaces and Welded Areas	71
A.1	Fracture surfaces and welded areas – C_SF.	71
A.2	Fracture surfaces and welded areas – C_FL1.	71
A.3	Fracture surfaces and welded areas – C_FL2.	72
A.4	Fracture surfaces and welded areas – C_FL3.	72
A.5	Fracture surfaces and welded areas – C_FLx1.	73
A.6	Fracture surfaces and welded areas – R_SF.	73
A.7	Fracture surfaces and welded areas – R_FL1.	74
A.8	Fracture surfaces and welded areas – R_FL2.	74
A.9	Fracture surfaces and welded areas – S_SF.	75
A.10	Fracture surfaces and welded areas – S_FL1.	75
A.11	Fracture surfaces and welded areas – S_FL2.	76
A.12	Fracture surfaces and welded areas – S_FLx1.	76
A.13	Fracture surfaces and welded areas – S_FLx2.	77
A.14	Fracture surfaces and welded areas – S_TU.	77

B	Out-of-Plane Displacement at Spot Locations over Time	78
B.1	Out-of-plane displacement at spot locations over time – C_FL2.	78
B.2	Out-of-plane displacement at spot locations over time – C_FL3.	78
B.3	Out-of-plane displacement at spot locations over time – R_FL1.	79
B.4	Out-of-plane displacement at spot locations over time – R_FL2.	79
B.5	Out-of-plane displacement at spot locations over time – S_FL1.	80
B.6	Out-of-plane displacement at spot locations over time – S_FL2.	80

List of Tables

4	Methodology	17
4.1	Performed number and type of tests per joint layout.	18
4.2	Control parameter values for sequential ultrasonic welding.	21
5	Results	28
5.1	Overview of available results for all tested specimens.	28
5.2	Summarized welded areas and warp angles as derived from microscopy images.	31
5.3	Quasi-static test results.	32
5.4	Imposed maximum load and shear stress and resulting number of cycles to failure.	33
5.5	Occurrences of network errors and resulting machine downtime.	34
5.6	Summary of single spot weld test results.	45
6	Discussion	46
6.1	Thickness and warp angle of four-spot joint specimens: mean and standard deviation.	48

Nomenclature

Roman Symbols

d	Displacement	mm
h	Height	mm
JS	Joint stiffness	N/mm
P	Applied load	N
P_{max}	Maximum applied cyclic load	N
P_{ult}	Ultimate load	N
w	Out-of-plane displacement	mm
w	Width	mm
WA	Welded area	mm ²
x	Transverse coordinate	mm
y	Longitudinal coordinate	mm
z	Out-of-plane coordinate	mm

Greek Symbols

ϕ	Angle of misalignment	°
τ_{max}	Maximum applied cyclic shear stress	MPa
τ_{ult}	Shear strength	MPa
θ	Warp angle	°/m

Abbreviations

CF	Carbon fiber
DIC	Digital image correlation
ED	Energy director
GF	Glass fiber
PPS	Polyphenylene sulfide
SERR	Strain energy release rate
TPC	Thermoplastic composite
TSC	Thermoset composite

1

Introduction

Optimizing structural weight is a vital consideration in aircraft design: by eliminating any unnecessary structural weight, the amount of fuel that is consumed every flight is minimized. This, in turn, reduces operating costs for airlines and emissions of greenhouse gasses such as CO₂ and NO_x. Reduction of emissions is an especially important consideration in the current time and day, where global efforts are being made to reduce human-induced CO₂ emissions. It is estimated that commercial aviation is currently responsible for about 2.4% of these global emissions, which in 2018 alone amounted to 918 million tonnes of CO₂ emissions [1].

The potential for weight reduction has been an important driver for the use of fiber-reinforced polymer composites (referred to as composites from this point onward) in aircraft design. Owing to the high directionality that can be achieved and the excellent mechanical performance of reinforcement materials, composites show superior strength- and stiffness-to-weight ratios over conventional aerospace materials. Showcasing the advances in composite technology, both the Boeing 787 and Airbus A350 XWB have composites amounting to about 50% of their total weight [2, 3].

The category of polymers most commonly used for aircraft composites are thermosets. This type of polymer forms an irreversible, cross-linked molecular structure when fully cured. A limitation of this type of molecular structure is that it prevents cured thermoset composite (TSC) parts from being reprocessed. An alternative that is being used increasingly is offered by thermoplastic composites (TPCs). Contrary to TSCs, TPCs do not experience cross-linking of molecule chains, which means they can be reshaped through softening or melting.

TPCs offer various advantages over TSCs. Examples are an infinite prepreg shelf life, more cost-effective manufacturing, improved damage tolerance and increased recyclability [4–7]. One of the most important advantages, however, is the fact that TPCs can be joined through welding. This is a powerful joining method that does not require drilling holes in the adherends or depend on principles of adhesion. An especially interesting welding technique is sequential ultrasonic welding, which features a low energy consumption and short process times.

Since ultrasonic welding is traditionally a spot welding technique, it is expected to offer an improvement over continuous welding techniques, such as the commonly used induction and resistance welding, in the area of damage tolerance. As opposed to continuous welded seams, in a multi-spot welded joint evolving damage will have to re-initiate in each spot. Depending on the exact fatigue behavior, this characteristic might delay overall damage evolution through the joint.

The main goal of this research is to explore the potential of multi-spot joint design in lap shear joints for damage evolution delay under cyclic loading. To this end, the effects of spot arrangement on fatigue behavior are evaluated experimentally and it is investigated to what extent relevant existing knowledge on multi-spot welded joints on steel adherends can be transferred to composites.

The main body of this report has been divided into multiple chapters. First, Chapter 2 provides an overview of the theoretical background and advances in current literature that are relevant to this research. Chapter 3 identifies the problem statement and translates this into a research definition. In Chapter 4, the complete methodology regarding manufacturing, experimental testing and data acquisition is addressed. Results of experimental testing are presented in Chapter 5 and subsequently discussed in Chapter 6. Finally, conclusions and recommendations regarding future work can be found in Chapter 7.

This chapter provides the reader with a summary of the main topics and advances in recent literature that are relevant to this research. First, Section 2.1 addresses the relevance and current level of maturity of TPC welding in general. Section 2.2 then describes ultrasonic welding in more detail, since this technique was identified as a potentially promising approach to joint damage tolerance and is the method of choice in this research. Damage tolerance itself and other structural design concepts relating to fatigue will be discussed in Section 2.3. This section will also briefly summarize relevant work regarding fatigue of multi-spot welded joints on steel adherends.

2.1. Welding of thermoplastic composites

Welding is a class of joining techniques for thermoplastic polymers and TPCs that is based on the principle of polymer healing. When a sufficient amount of heat is supplied to adherends that are in close contact, softening of the thermoplastic matrix will result in diffusion of polymer chains across the interface. This process of polymer diffusion is illustrated in Figure 2.1. It can be seen that, after diffusion and subsequent consolidation, the interface between the adherends has essentially been removed.

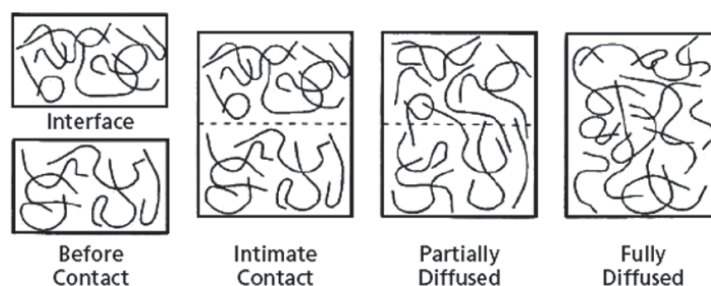


Figure 2.1: Diffusion of polymer chains across the weld interface [6].

Due to the nature of the process, welding is not suitable for joining of TSCs without the introduction of foreign materials at the interface: the cross-linked polymer structure of thermosets prevents softening and melting. For TPCs, however, welding has been found to offer many advantages over both mechanical fastening and adhesive bonding.

2.1.1. Advantages over traditional joining methods

Mechanical fastening is the joining of two or more parts with fasteners, such as rivets or bolts. This joining method can be used for any combination of materials. Many different types of mechanically fastened joints exist, varying with load cases and desired modes of load transfer.

At the moment, mechanical fastening is still a dominant method for joining primary structural composite parts [8]. However, the need to drill holes in the material makes this method less than ideal for composite joining. Drilling easily creates delaminations in the material, damages the reinforcing fibers and results in stress concentrations that locally weaken the structure. Other typical problems include, but are not limited to, a mismatch in thermal expansion coefficient between fastener and adherend and increased susceptibility to water ingress at the hole location [4, 5].

Adhesive bonding also faces problems when applied to TPCs. First of all, creating a high-quality adhesive bond is not straightforward. Proper surface preparation is required, as contaminants will decrease bond strength. In addition, most polymers used for engineering applications are chemically

inert, meaning that the adherend surface must first be treated to locally alter its chemical and physical properties before it can be adhesively bonded [9]. After bonding, adhesives need to cure before attaining their final design strength, which limits process speed.

Another problem that is frequently encountered in adhesively bonded joints is the so-called kissing bond: a defect at the interface that does not show visible separation between the adherends and the adhesive [10]. This type of defect going unnoticed during inspection is a dangerous thing, since the resulting decrease in joint strength may lead to premature failure. In general, certification of primary structural adhesively bonded joints is difficult, since the current knowledge and ability to predict disbond growth are limited [11].

Welding solves many of the aforementioned problems related to mechanical fastening and adhesive bonding. Most importantly, the need to drill holes in the adherends is eliminated and the required amounts of surface treatment and preparation are limited.

2.1.2. Existing techniques

Welding techniques are typically classified by their heating mechanism. Three main categories can be distinguished: thermal, friction and electromagnetic welding. Figure 2.2 shows the classification of the most common welding techniques according to their heating mechanisms.

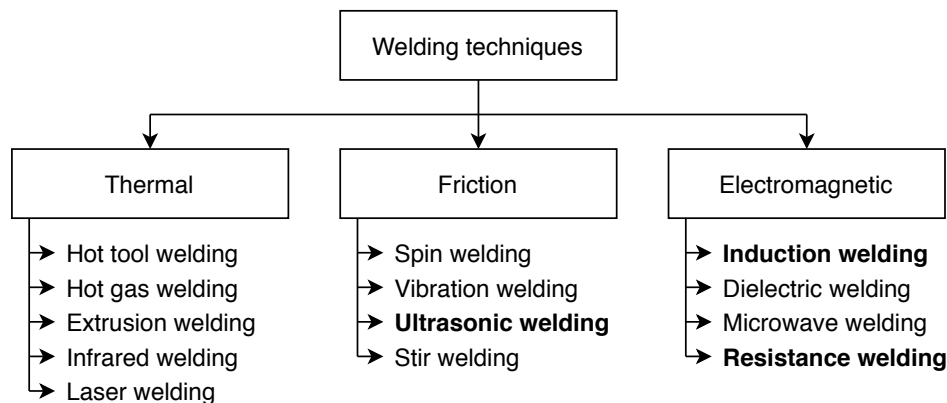


Figure 2.2: Classification of welding techniques according to heating mechanism [5].

Another distinction can be made between welding techniques, based on weld type. If a continuous seam is created the technique falls under continuous welding. Spot welding techniques, on the other hand, only join the adherends at discrete points.

Three techniques have been emphasized in Figure 2.2: ultrasonic, induction and resistance welding. These techniques are commonly regarded the most promising welding techniques for joining of TPCs [4, 12]. Out of these techniques both induction and resistance welding are continuous welding techniques, whereas only ultrasonic welding is traditionally a spot welding technique.

2.1.3. State of commercial application

At this moment, the use of TPCs in aircraft structures is still limited. Both the Boeing 787 and the Airbus A350 XWB, known for their extensive use of composites, predominantly use TSCs for their more primary structural applications [13]. Typical applications of TPCs in current commercial aircraft include clips, brackets, ceiling rails and stow bins [14]. There are, however, some noteworthy exceptions.

A major example is the fixed leading edge of the Airbus A380 wing, also known as the J-nose. This leading edge is made from glass fiber-reinforced polyphenylene sulfide (GF/PPS) that is joined through resistance welding: this same technology was used earlier for portions of the leading edges of the Airbus A340–500/600 [15].

TPCs have also been used for control surfaces on the tails of the Gulfstream G650 and Dassault F5X business jets: these parts are made from carbon fiber-reinforced PPS (CF/PPS). In order to avoid the hazard of current leakage in resistance welding of carbon fiber-reinforced composites, these control surfaces are joined through induction welding instead [15].

Contrary to induction and resistance welding, ultrasonic welding is not yet being used industrially for joining of structural aircraft components. Its high heating rates do allow creation of a simple ultrasonic spot weld in no more than a few seconds [16], which is a very short process time when compared to induction or resistance welding. For these continuous welding techniques, heating times generally lie in the range of 30 to 90 seconds [12, 17]. Additionally, no foreign material is needed at the weld interface when ultrasonic welding is used. Together, these advantages offer potential for ultrasonic welding as a method of choice over induction and resistance welding.

2.2. Ultrasonic welding

The previous section has highlighted the main advantages and opportunities offered by welding, and in particular ultrasonic spot welding, of TPCs. At this moment, there is still much that is not fully understood about the mechanisms of this welding technique. It is also important to note that, since adherends are joined at discrete points rather than over a continuous seam, the amount of welded area and therefore the ultimate failure load of an ultrasonically spot welded joint will typically be lower than that of a continuous weld created with induction or resistance welding.

However, due to the fact that evolving damage will have to re-initiate in subsequent spots, multi-spot welded joints are hypothesized to show an improvement over continuous welded seams in the area of damage tolerance. Since ultrasonic welding was the method of choice for creating multi-spot welded joints in this research, this section provides background information on all relevant aspects of this technique.

2.2.1. Main principles and components

A simple illustration of the ultrasonic welding setup is seen in Figure 2.3. The main components of the welding process are shown here: the adherends, which are the two composite parts that are to be joined, the sonotrode and the energy director (ED).

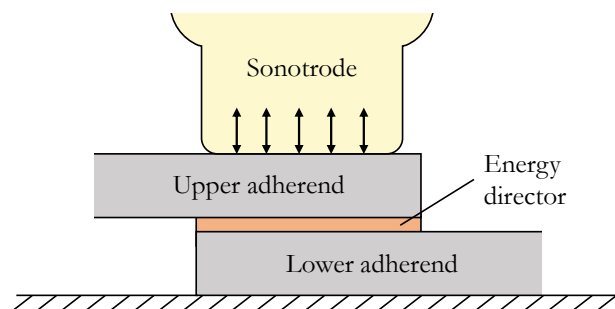


Figure 2.3: Schematic of the main ultrasonic welding process components [18].

The sonotrode, sometimes also called horn, vibrates up and down at ultrasonic frequencies while in intimate contact with the upper adherend. The vibration frequencies for typical commercial welders range from 20 to 50 kHz, at low amplitudes between $2.5 \mu\text{m}$ and 0.25 mm [16, 19]. The friction caused by these vibrations results in the generation of heat for welding: both through interfacial friction between the adherends and viscoelastic friction between the polymer molecules. Zhang et al. [20] showed that the initial heat generated during the welding process comes mostly from interfacial friction, whereas viscoelastic heating becomes dominant once the polymer reaches its glass transition temperature. This viscoelastic heating can achieve considerably higher heating rates

than heating through interfacial friction and is responsible for the majority of heat generation.

Apart from vibrating, the sonotrode applies the welding and consolidation force that are required during the vibration phase and consolidation phase, respectively. To maintain the required welding force during melting and flow of the ED, the sonotrode is allowed to displace downward.

During the entire welding process the sonotrode will periodically lose contact with the adherends: this phenomenon is called hammering. This loss of contact reduces heat generation and thus decreases process efficiency compared to the ideal case where the sonotrode is always in contact with the adherends. Palardy et al. [21] found that the hammering effect decreases towards the end of the welding cycle, and attributed this decrease to heating and localized melting of the ED at the interface. The resulting decrease in stiffness at the interface allows the upper adherend to follow the vibration of the sonotrode more closely, thus improving amplitude transmission.

The ED is a resin-rich piece of polymeric material, placed at the weld interface to ensure preferential heating at the interface. This is achieved through two forms of heat generation: surface friction between the ED and the adherends and viscoelastic heating as a result of higher cyclic strain in the ED compared to the adherends [22]. Once the ED reaches its glass transition temperature, its softened state results in faster, viscoelastic heating at the interface.

Traditional EDs are pre-molded onto the weld surface. These EDs are usually triangular or rectangular in shape [5]. Preferential heating due to a higher cyclic strain in this type of ED is guaranteed by the fact that it has a smaller cross-sectional area than the adherends [22].

An alternative to these traditional EDs was investigated by Villegas et al. [16]: the flat ED. This is a neat thermoplastic polymer film that is not pre-molded onto the adherend: instead, it is placed at the weld interface just before welding. The flat ED was found to simplify the welding process, while still resulting in consistent weld quality [23]. A significant part of the heat generation in flat EDs results from surface friction, while a higher cyclic strain in the ED is ensured by its lower stiffness compared to the adherends [18].

2.2.2. Process parameters

As was mentioned earlier ultrasonic welding is a friction welding technique, meaning that it relies on vibrations for heat generation. The process can be divided into two subsequent phases, each with its own set of process parameters: vibration and solidification.

The vibration phase encompasses the softening of the resin and subsequent diffusion of polymer chains across the weld interface. During this vibration phase the material is heated up as a result of the ultrasonic vibrations and pressure that are applied. The main process parameters for this phase are welding force and vibration frequency, amplitude and time [5, 24]. The vibration frequency is typically fixed for commercial ultrasonic welders [16]. The vibration time can be set directly, but it can also be imposed indirectly by defining a sonotrode displacement or amount of dissipated welding energy that must be reached.

In the solidification phase, vibrations are no longer applied: this allows the weld to cool down under continued applied pressure. For this phase, the process parameters that will affect the final weld quality are solidification force and solidification time [24].

2.2.3. Determination of optimum process parameters

In 2013, Villegas [16, 24] first investigated the subject of process monitoring during ultrasonic welding. The aim of this research was to gain a deeper understanding of the physical mechanisms that take place at the interface during welding and how these mechanisms relate to welding energy and sonotrode displacement throughout the welding process.

An example graph of power and sonotrode displacement during the vibration phase of the ultrasonic welding process is shown in Figure 2.4. Note that, in this graph, downward sonotrode displacement is depicted as positive.

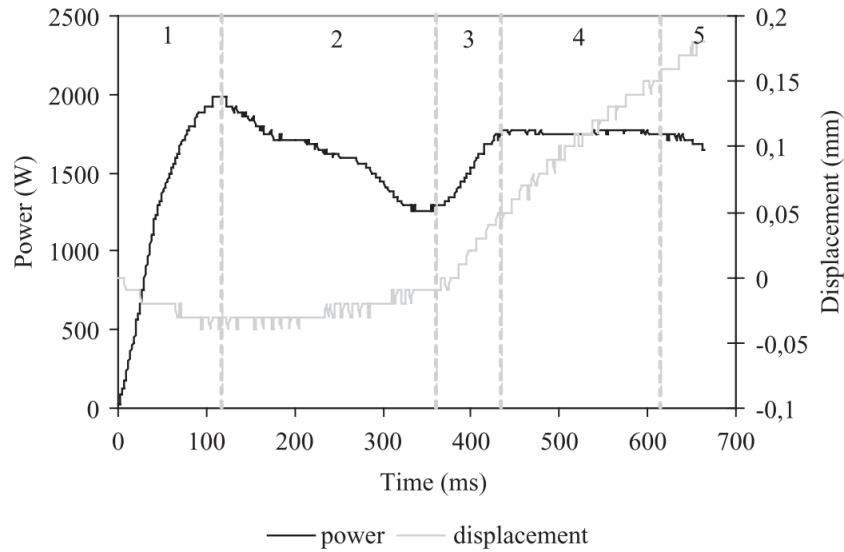


Figure 2.4: Example power and displacement curves of the ultrasonic welding process [16].

Five distinct stages, directly related to physical changes at the interface, can be identified: (1) heating of the ED, (2) localized melting of the ED, (3) a fully molten state of the ED, (4) further flow of the molten ED and (5) melting of the adherend resin. Each of these stages is addressed briefly in the overview in Figure 2.5.

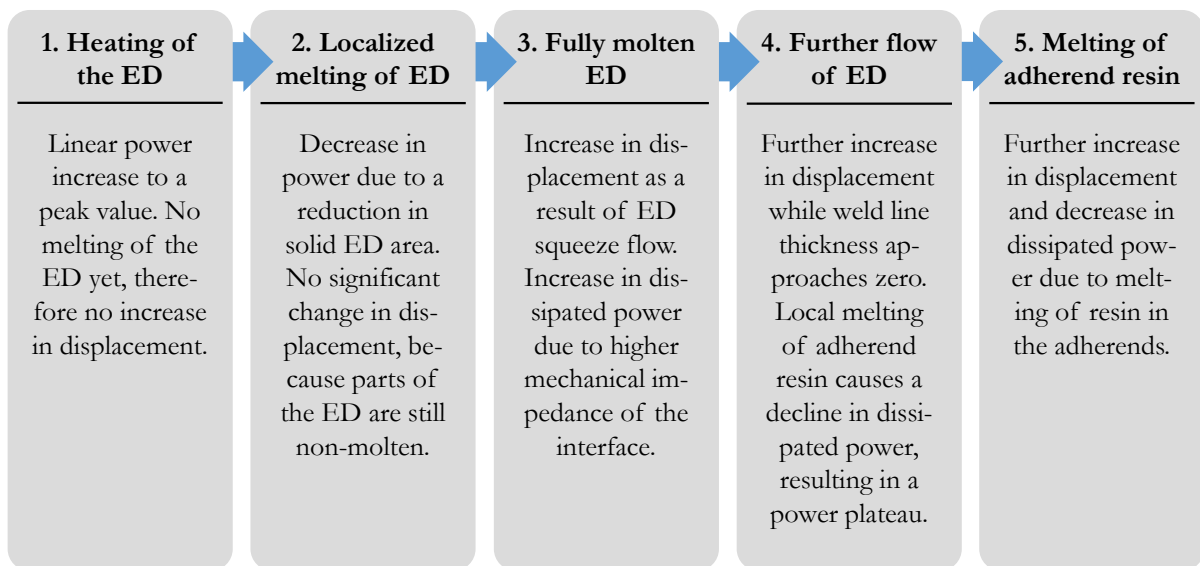


Figure 2.5: Stages in the welding process and their power and displacement characteristics [16].

The highest weld strength was consistently observed for processes ending in stage 4. During stage 3 the presence of the ED resulted in peak stresses, an effect that decreased continuously with squeeze flow towards stage 4. In stage 5 the molten adherend could no longer support the fiber bundles in the outermost plies, causing them to deform under the continued applied vibrations.

Whereas the time required to reach stage 4 varied, the sonotrode displacement and dissipated energy remained consistent. Contrary to displacement, energy is expected to vary with changes in boundary conditions, since not all supplied energy is used for the welding process. Instead, a portion is dissipated through the adherends, fixture and base [19].

The used welding force and amplitude did not have a significant effect on the strength that could be achieved. For each combination an optimum displacement/energy value could be identified, corresponding to a maximum strength that was consistently reached in stage 4. A combination of high force and high amplitude resulted in the fastest welding, with the smallest heat-affected zone in the adherends. This did, however, require more power compared to a process with a lower welding force and/or amplitude.

2.2.4. Control strategy for multi-spot welding

In recent years, Zhao et al. [25, 26] have investigated process control strategies for multi-spot welded joints. This research was based on aforementioned work by Villegas [16, 24] regarding the optimum process parameters for consistent weld strength. The main hypothesis was that the presence of a previous spot would affect the optimum energy, but not the optimum displacement, required for a second spot in a two-spot joint.

During preliminary investigation it was found that both displacement- and energy-controlled welding resulted in high-strength single spot welds. The optimum energy, however, varied substantially when different jigs were used, whereas optimum displacement remained unaffected. This confirmed that displacement-controlled welding is less sensitive to changes in boundary conditions.

Furthermore it was found that, for an energy-controlled two-spot weld, the welded areas of the first and second spot were around 10% and 30% smaller when compared to a single spot weld created at that same energy. For the displacement-controlled two-spot weld however, the welded area of the individual spots was found to approximately equal that of their single spot counterpart.

This research confirmed that, contrary to optimum energy, the optimum displacement for a two-spot column joint does not change compared to a single spot weld or between subsequent spots. This seems to suggest that the optimum displacement for a multi-spot welded joint can be determined once through a calibration weld and does not need to be re-evaluated for subsequent spots.

In subsequent research it was found that, following the established control strategy, multi-spot welded column joints could be created with a load-carrying capability close to that of mechanically fastened joints with multiple fasteners [27, 28]. Moreover, whereas damage in mechanically fastened joints was seen to be catastrophic and extend far beyond the hole, damage in the spot welded joints was found to remain restricted to the areas that had originally been welded.

2.3. Fatigue of single lap joints

The single lap joint is an anti-symmetric joint type in which two adherend surfaces are joined over a certain overlap length. Due to its relative ease of manufacturing and the amount of research already performed on multi-spot welding of this joint type by Zhao et al. [25–28], the single lap joint was the focus of this research.

When tested in a tensile shear configuration, the single lap joint experiences secondary bending as a result of eccentricity in the load path. This means that damage evolution in this type of joint can come as the result of more than one crack opening mode.

Typically, three different modes of crack opening can be distinguished. These modes are shown in Figure 2.6: (I) opening, also known as peel, (II) sliding or shear and (III) tearing. In a single lap joint tested under tensile shear, crack propagation will occur through a combination of mode I (as a result of secondary bending) and mode II (due to pure shear) crack opening [29].

In a continuous single lap joint, such as an adhesively bonded joint or welded seam, both shear and peel stresses typically attain maximum values at the ends of the overlap [31]. Following principles of superposition, it is easily understood that significant stress concentrations are present at the overlap ends. These stress concentrations are preferred locations for fatigue crack initiation. Alternatively, damage may already be present in the form of a manufacturing defect.

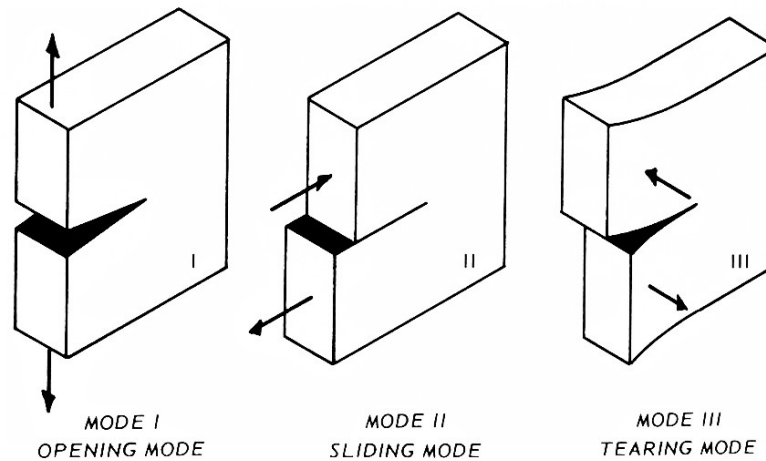


Figure 2.6: The three modes of crack opening [30].

An existing crack at the interface will propagate under continued cyclic loading, provided that the applied load is high enough. This crack growth will progressively reduce the effective bonded overlap length. The more this effective overlap length is reduced, the larger the amount of secondary bending and therefore the stress concentration at the crack tip becomes [29]. As a result, the crack growth rate increases progressively towards final failure.

Throughout this process of damage evolution, the crack growth rate is dictated by the medium that the crack is growing through. In practice this means that, once damage exists in a continuous single lap joint, there is limited resistance to its subsequent evolution. To explain how this behavior might be affected through joint design, some common design concepts for fatigue are discussed next.

2.3.1. Structural design concepts

Several structural design concepts for fatigue exist, all aimed at designing a structure or part in such a way that no catastrophic failure will result from cyclic loading during its intended service life. The three commonly used design concepts are safe life, fail safe and damage tolerant design.

Safe life design

Safe life fatigue design is based on the requirement that a structure or part should not fail within a predetermined amount of time. To successfully use this design strategy, it is necessary to know how the applied cyclic loading relates to the number of cycles until failure.

A common way to characterize this relation is through so-called Wöhler or stress-life curves. These curves relate the applied sinusoidal stress amplitude to the number of cycles until failure: a basic illustration of this concept is shown in Figure 2.7. There are many variables that affect the exact shape of this curve, such as material type, stress ratio or mean stress, frequency and temperature. However, so long as the intended operating conditions of the part under consideration are known and accounted for, the Wöhler curve can offer a reasonable estimate of its safe fatigue life.

Certain limitations exist when using Wöhler curves as an estimation for safe fatigue life, though. These limitations mostly relate to the way these curves are typically generated.

First of all, Wöhler curves are generally created through fatigue testing of coupons of the material under consideration. Fatigue behavior does, however, not only depend on the material that is used but also on the geometry of the part.

Secondly, the exact shape of the Wöhler curve will depend on the loading conditions during the fatigue test. Most often, the coupons will be subjected to a uni-axial sinusoidal load. Many parts will however encounter variable amplitude and/or multi-axial loading during their operational life.

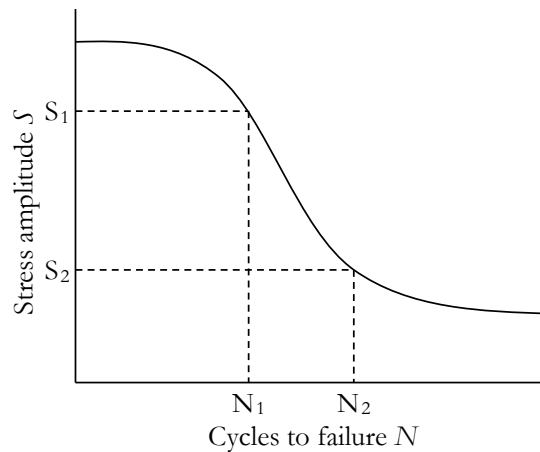


Figure 2.7: Example of a typical stress-life curve.

Methods exist to deal with both aforementioned limitations. For example, the applicability of the Wöhler curve can be improved through fatigue life testing of the actual part design, rather than simple coupon testing. In addition, variable amplitude load spectra can be accounted for as long as the load spectrum is known, through methods such as rainflow analysis [32]. There is, however, a phenomenon that this method fails to account for: the possibility that damage is already present in a part prior to its service life.

Fail safe design

A second design approach that is commonly used is fail safe design. Contrary to safe life design, the basis of fail safe design is the assumption that a part will fail. This part, however, should only be allowed to fail in a safe way: even when the part has failed, the overall structure should be able to maintain its required strength for a certain amount of time. In practice, this means that redundancies are introduced in the structure.

Compared to safe life design, fail safe offers the economic advantage that parts only need to be replaced once they have actually failed. In addition, failure of a single part in a fail safe design is not immediately critical. This is an improvement in safety over the safe life concept, where failure of a part will have catastrophic consequences. However, the fail safe approach still fails to account for the possibility that damage already exists within the part or structure.

Damage tolerant design

Damage tolerant design is based on the assumption that damage exists, or will arise, within the part or structure and is permitted to grow. This damage, however, is not allowed to grow to a critical size within a predetermined period of time. After this period, the damage can be detected and repaired during scheduled maintenance.

The foundation of damage tolerant design lies in fracture mechanics. This means that, contrary to safe life and fail safe design, damage tolerant design incorporates the physical processes related to damage evolution.

According to linear elastic fracture mechanics, crack propagation can be described through the strain energy release rate (SERR): the amount of energy released upon incremental growth of the fracture surface. Crack initiation or propagation will occur only if the SERR exceeds a certain critical energy release rate. This critical value is a characteristic of the medium through which the crack propagates, depending on its flexibility and fracture toughness for the different crack opening modes.

With this in mind, it can be understood that the damage tolerance of a single lap composite joint can potentially be improved by increasing the critical energy release rate at the weld interface, as this is where crack propagation is expected to occur.

The critical energy release rate increases with a higher fracture toughness and/or higher flexibility. In a multi-spot welded joint, the medium through which a crack propagates can be seen as the combination of the welded spots and the non-welded intermediate areas. These non-welded areas could be interpreted as having infinite flexibility: as such, it can easily be seen how a multi-spot welded joint would potentially offer increased damage tolerance.

On the other hand, these non-welded areas will also have zero fracture toughness. Ultimately, research is thus needed to determine if multi-spot welded joints could offer an improvement over continuous welded seams.

2.3.2. Arrangement effects in multi-spot welded steel joints

In 2011, Hassanifard [33] et al. investigated the effects of spot arrangement on fatigue behavior in a multi-spot resistance welded steel joint. Specifically, the effect of spot arrangement on fatigue life in a four-spot welded joint in three distinct layouts was investigated.

The single lap joint specimens used in this study were joined through resistance welding. Specimens were created with three different joint layouts: (A) four-row, single-column, (B) single-row, four-column and (C) two-row, two-column. The exact specimen geometries are shown in Figure 2.8: the indicated dimensions are all in mm.

It is suspected that an error is present in the figure: for the A-type specimen, it is assumed that the distance from the outermost spots to the ends of the overlap should be 10 mm instead of 5 mm.

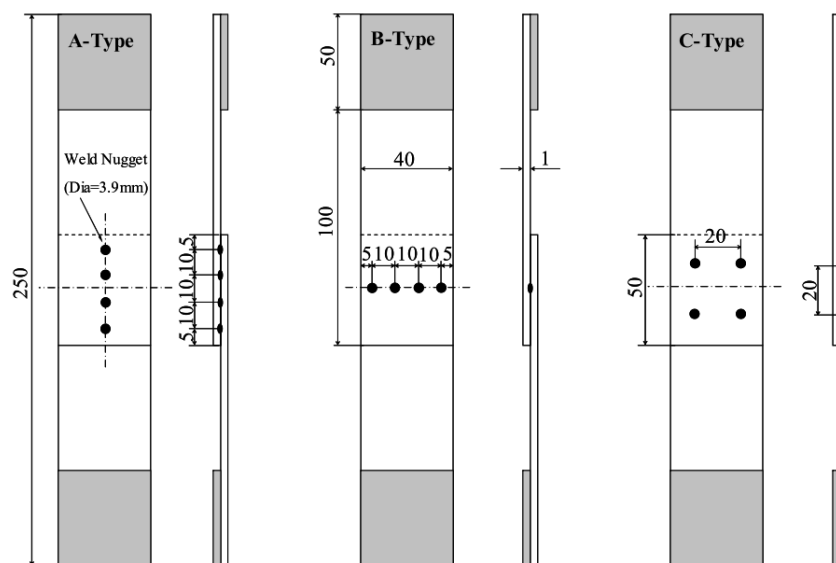


Figure 2.8: Geometries of the steel spot welded specimens tested for fatigue life [33].

The different geometries were tested for both static strength and fatigue life in a tensile shear configuration. The static tests were performed mainly to obtain a reference for the cyclic load that should be applied during fatigue testing.

Using these results the specimens were tested at various load levels, ultimately resulting in a stress-life curve for each of the three arrangement types. During these fatigue tests the applied load was kept strictly tensile, in order to prevent any potential buckling of the steel adherends. The resulting stress-life curves are shown in Figure 2.9.

From the stress-life curves it can be seen that the B-type specimens consistently show the highest fatigue life over practically the entire applied stress range. The lowest fatigue life, on the other hand, is consistently observed for specimens of the A-type. These results show that there is a clear dependency of joint fatigue behavior on spot arrangement.

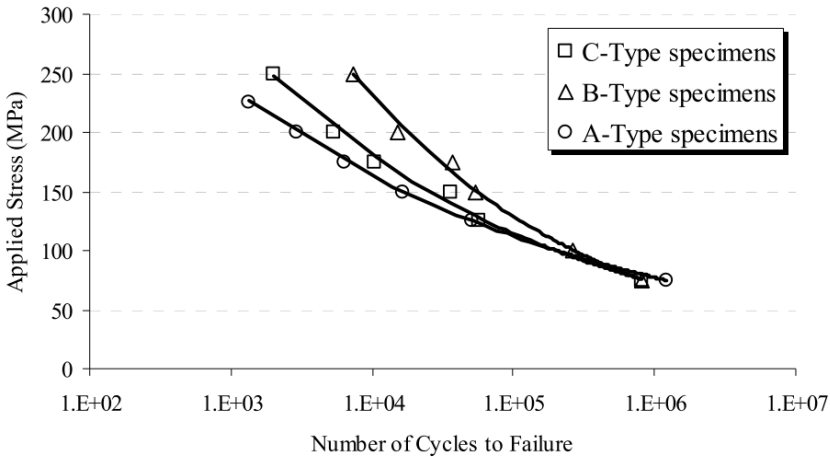


Figure 2.9: Stress-life curves for different four-spot arrangements in steel welded joints [33].

Apart from determining fatigue life, the failure modes of the specimen types at various load levels were assessed through visual inspection. Different failure modes were observed at different load levels. At high load levels, the specimens consistently failed through interfacial nugget fracture, whereas at low load levels all specimen types experienced sheet fracture of the adherends. At intermediate load levels, failure modes varied between the specimen types.

3

Research Definition

It has been identified that composites are being used increasingly in aviation and that TPCs, in particular, offer multiple advantages over their more commonly used thermoset counterparts. TSCs form an irreversible, cross-linked molecular structure after curing, whereas TPCs can be reshaped and processed through polymer softening and melting. This characteristic results in one of the biggest advantages of TPCs: the fact that they can be joined through welding. However, many unknowns still exist that currently prevent this process from being used industrially for joining of primary structural components.

In this chapter, the importance of this research is underlined by identifying a gap in existing knowledge. Section 3.1 describes the problem statement that served as foundation for this research. In Section 3.2 the scope of the research is defined in more detail and, in doing so, research questions are established. Section 3.3 then elaborates on the hypothesized answers to these questions.

3.1. Problem statement

Welding of TPCs is known to offer multiple advantages over conventional joining methods. Still, at this moment only two of many techniques are being used to join structural components on an industrial scale: induction and resistance welding. Both are continuous welding techniques.

In a continuous lap joint, damage evolution along the weld line under cyclic loading typically starts with crack initiation at the edge, followed by crack growth which then ultimately leads to final failure. Should damage happen to already be present in this type of joint, its remaining fatigue life will depend predominantly on its resistance against further crack growth.

Generally speaking, there are a number of ways in which the crack growth resistance of a medium can be changed. For example, a different material can be chosen or toughening particles can be embedded. Another option is to affect crack growth resistance through design.

A commonly used design solution for adhesively bonded joints is to include disbond arrest features in the form of rivets or bolts. A comprehensive review on such disbond arrest features is given by Hangx [34]. However, by introducing fasteners as disbond arrest features many of the initial advantages of welding as a joining method are negated. Drilling often damages the adherends and a pin load is introduced by the fastener, resulting in high stress concentrations. In addition, fasteners increase the structural weight of the joint.

An approach that might improve the crack growth resistance of a welded joint, while still benefiting from the advantages that this joining method offers, is to weld at discrete spots rather than over a continuous seam. As damage evolves through such a multi-spot welded joint, cracks will have to re-initiate in subsequent spots. Depending on the exact crack initiation and propagation behavior, this characteristic might delay overall damage evolution through the joint.

At this moment, ultrasonic welding is the spot welding technique with the highest level of maturity. This technique has already shown promising results in multiple regards, such as its low overall energy consumption and very short welding times. In this research it is used to study the evolution of fatigue damage in multi-spot welded joints. More specifically, the effects of spot arrangement on fatigue behavior are investigated.

The underlying research objective is to *explore the potential of multi-spot joint design in lap shear joints for damage evolution delay under cyclic loading.*

3.2. Scope and research questions

At this moment, very little is known about the fatigue behavior of multi-spot welded joints in TPCs. To the author's knowledge no research has yet been published in which this subject is investigated, which means that this research will serve as a first explorative step into this topic. To this end, a more narrow research scope must be defined.

To be able to place this research within a reference framework, existing research by Hassanifard et al. [33] is considered that investigates the effects of spot arrangement on fatigue behavior in four-spot welded steel joints. By using this work as a reference, fatigue behavior of multi-spot welded joints can be compared between TPCs and steel and it can be evaluated if certain established design rules and existing knowledge from steel might be transferable to TPCs. As a follow-up to this research, in future work the damage tolerance of these same joint layouts could be investigated by artificially introducing damage into the joints.

In this thesis, the methodology established by Hassanifard et al. is applied to welded TPC joints. Following this methodology, three different four-spot joint layouts are evaluated: a single-column (C), single-row (R) and square (S) layout. Schematic images of these layouts can be seen in Figure 3.1. For all three layouts, the amount of welded area is theoretically the same.

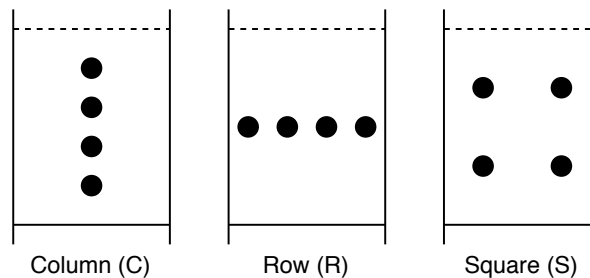


Figure 3.1: Schematic images of a four-spot column, row and square joint layout.

The main question that guides this thesis is as follows:

What are the effects of spot arrangement on fatigue behavior in a four-spot welded TPC joint?

This research question is split up into multiple sub-questions, each of which addresses a different aspect of fatigue behavior. These sub-questions are as follows:

- a. In what way is the fatigue life affected?
- b. What failure modes are observed?
- c. How does damage evolve through the joint?

This research is limited to single lap joints that are tested in a strictly tensile shear configuration. Cyclic loading is done in the form of constant-amplitude sinusoidal loading. The material combination that is considered is CF/PPS.

It is interesting to see to what extent results found for TPC and steel adherends compare to each other. Depending on how similar or different these results are, certain existing design rules and philosophies might be transferable from one material to the other. As a direct followup to the main research question, a second research question is thus formulated as follows:

To what extent can existing knowledge about the effects of spot arrangement on fatigue behavior in steel joints be transferred to four-spot welded joints in TPCs?

In answering this question, the following aspects are considered:

- a. How do the effects of spot arrangement on fatigue life compare between steel and TPCs?
- b. What similarities and differences are observed in failure modes across load levels?

In their research, Hassanifard et al. [33] did not address damage evolution under cyclic loading. Only failure modes and stress-life curves were presented as results. This means that no information is available that allows comparison between damage evolution in TPCs and steel for the considered four-spot joint layouts. Still, fatigue behavior of four-spot welded joints in TPCs and steel is compared within the scope of available information by considering fatigue life and failure modes.

3.3. Hypotheses

In this section, hypotheses relating to the main research question are presented. Fatigue behavior of a multi-spot welded joint was previously split into three main characteristics: fatigue life, failure modes and damage evolution. Each of these aspects is discussed subsequently. Expected results of the comparison between fatigue behavior in TPCs and steel are not discussed explicitly, as these flow directly from the hypotheses presented here.

3.3.1. Fatigue life

Generally speaking, the longest fatigue life at any load level is expected to be seen for spot arrangements in which the applied load can be distributed equally over the four spots.

Specifically, this means that a square joint layout is expected to reach the longest fatigue life. In this type of layout, each spot is theoretically subject to the exact same boundary conditions.

In a four-spot column joint, cracks are assumed to initiate in the outer spots at a relatively low number of cycles due to uneven distribution of the load across the spots. This uneven load distribution is typically seen in joints consisting of three or more rows of fasteners: in such a joint, the outer rows transfer a larger portion of the load than the inner ones [35].

In a four-spot row the load distribution over the spots will be more uniform than in the column joint, since the entirety of applied load is transferred from one adherend to the other by this single row of spots. However, due to their vicinity to a free edge the outer spots are still subject to different boundary conditions than the inner ones are.

Concluding, it is hypothesized that a column layout results in a much shorter fatigue life compared to a row or square layout. The latter two are assumed to lie close together, with square reaching a slightly higher fatigue life.

3.3.2. Failure modes

Due to the strictly tensile loading condition and the presence of reinforcing fibers in the adherends, failure is expected to always occur along the weld line in the form of through-the-spot fracture. At the weld line, a crack can propagate directly through the polymer matrix of the spot and outermost plies without needing to cross carbon reinforcement fiber bundles.

In line with this, first ply failure is assumed to be the observed failure mode regardless of load level and spot arrangement. Any damage observed on the fracture surfaces is expected to be restricted to the welded areas of the spots only. These assumptions are corroborated by findings of Zhao et al. [25–28], who consistently reported this failure mode and damaged area in quasi-static tests of various spot arrangements.

3.3.3. Damage evolution

Damage evolution is expected to depend heavily on the location(s) of crack initiation. This, in itself, will depend on quality and consistency of the spot welds. Two theoretical cases are considered in this hypothesis: an ideal case, where all spot welds are perfectly identical, and a non-ideal case, in which an imperfection leads to preferential crack growth through a single spot.

In the ideal case, cracks are assumed to propagate inwards from both overlap ends simultaneously. This case is depicted in Figure 3.2 for a column, row and square joint layout. Note that this image represents a case in which all spot welds still have a load-carrying capability. The red arrows indicate locations where cyclic crack growth is assumed to occur.

Looking at this image, it can be understood that cyclic loading will gradually decrease the amount of load-carrying welded area until the shear strength of the joint is ultimately exceeded. At this point, the gradual crack growth is followed by sudden joint failure. For a column joint this will occur at a lower number of cycles than for a row or square joint, since only two of the four spot welds in a column resist cyclic crack growth simultaneously.

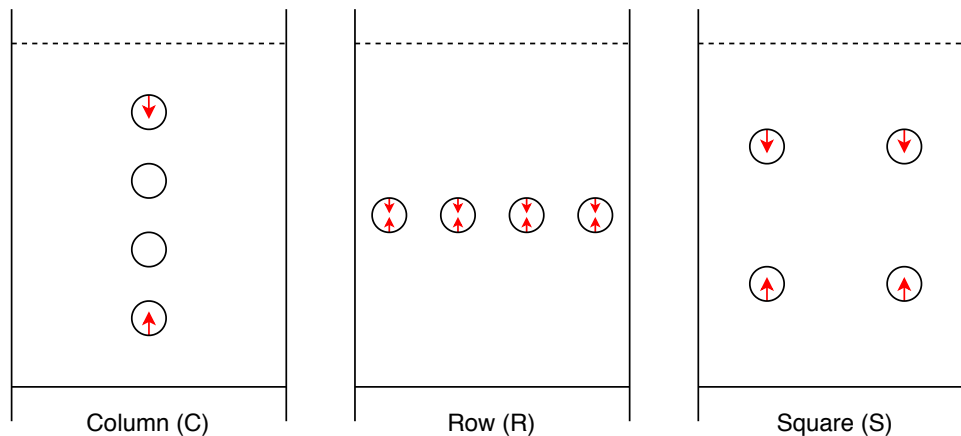


Figure 3.2: Predicted path of damage evolution for ideal spot welds.

In a non-ideal case, damage evolves through a single spot rather than through multiple spots simultaneously. As a result, this spot experiences larger cyclic crack growth.

Examples of this damage evolution through a single spot are shown in Figure 3.3. Note that, for the column and row layouts, preferential damage evolution will only occur in the outermost spots as their presence prohibits crack growth in the inner spots. For a square joint layout, preferential damage evolution due to imperfections may occur in any of the four spots.

If a joint experiences preferential damage evolution through a single spot, this spot will fail at a low number of cycles compared to the fatigue life of an ideal joint. However, after failure of this first spot three intact spots still remain to carry the applied load. Although the total amount of load-carrying area in the joint has decreased, it is assumed that the remaining spots continue to carry load for a certain amount of cycles after failure of the first spot.

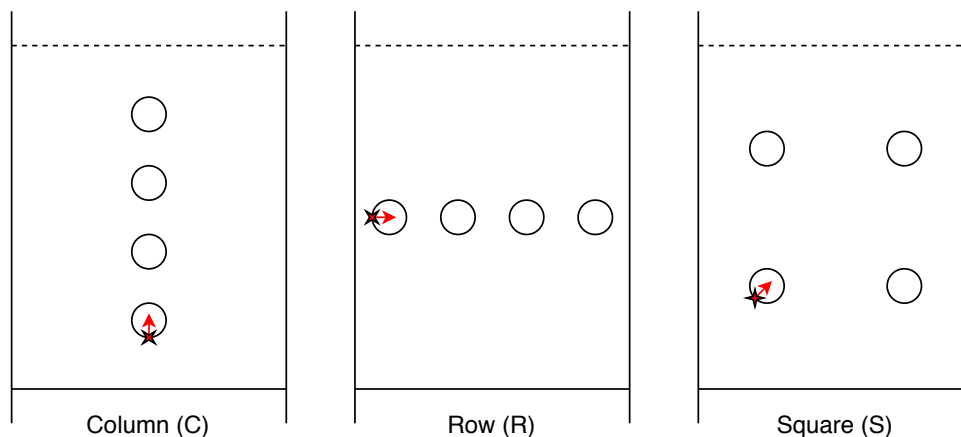


Figure 3.3: Predicted damage evolution due to spot weld imperfection.

In conclusion, if crack growth occurs in a single spot as a result of imperfections, the fatigue life of this joint is expected to be much shorter than in an ideal case. However, failure of this first spot will act as an indicator for upcoming joint failure, since the remaining three spots are assumed to continue carrying load for some time before final failure. Conversely, in an ideal joint it is expected that no indicator of imminent failure can be observed.

4

Methodology

In Chapter 3, the main objective of this research was defined and research questions were established. The main question that was identified was the following:

What are the effects of spot arrangement on fatigue behavior in a four-spot welded TPC joint?

To answer this question, existing methodology for four-spot welded steel joints with different joint layouts [33] was transferred to ultrasonically welded joints on TPC adherends. Four-spot welded joints were created in three different joint layouts to be tested in fatigue tests. Fatigue life, failure modes and damage evolution were compared between the three joint layouts, after which these interrelations themselves were evaluated against the ones found for different layouts in steel joints.

The complete methodology is addressed in detail in this chapter. First, a general design of experiments is proposed in Section 4.1. Specimen geometries are defined, the number and types of tests are detailed and a common nomenclature is established. Specimen production is then addressed in Section 4.2. This section details all steps in laminate manufacturing, specimen preparation and assembly. Section 4.3 elaborates on the test methods and equipment used for quasi-static and fatigue testing. Finally, Section 4.4 discusses the employed data acquisition and processing methods.

4.1. Geometries, test matrix and nomenclature

The main goal of this series of tests was to determine how the arrangement of spot welds in a four-spot welded TPC joint affects fatigue behavior and how this relates qualitatively to results found for similar four-spot welded steel joints, as investigated by Hassanifard et al. [33].

To this end it was not necessary to replicate the exact steel sample dimensions: the specimens could be up- or down-scaled. An important consideration in determining specimen size was to choose sufficiently large inter-spot distances, as failing to do so would cause interference during welding between the flow front of a molten ED and a still-intact adjacent ED.

When using circular flat EDs with a 4 mm diameter and thickness of 0.24 mm, Zhao et al. [28] found that this interference effect occurred at an inter-spot distance of 10 mm and that it decreased the welded areas of the involved spot welds, while also increasing variability in the measured welded areas over multiple specimens. At distances of 20 mm and higher, the effect was no longer observed.

To keep consistency of the welded area between different joint layouts as high as possible while still minimizing required material usage, a minimum inter-spot distance of 20 mm was chosen. As a result, minimum required overlap dimensions were defined as shown in Figure 4.1a. An adherend length of 170 mm was chosen to allow efficient nesting of samples on the base TPC laminates, while still leaving sufficient free length available for specimen clamping during tests.

The three different four-spot joint layouts are shown in Figure 4.1b. The relations between all dimensions were kept identical to those of the geometries used by Hassanifard et al. [33].

An overview of performed tests is given in Table 4.1. A total of 14 specimens were tested: each of the three joint layouts was tested quasi-statically for ultimate tensile failure load, after which multiple fatigue tests were performed at a percentage of this load. The exact amount of fatigue tests required to obtain sufficient information varied between the different layouts.

Two square specimens and one column specimen were tested incorrectly and were therefore not a part of fatigue analysis. Still, they are mentioned here since they were considered in the weld quality analysis described in Section 6.1.

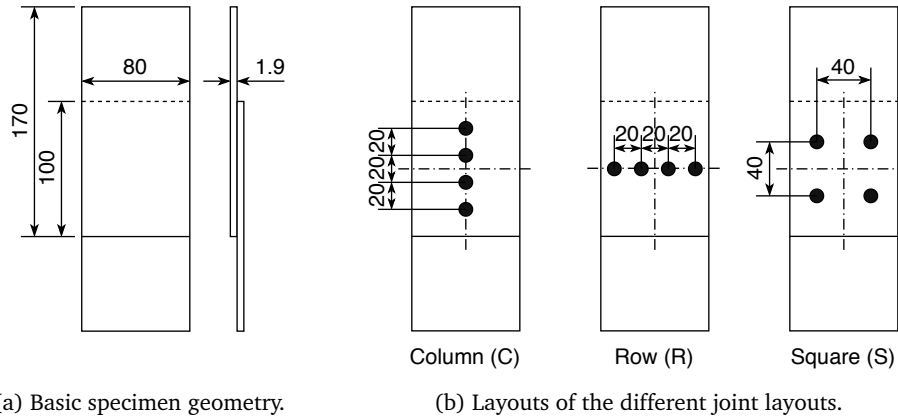


Figure 4.1: Geometries of the spot welded fatigue life specimens (dimensions in mm).

A single specimen with a square layout was used for tuning of the fatigue machine. Since tuning sometimes damages the specimen that is being used, this specimen was not considered for fatigue analysis. However, like the incorrectly tested specimens this specimen was assessed for weld quality.

Table 4.1: Performed number and type of tests per joint layout.

Joint layout	Test type	No. of tests	Specimen ID
Column	Static failure	1	C_SF
	Fatigue life	4 ¹	C_FL n
Row	Static failure	1	R_SF
	Fatigue life	2	R_FL n
Square	Static failure	1	S_SF
	Fatigue life	4 ²	S_FL n
	Fatigue tuning	1	S_TU

¹ Includes one failed test, which is referenced as C_FL x 1.

² Includes two failed tests, which are referenced as S_FL xn .

The static failure load was determined primarily as an input value for fatigue testing. Because of this, quasi-static testing was done only once for each joint layout. It should therefore be noted that the relevance of the reported failure load as a standalone value is limited.

Specimens were named according to the conventions presented in Table 4.1. When referring to individual spot welds on a specimen, the sequence in which the spots were originally welded was used. These welding sequences are detailed for the different joint layouts in Figure 4.2. As an example, a spot with the number 1 is referred to with the suffix “_s1”.

4.2. Specimen production

With the design of experiments laid out, specimen manufacturing is addressed next. All manufacturing and assembly steps that constitute this process are detailed. In addition, material characteristics are provided and the selected process control parameters for ultrasonic welding are discussed.

4.2.1. Manufacturing of adherends

For this research, three TPC laminates were manufactured in the Delft Aerospace Structures and Materials Laboratory. In accordance with earlier research performed by Zhao et al. regarding ultrasonic spot welding of TPCs [25–28], the chosen material combination was CF/PPS.

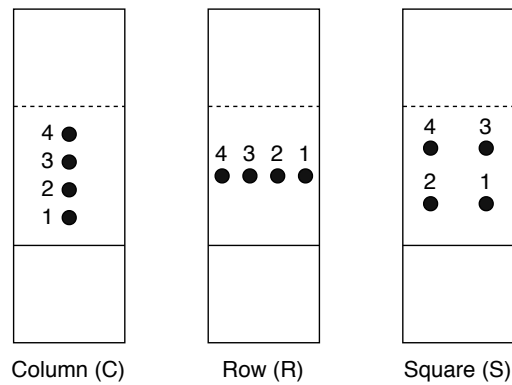


Figure 4.2: Spot weld numbering conventions.

The laminates were manufactured from Toray Cetex[®] TC1100 powder-coated semipreg, which features a T300JB carbon 5-harness satin weave fabric. In a 5-harness satin weave each fiber bundle crosses four subsequent fiber bundles in the transverse direction, as illustrated in Figure 4.3. Six square fabric plies with dimensions of 590 mm × 590 mm were used in a $(0/90)_3$ layup.

The plates were hot press consolidated at a temperature of 320 °C and pressure of 1 MPa for 20 minutes: the full temperature-pressure control cycle is shown in Figure 4.4. To ensure uniform surface heat distribution throughout the consolidation process, each laminate was sandwiched between two graphite plates. After consolidation, the final thickness of the three laminates was 1.80, 1.84 and 1.90 mm. In each of the three laminates, variations in thickness were found to remain within a range of ± 0.01 mm.

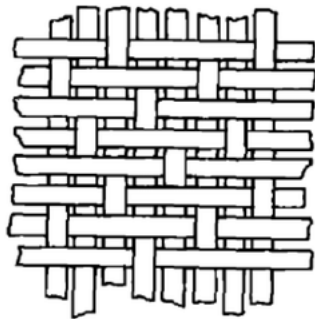


Figure 4.3: Structure of a 5-harness satin weave [36].

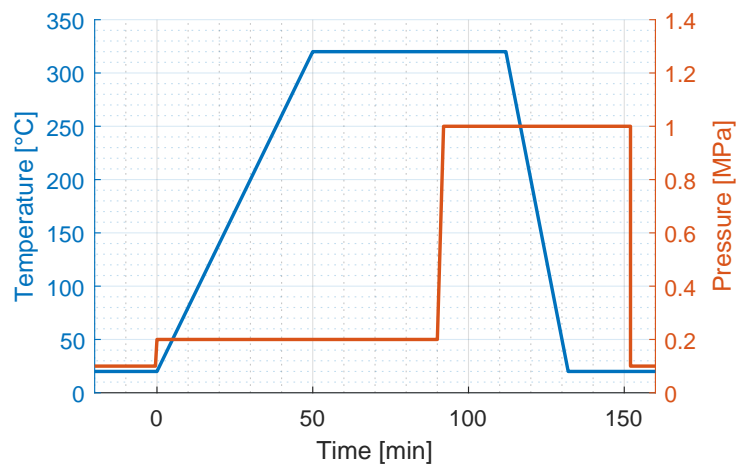


Figure 4.4: Press control cycle for consolidation of CF/PPS laminates.

The consolidated laminates were cut into rectangular samples using a diamond saw cutting table: specific specimen dimensions have been outlined previously in Section 4.1. Note that, in all cases, the samples were cut from the laminates in such a way that the main apparent fiber orientation was parallel to the direction of the applied load during testing.

4.2.2. Ultrasonic spot welding

Spot welding was done using the Rinco D3000 ultrasonic welding machine, which operates at a vibration frequency of 20 kHz. Conform the methodology established by Zhao et al. [25–28] a cylindrical titanium sonotrode with a diameter of 10 mm was used.

To prevent movement of the adherends during welding, they were kept in place on the aluminum base plate by two bar clamps. These clamps were attached to the base plate through bolted connections, each of which was tightened to a torque of 18 Nm. A supporting piece of material with a thickness of 1.9 mm was placed underneath the free edge of the top adherend to prevent angle misalignment between the two adherends. A schematic of the setup is shown in Figure 4.5.

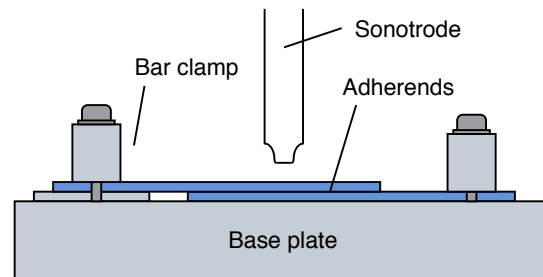


Figure 4.5: Schematic of the used welding setup.

To promote heat generation at the interface between the adherends during welding, circular PPS EDs with a 4 mm diameter were used. These EDs were punched from a flat sheet of PPS with a thickness of 0.24 mm, which was in turn created through hot press consolidation of three layers of 0.08 mm Fortron[®] amorphous PPS film.

Prior to welding, the ED spots were fixed onto the adherends using a Rinco handheld ultrasonic welder. In combination with the aforementioned 10 mm circular sonotrode, these EDs resulted in circular spot welds with an approximate diameter of 10 mm.

In previous work Zhao et al. [25, 26] worked on defining a process control strategy for multi-spot welded joints. Their approach was based on earlier work by Villegas [16, 24] regarding optimum process parameters for consistent weld quality. It was discovered that displacement-controlled welding shows a low sensitivity to changes in boundary conditions [25] and that the optimum displacement does not change for subsequent welds in a multi-spot welded joint [26].

Based on these findings Zhao et al. opted for displacement-controlled welding as their process control strategy. It was found that, contrary to full overlap joints, spot welds required a linearly increasing force during the vibration phase to ensure a continued squeeze flow of the ED [26]. Spot welds were successfully created at a force rate of 1000 N/s. In combination with an initial welding force of 1500 N and a peak-to-peak amplitude of 60.8 μm an optimum displacement of 0.23 mm was determined. Consolidation was done under a force of 1500 N for 4000 ms.

The author verified experimentally, through creation of single and two-spot column welds, that using the aforementioned combination of welding parameters resulted in high-quality welds. Therefore, the same set of welding parameters (as summarized in Table 4.2) was used for this research.

4.3. Experimental test methods

With regard to experimental testing two main series of tests were performed: quasi-static tensile shear tests to determine the ultimate failure load, and fatigue tests at a set percentage of this static failure load. For both of these test types, procedures are detailed in this section.

4.3.1. Static failure load determination

Tensile shear testing was done on a Zwick/Roell 250 kN universal testing machine, with the main goal of determining the ultimate failure loads of all three joint layouts. In these tests the specimens were subjected to a continuously increasing tensile load until failure of the joints occurred.

The specimens were clamped in the machine using hydraulic grips. The lower grip was placed at a horizontal offset of 1.9 mm with respect to the upper grip, to account for the anti-symmetry of

Table 4.2: Control parameter values for sequential ultrasonic welding as used in this research.

Phase	Parameter	Value	Unit
Vibration phase	Initial force	1500	N
	Force increase	1000	N/s
	Vibration amplitude ¹	60.8	μm
	Vibration frequency ²	20	kHz
	Displacement	0.23	mm
Consolidation phase	Consolidation force	1500	N
	Consolidation time	4000	ms

¹ Peak-to-peak.

² Note that the vibration frequency is typically fixed, as it depends on the type of ultrasonic welding machine that is used [16].

the single lap specimens. This way, the weld interface was aligned parallel to the loading direction. Rectangular grip inserts were used to ensure proper and uniform clamping over the entire specimen width. After each test it was verified that no slipping of the specimens had occurred in the grips.

The initial grip-to-grip separation of the machine was set to 170 mm. No preload was imposed at the beginning of the test: after clamping, the grip-to-grip separation was updated accordingly to satisfy this condition.

The tensile load during testing was increased in a displacement-controlled manner, at a constant rate of 1 mm/min. This displacement rate followed from preliminary test results and available knowledge in the lab on tensile shear testing of CF/PPS single lap joints. The displacement was applied through vertical cross-head motion.

Although the primary goal of these tests was to determine the ultimate failure load of each joint layout, load- and displacement data still provided valuable insight into joint performance and damage evolution leading up to failure. These data were monitored in the form of applied load (P), which was directly derived from the load cell, and cross-head displacement (d). With these data, combined with the total welded area (WA), the shear strength τ_{ult} and joint stiffness JS could be calculated.

$$\tau_{ult} = \frac{P_{ult}}{WA} \quad (4.1)$$

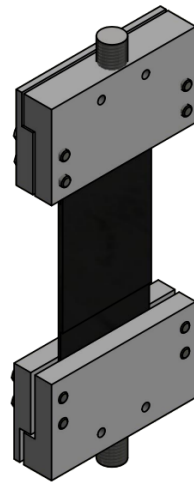
$$JS = \frac{\Delta P}{\Delta d}, \quad \text{during initial linear-elastic stage only} \quad (4.2)$$

4.3.2. Fatigue testing

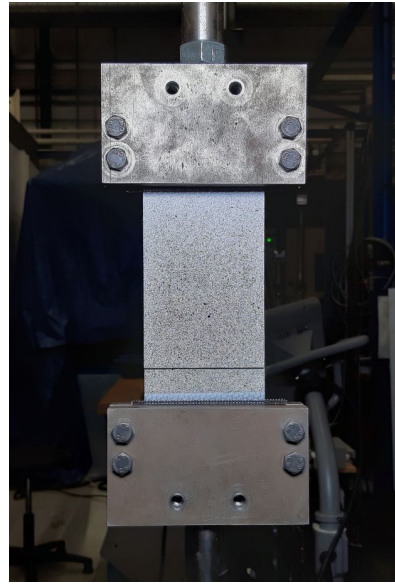
Fatigue tests were executed using the MTS 810 Material Test System, which has a load range up to 15 kN. All tests were performed under load-controlled sinusoidal constant-amplitude loading, with a frequency of 5 Hz, as is commonly used in composite fatigue testing [37–39], and an R-ratio of 0.1 conform the methodology of Hassanifard et al. [33].

The specimens were clamped using bolt-tightened grips, as displayed in Figure 4.6. These specific grips were chosen because they eliminated the need to drill holes in the adherends. Another good option would have been to use hydraulic wedge grips, but no sufficiently wide wedges were available that could clamp over the entire specimen width.

To account for the naturally present eccentricity of the single lap specimens, a 2 mm thick steel plate was clamped in the upper grip at the faying surface (looking at Figure 4.6b, this means the steel



(a) Schematic image.



(b) Photo of the actual setup.

Figure 4.6: Bolt-tightened clamps as used for fatigue testing.

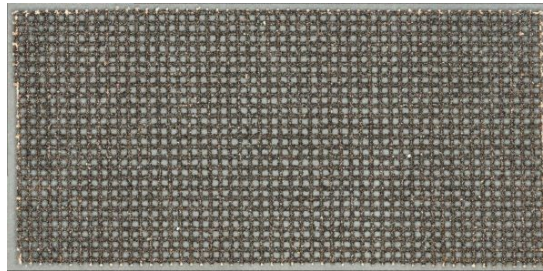


Figure 4.7: Sandpaper mesh used for grip tabs.

plate was placed behind the specimen). Grip tabs in the form of grit 120 sandpaper mesh, shown in Figure 4.7, were used to keep the specimen from slipping during the tests. Since these grip tabs resulted in friction with both the specimen itself and the grips, adhering them to the specimens was not necessary. Instead, they were simply clamped in the grips together with the specimen.

Specimens were clamped in the upper grip first, which was completely fixed in position. The bottom grip was allowed to rotate around its longitudinal axis, so that specimens made from slightly warped material could still be clamped without imposing an out-of-plane preload. The bolts were tightened to a torque of 20 Nm in increments of 2 Nm, following a cross-shaped tightening sequence.

The design of these grips resulted in a horizontal offset of 6.4 mm between the specimen weld interface and the piston center-line, meaning that some amount of additional secondary bending was introduced. This was, however, not considered a problem for this research since all specimens were tested under this same condition.

Fatigue life testing was done at 70% of the measured static failure load, with the goal of ending up in the low-cycle fatigue regime. Tests performed at these relatively high load levels were expected to allow the most informed comparison with steel joint fatigue behavior.

Hassanifard et al. [33] found that steel spot welds in the low-cycle regime consistently failed from fracture through the spots. This same failure mode was, however, not observed in the high-cycle regime: here, adherend sheet fracture transverse to the loading direction was found to be the dominant failure mode. Although it is assumed that spot welded joints in TPCs fail from spot fracture regardless of applied load level, it was considered most interesting to compare the results for TPCs and steel in the low-cycle regime, were both materials would show a comparable failure mode.

4.4. Data acquisition and processing

This section discusses the methods of data acquisition and processing that were used to acquire relevant information from the fatigue tests. The welded areas of individual spots were evaluated through microscopy and image analysis of the fracture surfaces after testing (Section 4.4.1). Data acquisition during the tests was done through monitoring of the cyclic peak-valley load and displacement values (Section 4.4.2) and by taking photos at regular intervals for digital image correlation (Section 4.4.3). For all three acquisition methods, processing steps are detailed in the respective sections.

4.4.1. Microscopy and image processing

After destructive testing, fracture surfaces of the spots were analyzed through optical microscopy and image processing. The primary goal of this analysis step was to assess weld quality by measurement of the total welded area. In addition, adherend warpage was quantified in an attempt to determine if warpage affects the amount of welded area and, by extension, weld quality of the spots.

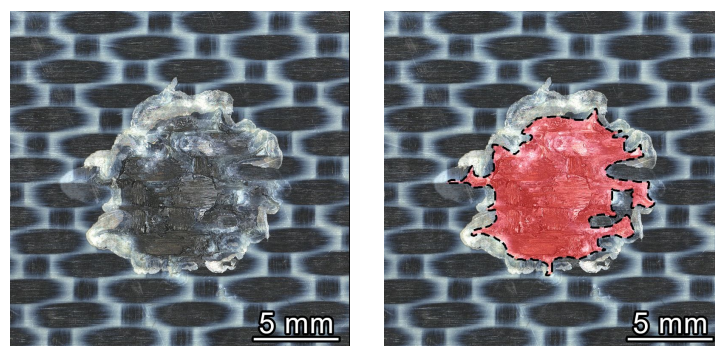
The Keyence VR-5000 Wide Area 3D measuring system was used to obtain low-magnification ($12\times$) images of the joint surface and individual spot welds. This microscope was chosen primarily for its stitching functionality, in which multiple microscopy images are combined in order to create a single image of a larger surface area. This way, it was possible to obtain images of the entire overlap area as well as of the individual spot welds.

In obtaining and processing the surface images, a couple of criteria were followed consistently:

- Microscopy images of the individual spot welds were always taken on the bottom adherend (referring to its position during welding).
- The direction of applied load is always the horizontal direction in the images, unless indicated otherwise in the text.
- An image of the full joint always spans the dimensions of the overlap: $100\text{ mm} \times 80\text{ mm}$. Since these images have a size of $2120 \times 1696\text{ px}$, this translates to a pixel ratio of 21.2 px/mm .
- An image of a single spot weld always spans an area of exactly $20 \times 20\text{ mm}$. Since these images have a size of $1696 \times 1696\text{ px}$, this translates to a pixel ratio of 84.8 px/mm .

The welded areas of the spot welds were measured using the NIH image analysis software ImageJ, version 1.52d [40]. The plugin ‘Dotted Line’ was used to trace the outline of the welded area.

An example fracture surface is shown in Figure 4.8. Note that the flow front of the ED was not considered in tracing the total welded area. No actual welding to the adherends was observed here, meaning that the contribution of this area to the joint strength was assumed to be negligible. This is consistent with the way that welded area was measured by Zhao et al. [28].



(a) Original image as obtained from the Keyence VR-5000 microscope. (b) Selection of welded area using ImageJ image analysis software.

Figure 4.8: Welded area determination using the Keyence VR-5000 microscope and NIH image analysis software ImageJ [40].

Figure 4.9 illustrates the basic principle of warpage in a rectangular plate. The dotted outline represents a perfectly straight plate. The continuous outline is an example of a warped plate: the corners *A* and *D* have displaced upwards, whereas *B* and *C* have moved downwards. In general, a plate is considered warped if its four corners no longer lie on a single two-dimensional plane.

The situation sketched in Figure 4.9 is visualized in the example image shown in Figure 4.10: here, it can clearly be seen that corners *A* and *D* of this specimen are elevated compared to *B* and *C*. By measuring height values at the four corners, a warp angle could be defined.

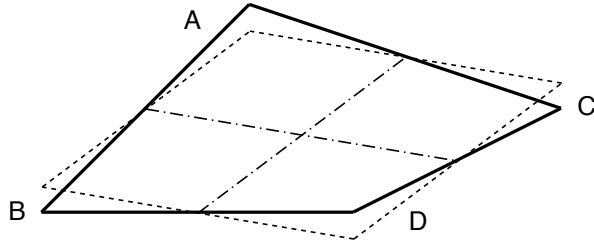


Figure 4.9: Schematic representation of warpage in a rectangular plate.

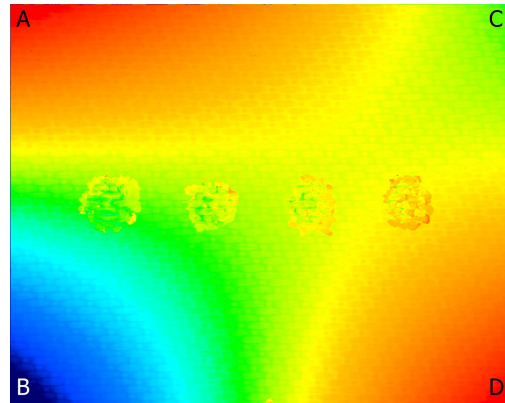


Figure 4.10: Height image obtained from the Keyence VR-5000, indicating warpage.

The warp angle was evaluated by considering the angle of misalignment ϕ between line segments *AB* and *CD*. This concept is illustrated in Figure 4.11, where *w* is the length of the line segments *AB* and *CD*.

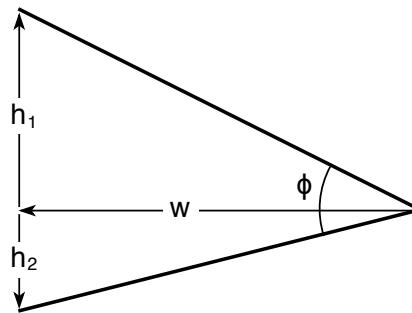


Figure 4.11: Angle of misalignment ϕ between two line segments.

According to this figure and assuming small angles, ϕ can be calculated as follows:

$$\phi = \left| \tan^{-1} \left(\frac{h_2}{w} \right) - \tan^{-1} \left(\frac{h_1}{w} \right) \right| \approx \frac{|h_2 - h_1|}{w}$$

Note that, in order for this equation to be valid, points *A* and *C* need to coincide. This was accounted for through a vertical offset for both points *B* and *D*:

$$\phi = \frac{|(z_B - z_A) - (z_D - z_C)|}{w}$$

Finally, the angle of misalignment was normalized by dividing it by the overlap length, which is the distance between segments AB and CD . This way, the warp angle was defined as seen in Equation (4.3). Note that this last step of normalization was taken purely to present more intuitive values: this does not mean that the angle increases linearly with overlap length.

$$\theta = \frac{\phi}{L} = \frac{|(z_B - z_A) - (z_D - z_C)|}{wL} \quad (4.3)$$

4.4.2. Cyclic load and displacement data

Load and displacement data of the fatigue tests were obtained through cyclic peak-valley acquisition derived from the load cell. The main goal of evaluating these data was to localize the onset of final failure and determine the approximate remaining lifetime. In order to present these data in an informative way, multiple data cleaning steps were taken. These steps are all illustrated in Figure 4.12 and are described in more detail below.

The following data cleaning steps can be seen in Figure 4.12:

- (a) This figure shows the raw displacement data plotted against the number of cycles.
- (b) All valley data points were removed. Since minimum displacement and load show the same trends as their maximum counterparts, they could be excluded without losing relevant information. This significantly reduced computation times. Removal of the valley data points was done by defining a «threshold» value that separated the peak and valley parts of the graph. Everything below this value was excluded from the data set.
- (c) Vertical lines corresponding to the DIC interval were omitted. At regular intervals, the test was paused so that DIC photos could be taken. After this dwell it took a certain amount of cycles before the machine response could match the control load again: this manifested itself as regular vertical ‘dips’ in the load and displacement data. Occurrences were localized by defining a «drop» value. Whenever the difference between two subsequent displacement values was greater than «drop», the next «response_cycles» points were excluded. The value of «response_cycles» was defined by inspecting the data sets and was found to be 25 cycles for the majority of the specimens.
- (d) An offset was defined in such a way that the reported peak displacement at the start of testing equaled zero. In the same way as was done for the machine response after a DIC dwell, the first «response_cycles» points were omitted from the data set. The first subsequent displacement value was used as «offset», after which all displacement values were updated accordingly.
- (e) In the final graph, the vertical axis was re-scaled and the peak control load included. The load data were processed in the exact same way as the displacement data, the only difference being that the former were not offset-corrected.

4.4.3. Digital image correlation

Digital image correlation (DIC) is a method in which the deformation of an object over time is measured by tracking specific points on its surface. To use this method successfully, a random black-and-white speckle pattern was applied to the surface of interest. This was done by misting black spray paint over a white paint base coat. By measuring the displacements of these speckles on photos in a loaded state with respect to a reference image in unloaded state, full strain and displacement fields can be derived. When only one camera is used 2D fields can be obtained, whereas two cameras at different angles are needed for 3D data that include out-of-plane displacement.

Two cameras were used to obtain 3D displacement data. Photos were taken every 1000 cycles. Unfortunately, a mistake in the control program resulted in DIC photos being taken at the minimum load instead of the maximum load, meaning that the specimens were in a (close to) unloaded state.

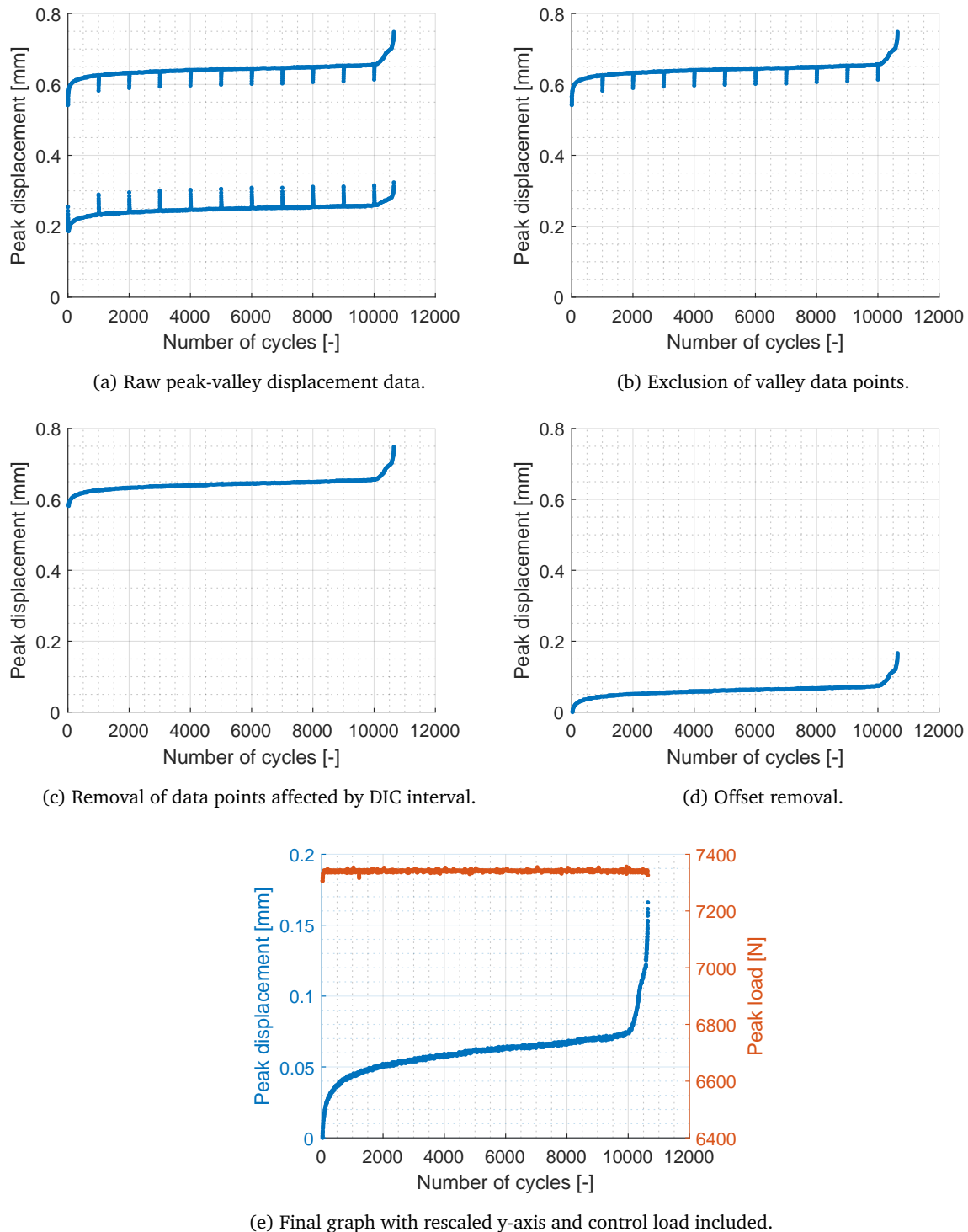


Figure 4.12: Steps in cleaning up the raw peak-valley load and displacement data, obtained from the MTS 15 kN fatigue machine.

As a result, proper strain fields could not be derived from these images. However, displacements over time with respect to the undamaged specimen could still be tracked as a result of material warpage: as damage evolved through the joint, the adherends became less restricted by the presence of the spot welds and showed out-of-plane deformation towards their original warped shape.

Data processing was done in the form of out-of-plane displacement graphs. An example line graph for a square joint layout is shown in Figure 4.13. Spot weld locations are indicated by dashed lines.

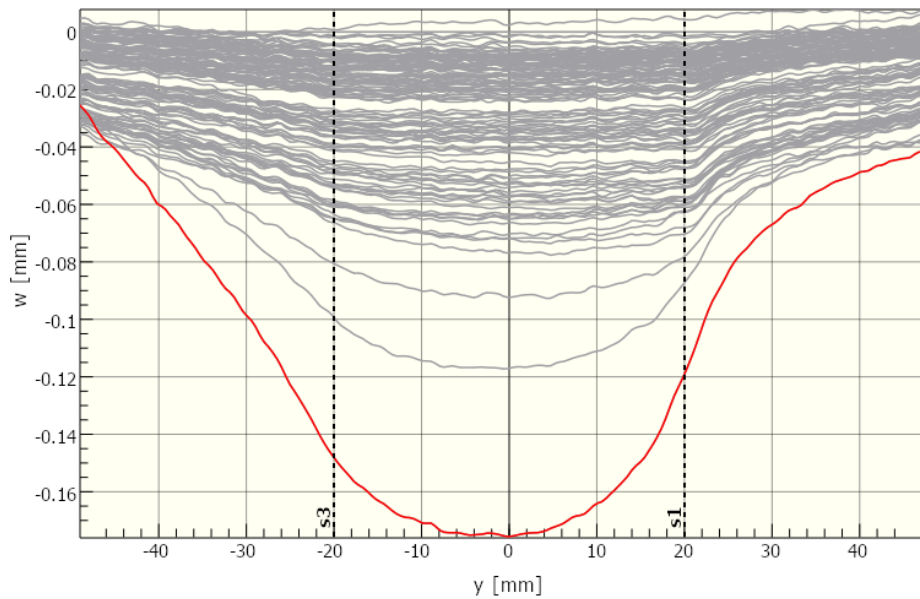


Figure 4.13: Example line graph showing out-of-plane displacement.

In these line graphs, out-of-plane displacement w with respect to the first reference image is displayed for every DIC measurement along a transverse (varying x) or longitudinal (varying y) line that passes through one or multiple spots. By definition, the last measurement before final failure is always highlighted in red.

Alternatively, evolution of out-of-place displacement at the locations of the four spots was evaluated over the entire lifetime of the joint as displayed in Figure 4.14.

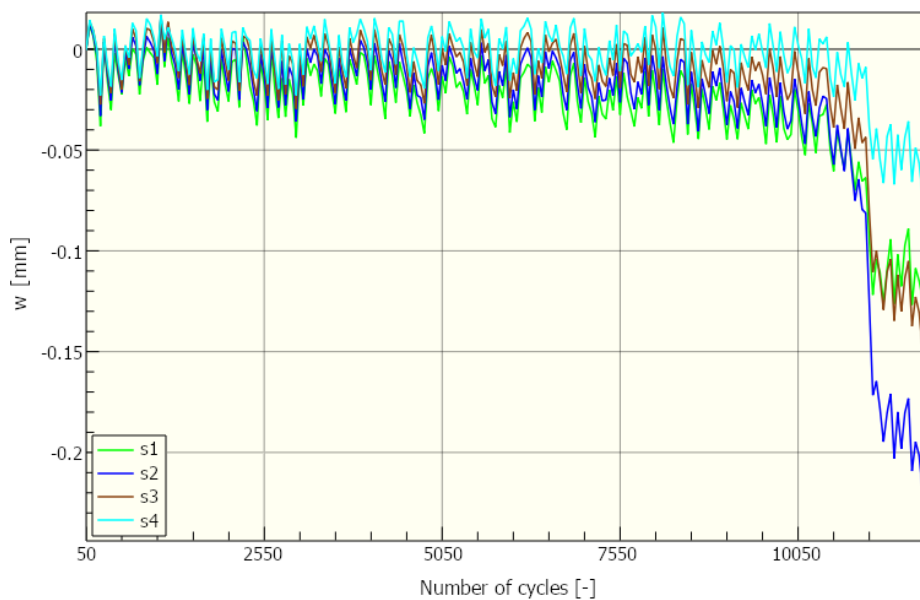


Figure 4.14: Example graph showing out-of-plane displacement at spot locations over time.

All displacement data were derived with Vic3D software, using a subset (area that is considered for a single data point) dimension of 27 px and a step size (distance to next data point) of 7 px.

5

Results

Table 5.1 shows an overview of the gathered test results per specimen, split by joint layout. A check mark (✓) indicates that results of this type were acquired for this specimen and were used in subsequent analysis in Chapter 6. A select number of results have been marked with a red cross mark (x): these results were acquired correctly, but were subsequently deemed unreliable. Certain results were not acquired or were excluded from analysis for varying reasons:

- Both C_FLx1 and S_FLx1 were tested incorrectly in such a way that the specimens failed before cyclic loading was applied. As a result, no fatigue life could be determined and data that would normally be acquired during cyclic loading (load and displacement data and DIC photos) do not exist for these specimens.
- S_FLx2 was tested directly after the incorrectly tested S_FLx1. Uncertainty exists on the machine settings and calibration at that time. Since it was not possible to eliminate this uncertainty or determine how it may have affected test results, all fatigue data relating to specimen S_FLx2 were excluded from further analysis.
- For C_FL1, no DIC data are available. This specimen failed before the specified number of cycles for DIC data acquisition (1,000 cycles) was reached. For subsequent specimens of the column type, the DIC interval was lowered from 1,000 to 50 cycles as a result.
- S_TU was used solely to tune the fatigue machine response for the specimens used in this research. This specimen was not a part of any further quasi-static or fatigue analysis.

Experimental test results are presented in this chapter. In Section 5.1, welded area and warp angle as derived from microscopy images are presented. Results of quasi-static testing are given in Section 5.2: from the acquired load-displacement data, shear strength and joint stiffness have been calculated. Finally the fatigue lives, cyclic load and displacement data and DIC results from the fatigue tests are presented in Section 5.3.

Table 5.1: Overview of available results for all tested specimens. A check mark (✓) indicates that results of this type are available for this specimen and were used in analysis. A red cross mark (x) means these results are available, but were considered unreliable and were therefore excluded from analysis.

Result type	Column					Row			Square					
	C_SF	C_FL1	C_FL2	C_FL3	C_FLx1	R_SF	R_FL1	R_FL2	S_SF	S_FL1	S_FL2	S_FLx1	S_FLx2	S_TU
Surface microscopy	✓	✓	✓	✓	✓	✓	✓	✓	✓	✓	✓	✓	✓	✓
Quasi-static test results	✓					✓			✓					
Fatigue life		✓	✓	✓			✓	✓		✓	✓		x	
Cyclic load and displacement data		✓	✓	✓			✓	✓		✓	✓		x	
Digital image correlation			✓	✓			✓	✓		✓	✓		x	

5.1. Surface microscopy

After destructive testing, surface microscopy images were obtained of the individual spot welds and of the full overlap areas. From these images, the welded areas of the spots and warp angles of the adherend material were determined following the methodology of Section 4.4.1. Microscopy images and traced welded areas of all spots can be found in Appendix A.

Figure 5.1 shows the measured welded areas of all specimens, split out into individual spots. Recall that the spot identifiers (s1 – s4) refer to the sequence in which the spots were originally welded. These sequences can be found in Figure 4.2 for the three joint layouts. It should be emphasized that, between the different layouts, the location of a spot with a certain identifier is not the same.

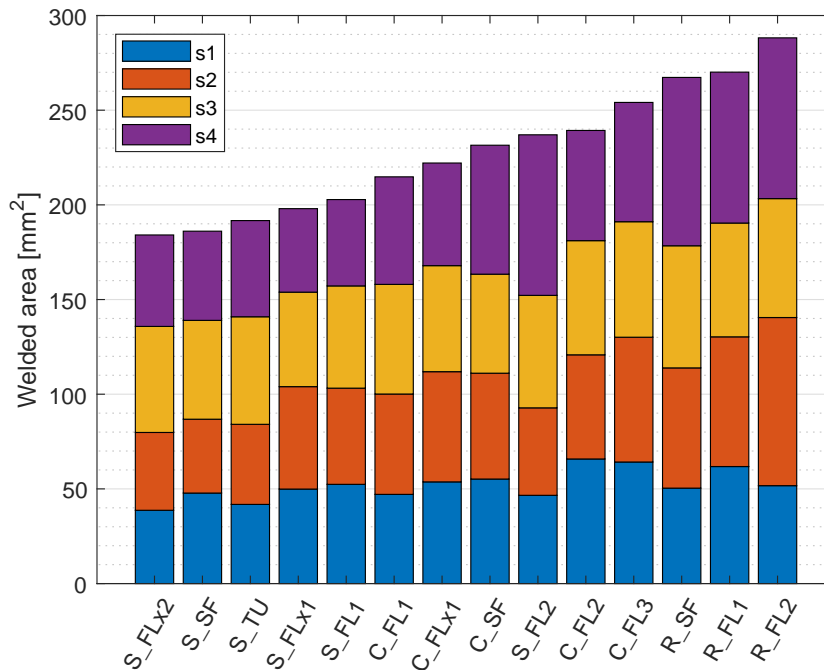


Figure 5.1: Welded areas as derived from microscopy images, split out into individual spots.

Results are shown in ascending order of total welded area. Two identified sources of outliers should be acknowledged when interpreting these results:

- Incidentally, an imprint was observed in which the circular outline of the sonotrode could be recognized. These imprints were visibly deeper than the more commonly seen cases and the measured welded area of these spots was significantly larger than average. Two such cases were encountered: S_FL2_s4 and R_FL2_s2. An example of this anomalous type of fracture surface can be seen in Figure 5.2.
- In all row specimens, secondary edge welding was observed during welding of s4. This secondary welding was included in measurement of the welded area of s4. Because of this, reported values for s4 of all row specimens are significantly larger than average.

Apart from the row specimens, in three cases some secondary welding was observed and included in measurement of the total welded area. These cases, together with the aforementioned anomalies, have been annotated accordingly in the summarized results in Table 5.2.

In acknowledgment of the fact that a weld identifier (s1 – s4) refers to a different spot location in each of the three joint layouts, Figure 5.3 separates the results by joint type. In these sub-graphs, welded area at a specific spot location can be compared directly across all specimens of that layout.

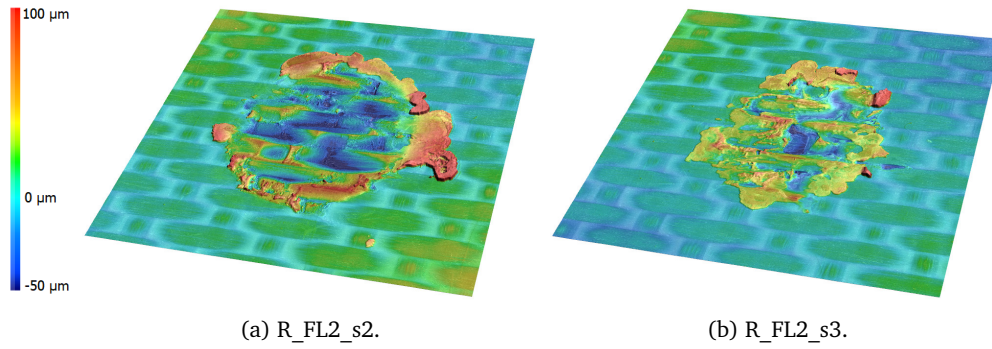


Figure 5.2: Example roughness image of a deeper-than-usual circular imprint (left), compared to a more commonly seen fracture surface in this research (right).

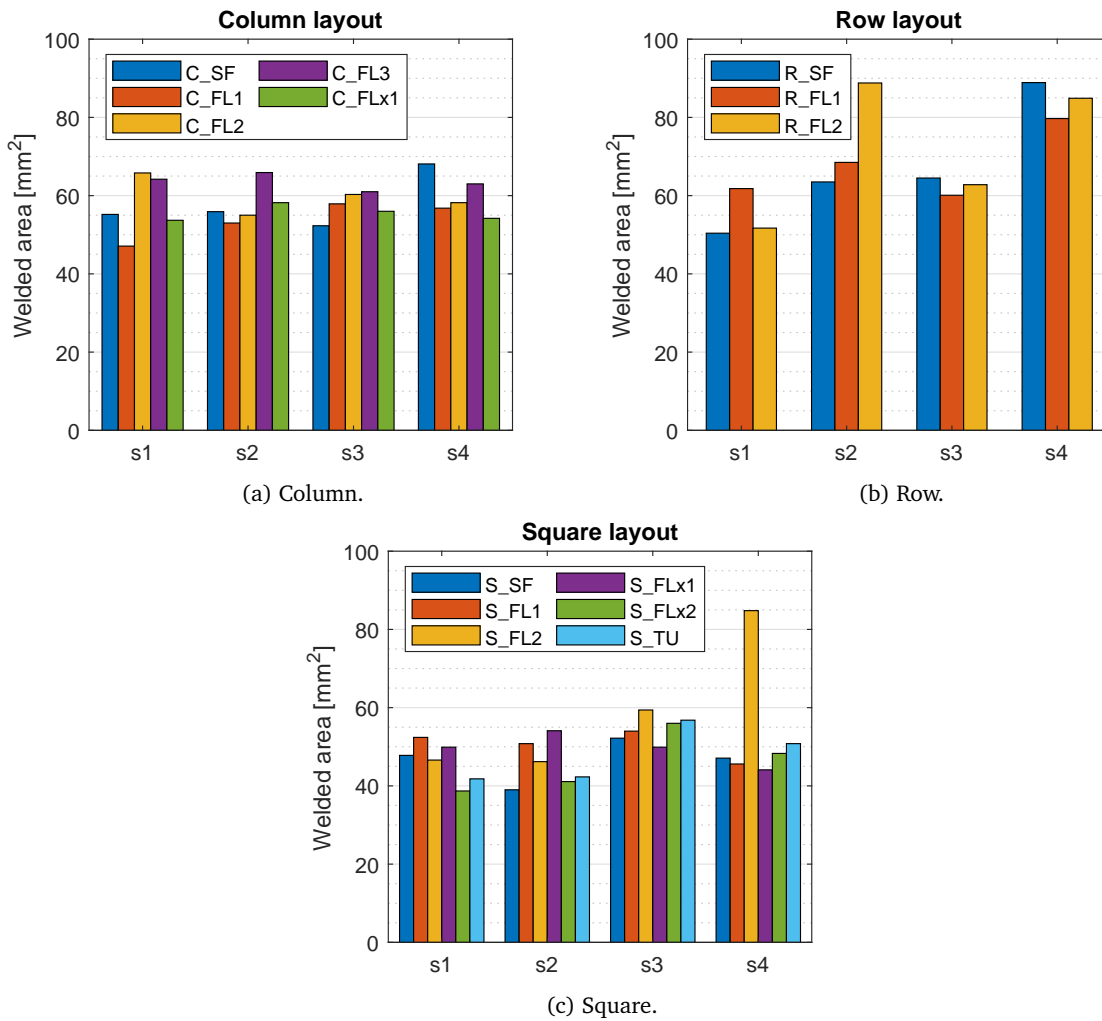


Figure 5.3: Welded area by spot weld location for the three different joint layouts.

To quantify warpage both top and bottom adherends (referring to position during welding) were considered. Results are presented in Figure 5.4, sorted by combined adherend warp angle. Although this sum itself is not a physical quantity and does not consider constraints imposed by clamping during welding, it indicates to what extent the final welded specimens deviated from a perfectly straight, non-warped state and how all specimens related to each other in this regard.

For all samples cut from the same laminate, warpage deforms that sample in the same direction. As a result, when placed in an overlap configuration, warpage in both adherends will mutually amplify the warp angle of the final welded specimen.

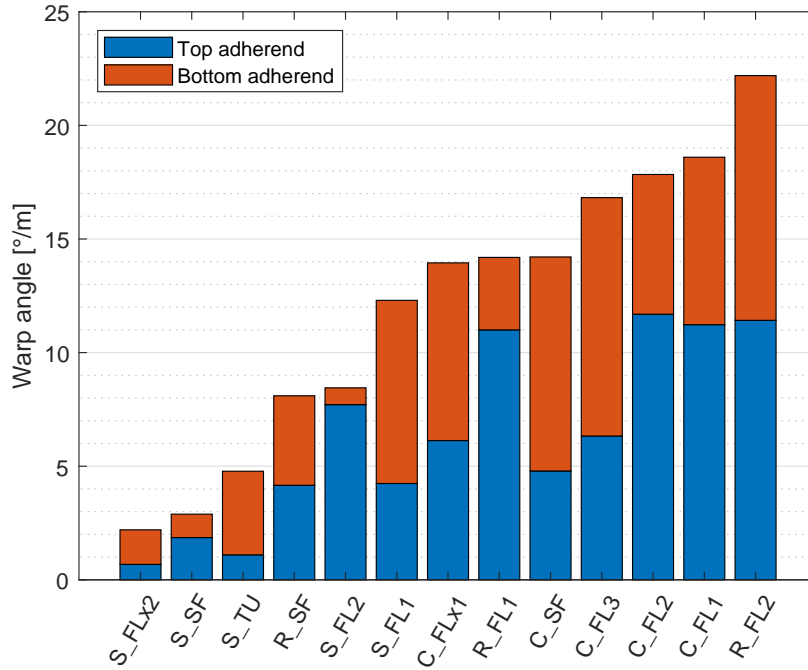


Figure 5.4: Warp angle of the top and bottom adherends of each specimen. Top/bottom refers to adherend position during welding.

Table 5.2 summarizes all results for welded area and warp angle as determined from surface microscopy images. Thickness, as measured with a thickness gauge, has also been included.

Table 5.2: Summarized welded areas and warp angles as derived from microscopy images.

Joint layout	Specimen	Welded area [mm ²]				Warp angle [°/m]		Thickness [mm]	
		s1	s2	s3	s4	θ_{top}	θ_{bot}	t_{top}	t_{bot}
Column	C_SF	55.2	55.9	52.3	68.1	4.79	9.42	1.83	1.84
	C_FL1	47.1	53.0	57.9	56.8	11.23	7.37	1.84	1.84
	C_FL2	65.8	55.0	60.3	58.2	11.69	6.15	1.84	1.83
	C_FL3	64.2	65.9	61.0	63.0	6.33	10.49	1.81	1.84
	C_FLx1	53.7	58.2	56.0	54.2	6.13	7.82	1.83	1.82
Row	R_SF	50.4	63.5	64.5	88.9 ¹	4.16	3.94	1.81	1.79
	R_FL1	61.8	68.5	60.1	79.7 ¹	11.00	3.19	1.80	1.80
	R_FL2	51.7	88.8 ²	62.8	84.9 ¹	11.42	10.77	1.80	1.80
Square	S_SF	47.8	39.0	52.2 ¹	47.1 ¹	1.86	1.03	1.89	1.90
	S_FL1	52.4	50.8	54.0	45.6	4.24	8.06	1.91	1.91
	S_FL2	46.6	46.2	59.4	84.8 ²	7.71	0.74	1.91	1.89
	S_FLx1	49.9	54.1	49.9	44.1	N/A ³	N/A ³	1.90	1.89
	S_FLx2	38.7	41.1	56.0	48.3 ¹	0.68	1.52	1.90	1.89
	S_TU	41.8	42.3	56.8	50.8	1.10	3.68	1.89	1.93

¹ For these spot welds, a certain amount of secondary welding was observed and included in the measured area.

² For these spot welds, a deeper imprint was observed than for other spots. In this imprint, the circular outline of the sonotrode could be recognized.

³ No results available: this specimen was crushed as a result of compressive loading.

5.2. Quasi-static test results

The load-displacement curves of the column, row and square specimens tested for ultimate failure load can be seen in Figure 5.5. From these graphs the ultimate load P_{ult} can be derived directly as the peak value of each respective curve. The shear strength and joint stiffness have been calculated according to Equations (4.1) and (4.2). The welded areas that were used to compute the shear strength have been reported previously in Section 5.1.

Table 5.3 summarizes the obtained joint parameters relating to quasi-static performance.

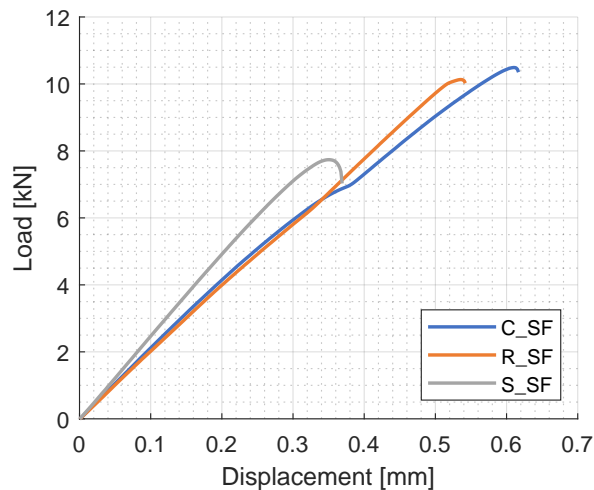


Figure 5.5: Load-displacement curves of the quasi-static test specimens.

Table 5.3: Quasi-static test results.

Specimen	P_{ult} [kN]	τ_{ult} [MPa]	JS [N/mm]
C_SF	10.487	45.3	21,184
R_SF	10.115	37.8	20,173
S_SF	7.546	40.6	24,588

5.3. Fatigue test results

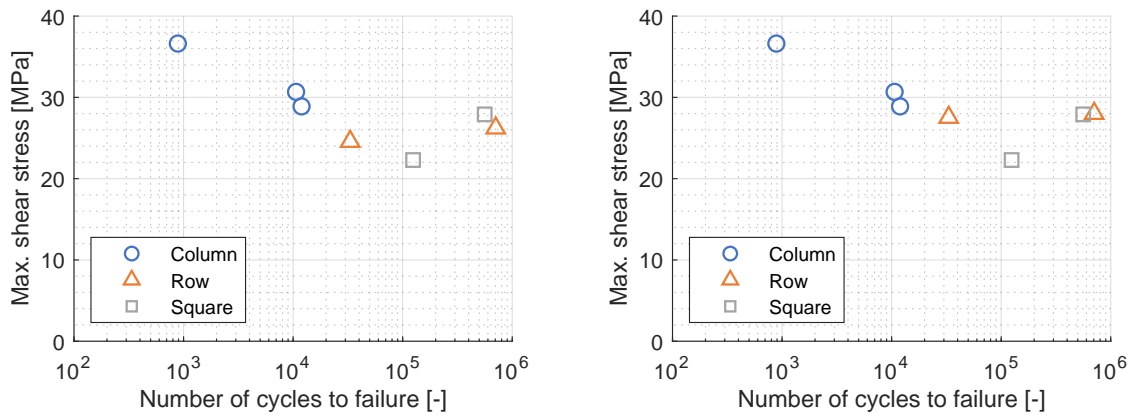
5.3.1. Fatigue life

For all fatigue tested four-spot specimens, the fatigue life (number of cycles to failure) was reported. This fatigue life was observed under a certain imposed maximum load, previously defined as 70% of the ultimate failure load for that joint layout. However, total welded area was previously seen to vary between specimens. As a result, the actual shear stress that a joint was subjected to was not the same for different test repetitions.

To account for this variability in welded area, maximum load was converted to maximum shear stress by division through the total welded area. This way, fatigue life results could be visualized in a semi-logarithmic stress-life diagram as shown in Figure 5.6.

Two variations of the stress-life diagram are shown: this is a result of the secondary welded area that was observed in all row specimens. Although this area of secondary welding will have had a certain load-carrying capability, it is unknown to what extent it contributed to the joint strength. As a result, the fatigue life diagram is shown for two possible edge cases: (a) one in which the secondary welded area contributed fully to the joint strength and (b) one in which it did not contribute at all. Of these two cases, (a) offers the most conservative estimation of joint performance.

The maximum load, maximum shear stress and number of cycles to failure of all considered specimens are summarized in Table 5.4. It should be noted that, for R_FL2, a cracking sound was heard during the initial load ramp prior to cyclic loading. It should also be mentioned that C_FL1 and S_FL1 were tested at a load level of 75%, as during initial tuning a load level of 70% briefly seemed to result in test times exceeding the time available for experiments.



(a) Full contribution from secondary welding.

(b) No contribution from secondary welding.

Figure 5.6: Stress life diagram showing all three joint layouts. Two edge cases are shown for the row specimens, in which the observed secondary edge welding either (a) fully contributed to the joint strength or (b) did not contribute at all.

Table 5.4: Imposed maximum load and shear stress and resulting number of cycles to failure.

Joint layout	Specimen	P_{max} [kN]	τ_{max} [MPa]	N_{fail} [-]
Column	C_FL1	7.866	36.6	887
	C_FL2	7.341	30.7	10,645
	C_FL3	7.341	28.9	11,943
Row	R_FL1	7.081	26.2	706,630
	R_FL2	7.081	24.6	33,188
Square	S_FL1	5.660	27.9	560,870
	S_FL2	5.283	22.3	124,478

5.3.2. Cyclic load and displacement data

Cyclic peak-valley load and displacement data were monitored during the fatigue tests. In this section these data, plotted against number of cycles, are displayed for the seven specimens that were considered in the fatigue analysis. Since these tests were performed in a load-controlled manner, the peak load shows as as mostly constant over time.

As with previously presented results, a couple of factors should be acknowledged when interpreting the cyclic load and displacement data:

- For unknown reasons, network errors would sometimes result in an emergency shutdown of the fatigue machine and therefore an interruption of the test. During the following downtime the specimen remained clamped in the machine. As a result, specimens would experience a tensile load from clamp and piston weight whenever an emergency shutdown occurred.

Machine downtime was seen to result in disruptions in the displacement curve, as highlighted in Figure 5.7. In this specific case, after 42 minutes of downtime it took over 5,000 cycles for the displacement graph to return to its original path.

In two cases, a network error occurred overnight and as a result that test was interrupted for an extended period of time. All cases of network errors and their resulting machine downtime have been summarized in Table 5.5, with the two overnight cases highlighted.

- When the fatigue life of the column specimens was observed to be shorter than that of the other

layouts (see Section 5.3.1), it was decided to lower the DIC interval for C_FL3 from 1,000 to 50 cycles to obtain more data on damage evolution. However, it was previously identified that after a DIC dwell it took approximately 25 cycles for the maximum load to match its control value again.

Figure 5.8 shows the effect this has on displacement data with a low DIC interval. It becomes clear that this specimen was subjected to a lower-than-intended load for about 50% of the total test duration. This is a much larger portion of its total fatigue life than is the case for the other specimens, where an interval of 1,000 cycles was used.

- In some specimens, noise was observed in the control load. This was seen most clearly for specimens R_FL1 (Figure 5.13) and, to a lesser extent, S_FL1 (Figure 5.15). It is expected that this noise is a result of varying oil pressure levels, which in itself would be a result of tests being run simultaneously on other servo-hydraulic test machines in the lab.
- Specimen R_FL2 slipped from the grips over the course of the first 12,000 cycles. After the specimen had come loose completely, the test was interrupted and the specimen was clamped again. As a result, the peak displacement curve for this specimen (Figure 5.14) is split into two parts with different slopes.

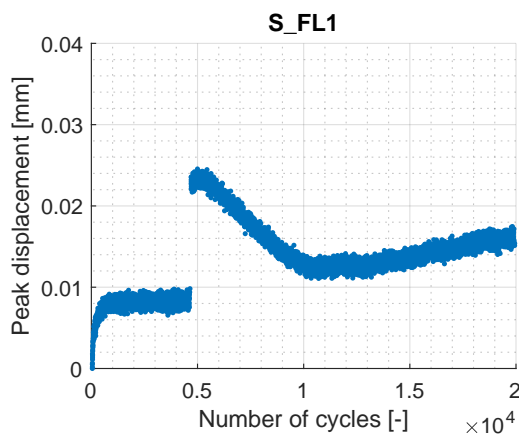


Figure 5.7: Effect of machine downtime, during which the specimen remained under a certain static load, resulting from incidental network errors.

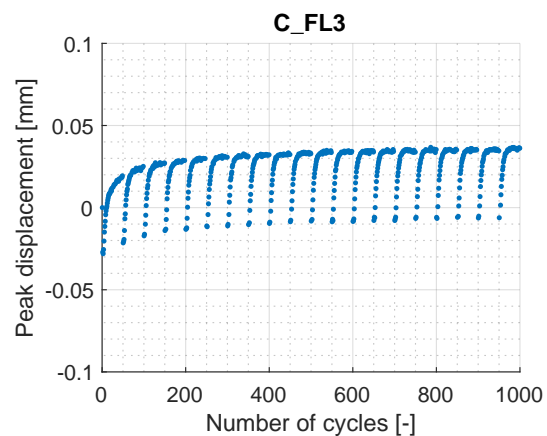


Figure 5.8: Effect of a low DIC interval on peak displacement values.

Table 5.5: Occurrences of network errors and resulting machine downtime.

Specimen	Cycles	Downtime	Specimen	Cycles	Downtime
	383,879	00:01:33		4,654	00:42:16
	384,579	00:00:51		47,653	00:08:52
	385,328	00:03:44		53,849	01:02:24
	453,251	00:10:32		102,590	13:07:52
R_FL1	455,062	00:37:26	S_FL1	156,969	00:03:47
	486,311	14:00:29		157,659	00:01:03
	544,281	00:13:32		158,874	00:00:30
	550,078	00:18:45		165,807	00:03:04
	619,112	00:01:32		198,574	00:00:45

The load and displacement graphs for all specimens considered in fatigue analysis can be found in Figures 5.10 to 5.16.

From the cyclic displacement data a gradual increase in peak displacement was observed for all specimens. To evaluate if this increase could be attributed directly to evolution of damage within the joint, a non-welded CF/PPS adherend was tested under the same fatigue conditions.

As seen in Figure 5.9, the initial shape of the displacement graph for this sample is comparable to that of the welded specimens: this indicates that the gradual increase in displacement can not be directly attributed to damage evolution within the joints. Note that R_FL2 experienced slip in the grips, which explains the different slope observed for this specimen.

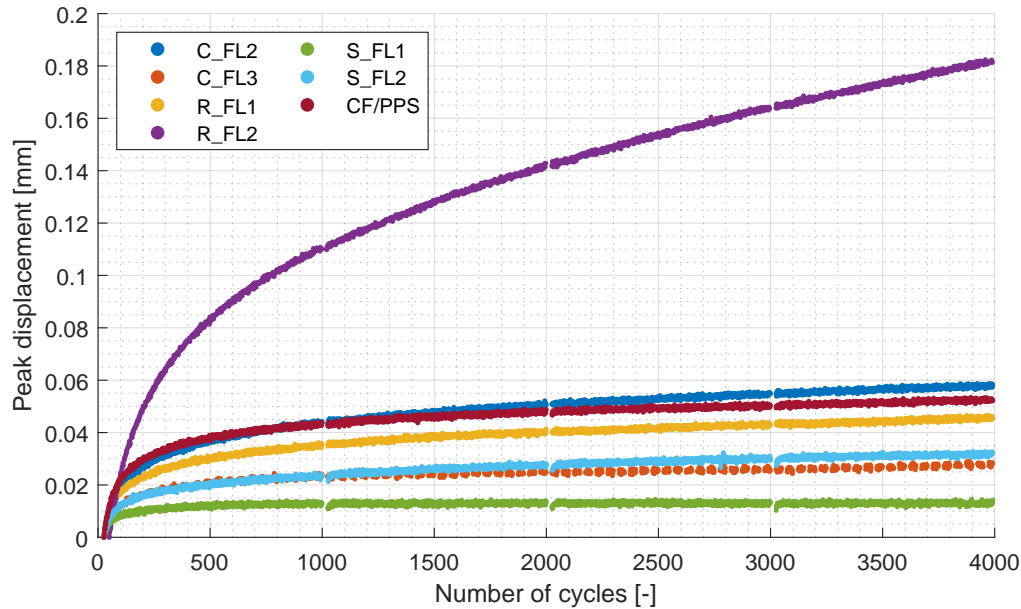


Figure 5.9: Shape comparison of cyclic displacement data to base CF/PPS material.

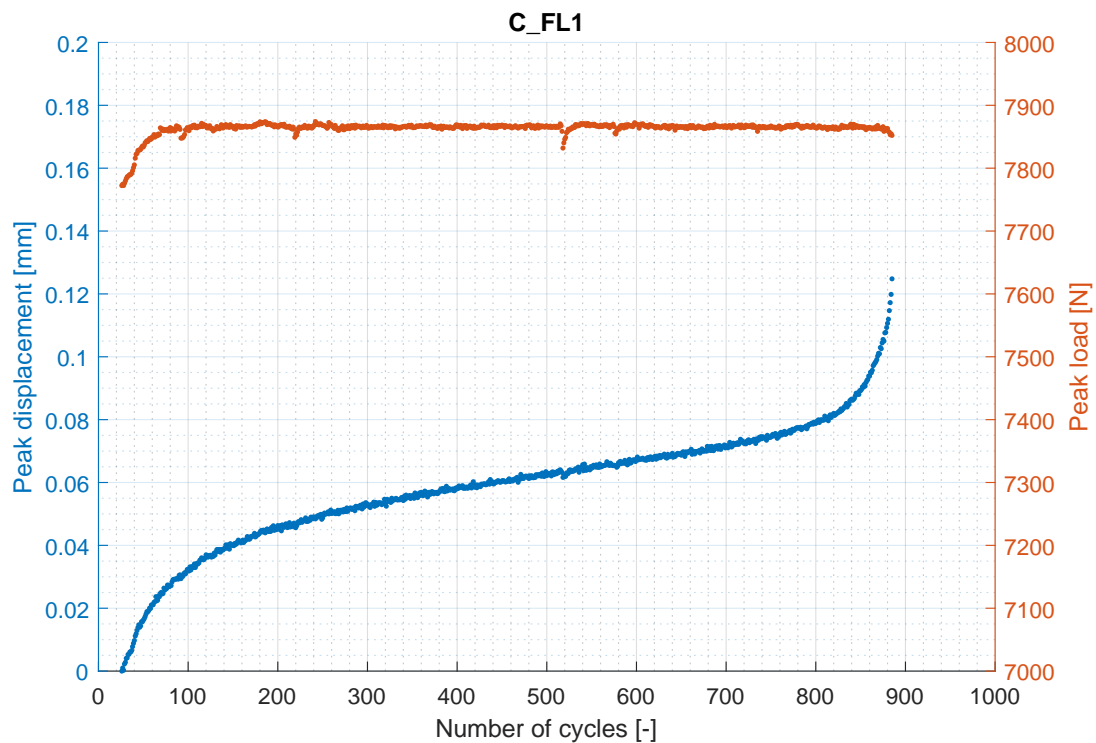


Figure 5.10: Cyclic peak load and displacement data – C_FL1.

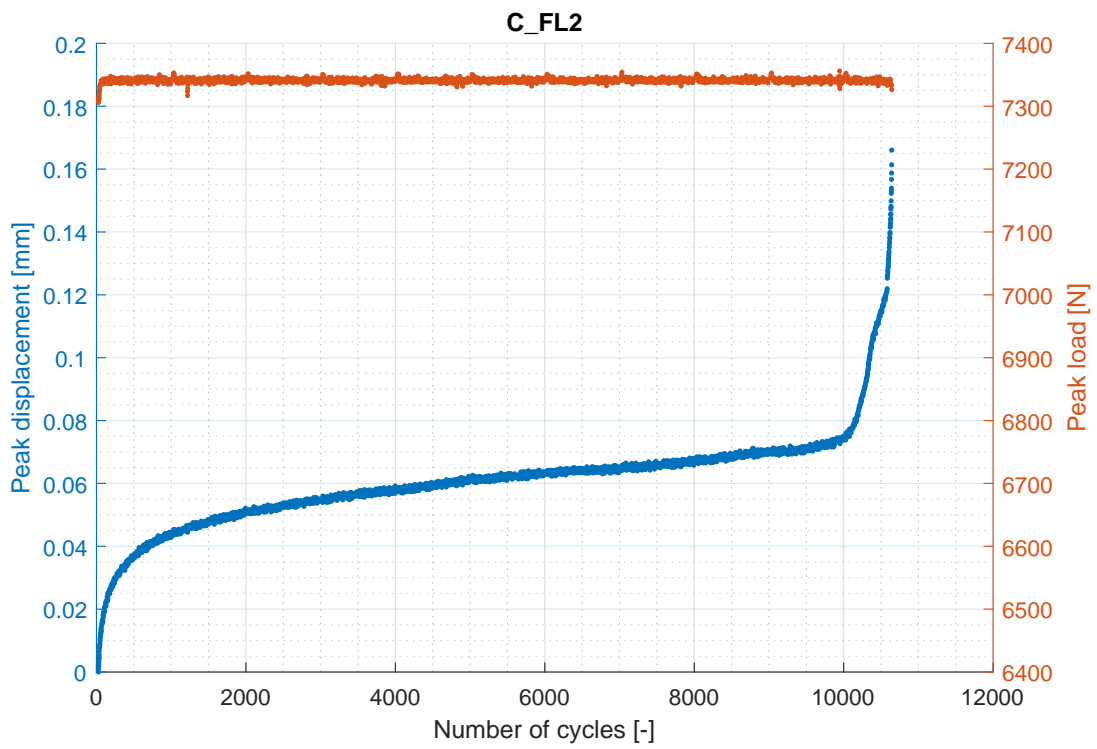


Figure 5.11: Cyclic peak load and displacement data – C_FL2.

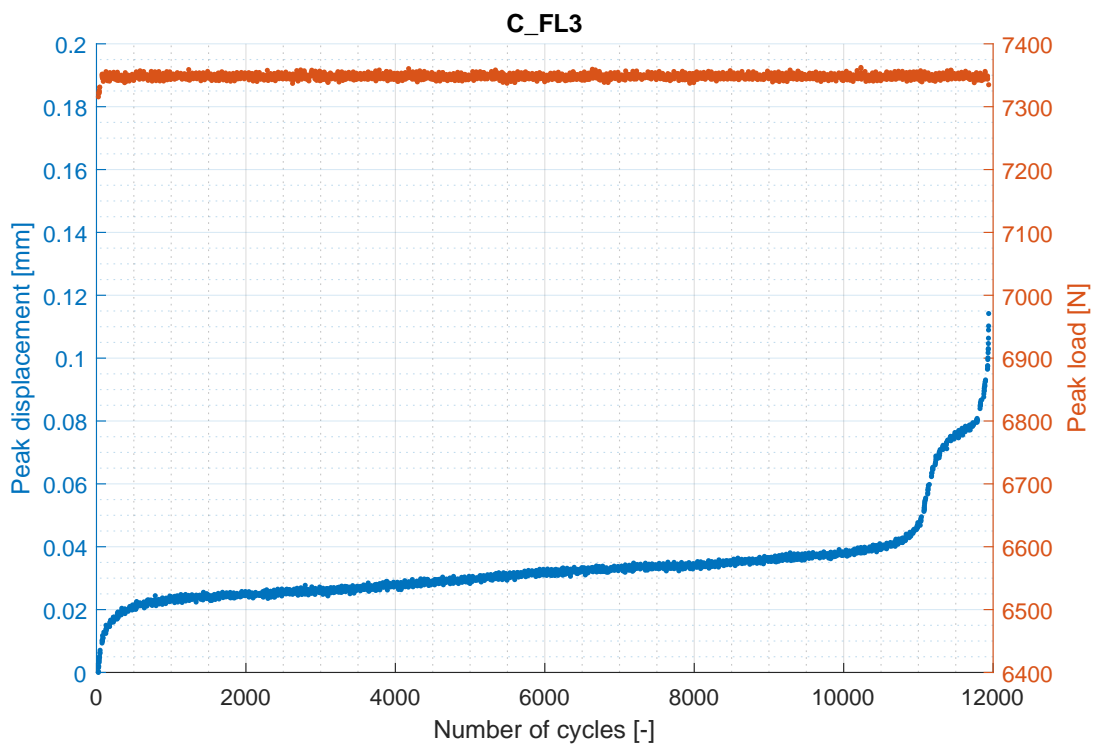


Figure 5.12: Cyclic peak load and displacement data – C_FL3.

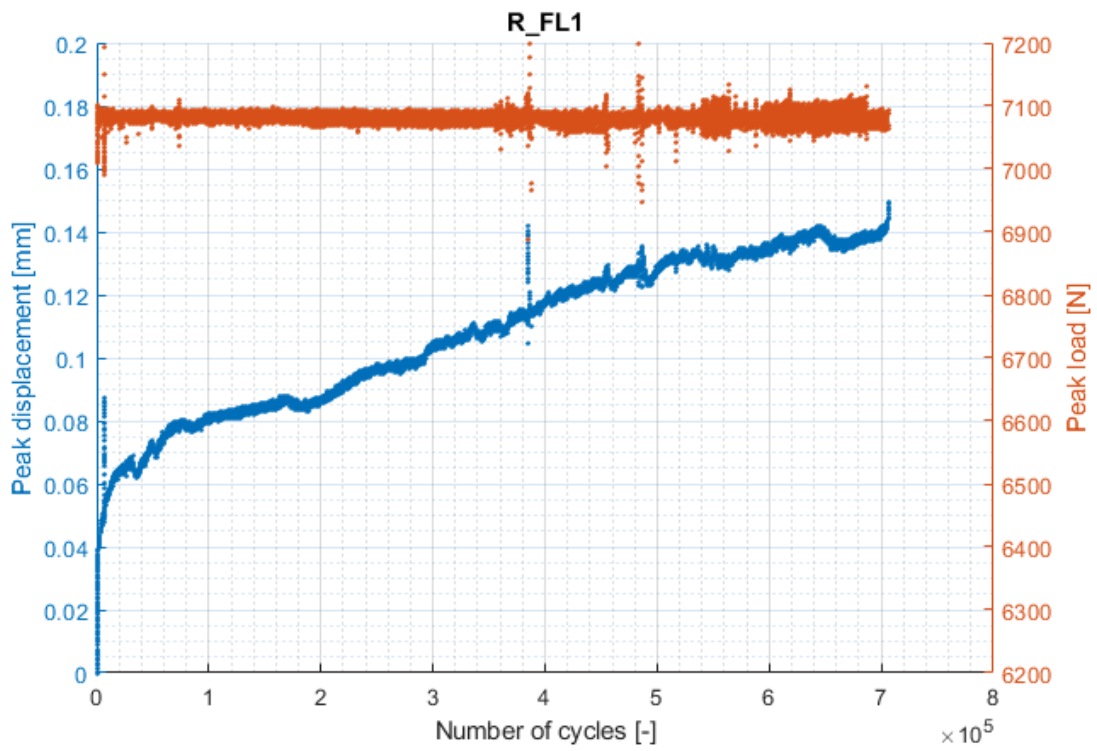


Figure 5.13: Cyclic peak load and displacement data – R_FL1.

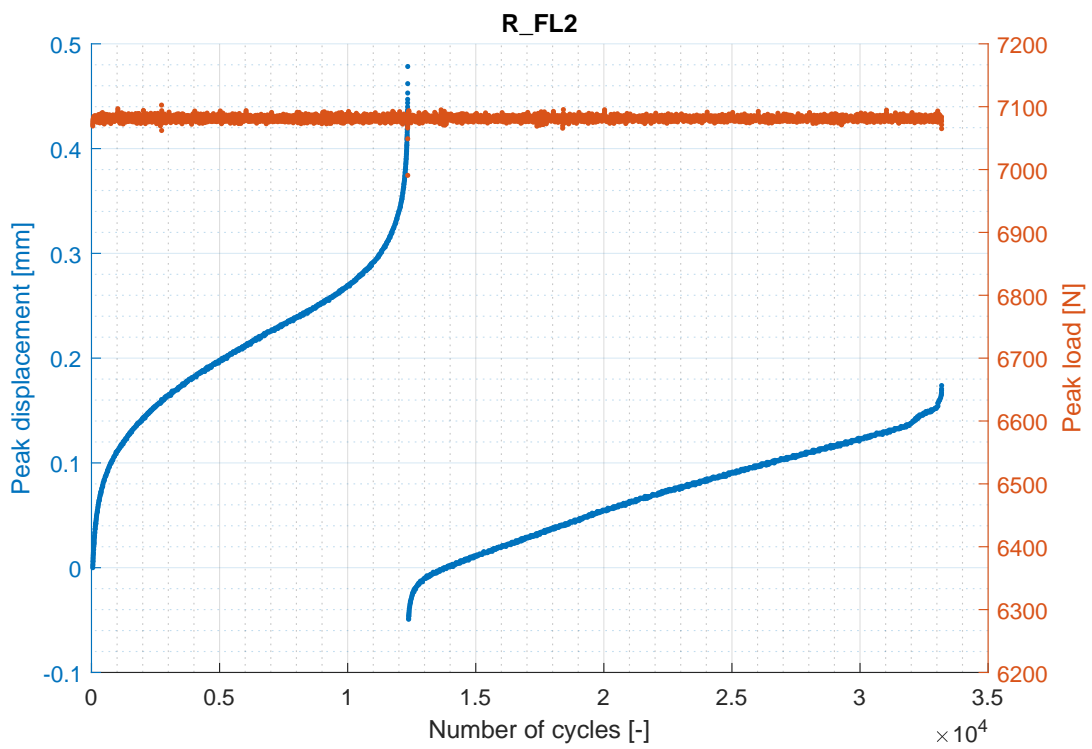


Figure 5.14: Cyclic peak load and displacement data – R_FL2.

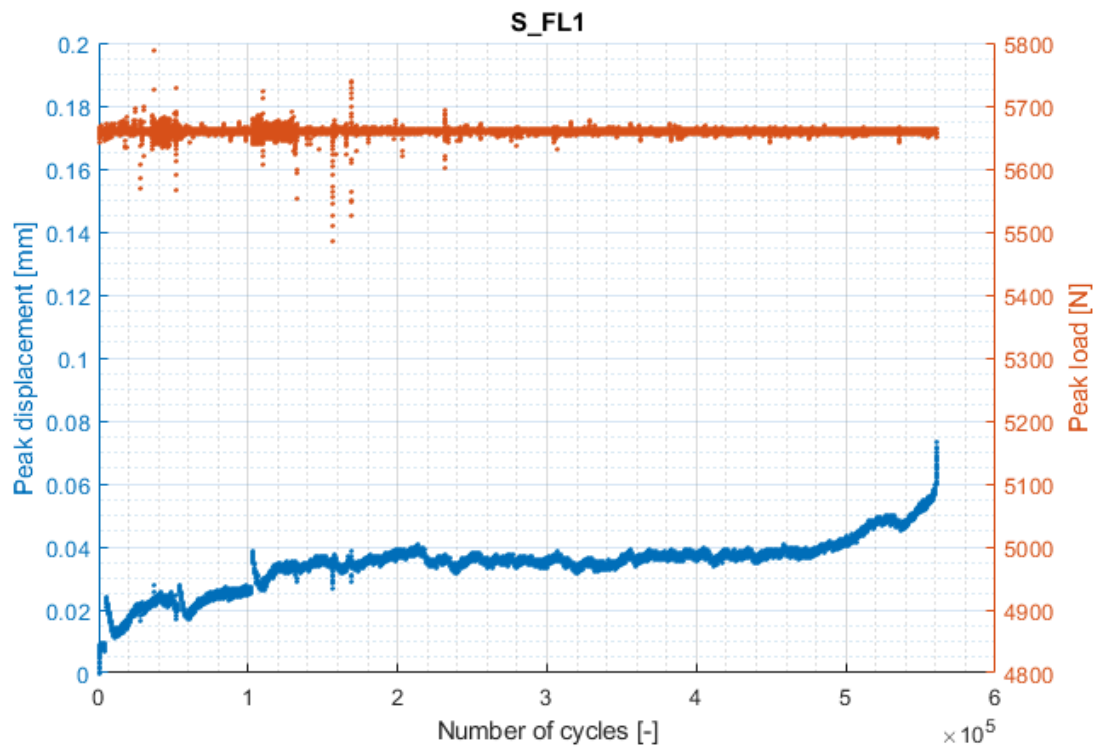


Figure 5.15: Cyclic peak load and displacement data – S_FL1.

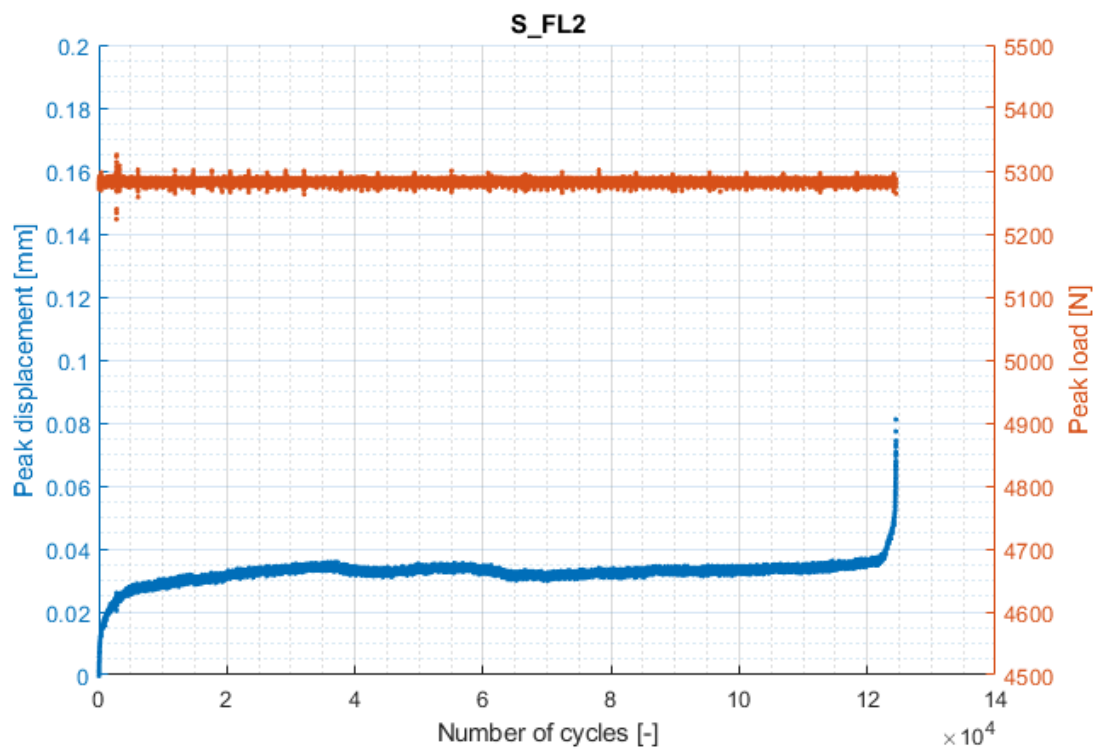


Figure 5.16: Cyclic peak load and displacement data – S_FL2.

5.3.3. Digital image correlation

DIC photos were taken in a (close to) unloaded state and processed as described in Section 4.4.3. For the column and row specimens, line graphs are presented that display out-of-plane displacement over a line passing through all four spots. These are found in Figures 5.17 and 5.18 (column) and Figures 5.19 and 5.20 (row). For the square layout, four graphs were derived per specimen: longitudinal and transverse lines, each passing through two spots. Graphs for S_FL1 and S_FL2 can be found in Figures 5.21 to 5.28. Note that, for S_FL2, photos were taken in a loaded condition.

Out-of-plane displacement was also evaluated at the spot locations: these graphs were used mostly as verification. For completeness, these graphs have been included in Appendix B.

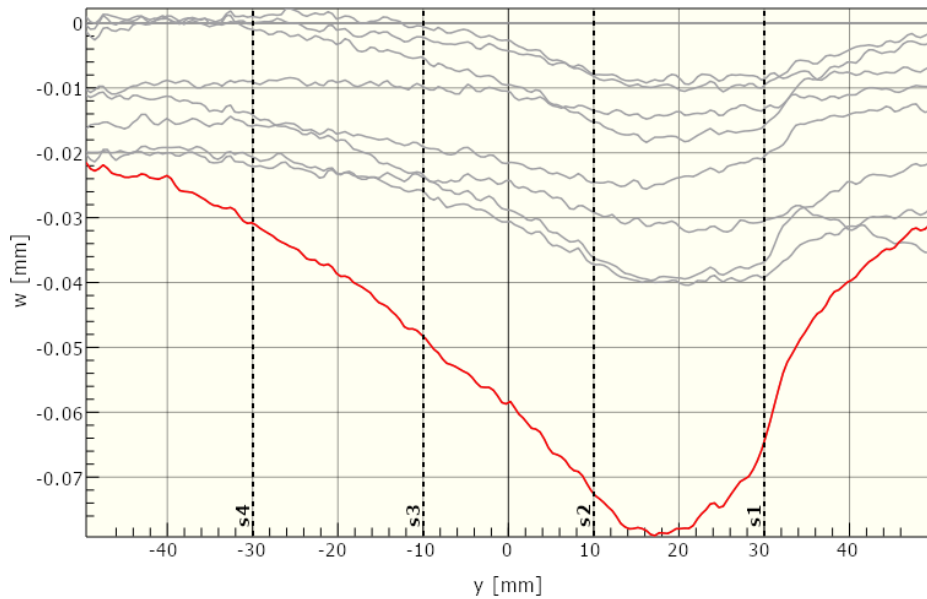


Figure 5.17: Out-of-plane displacement with time over longitudinal center-line – C_FL2.

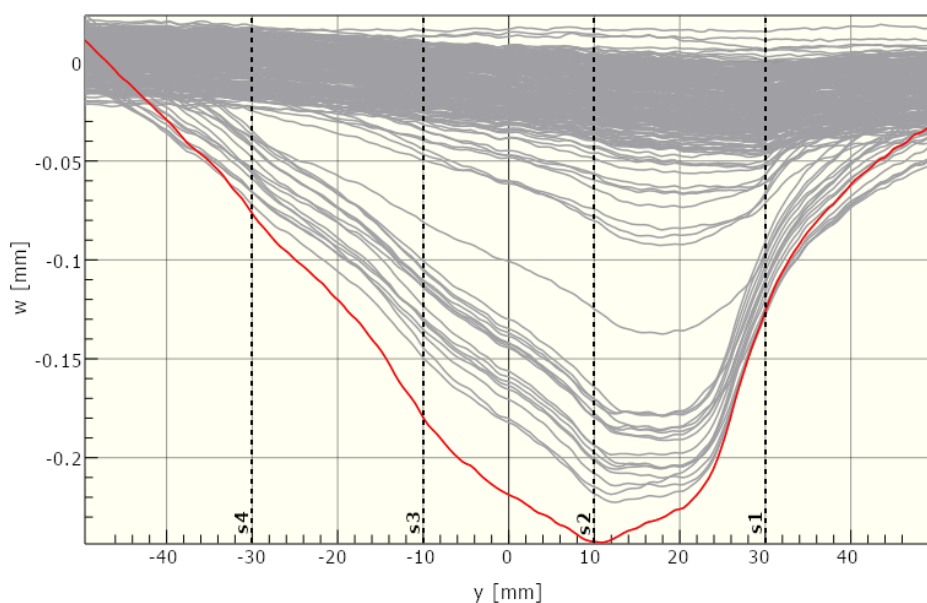


Figure 5.18: Out-of-plane displacement with time over longitudinal center-line – C_FL3.

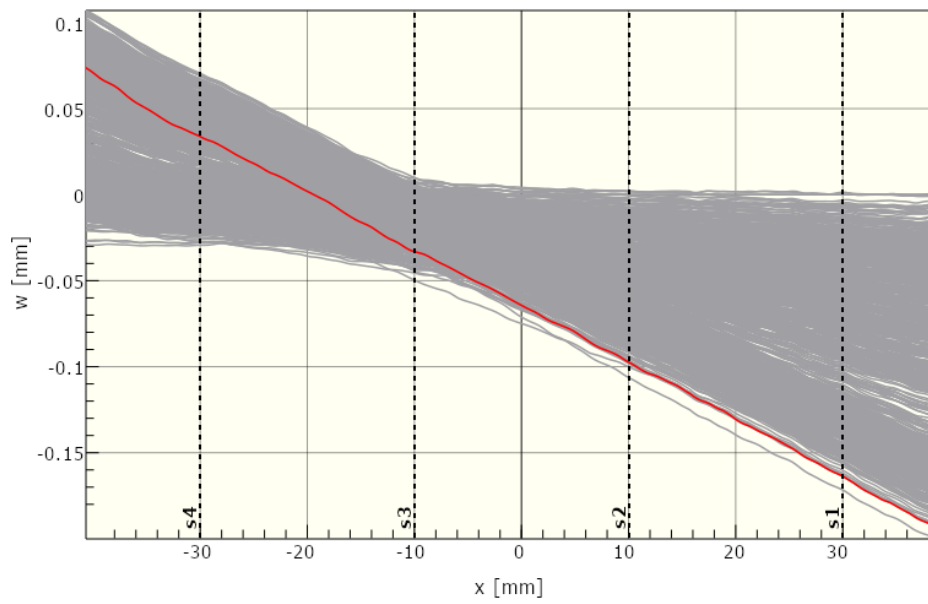


Figure 5.19: Out-of-plane displacement with time over transverse center-line – R_FL1.

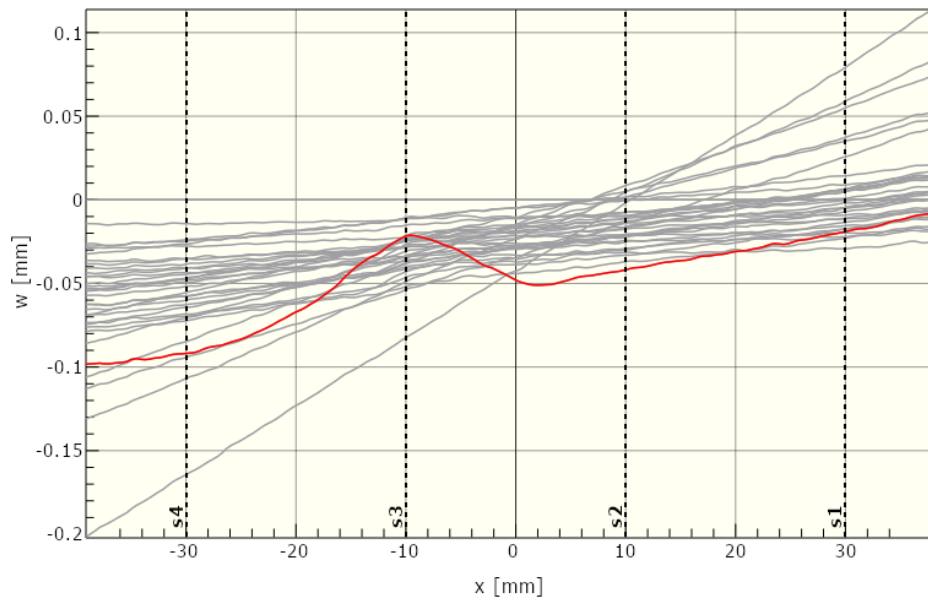


Figure 5.20: Out-of-plane displacement with time over transverse center-line – R_FL2.

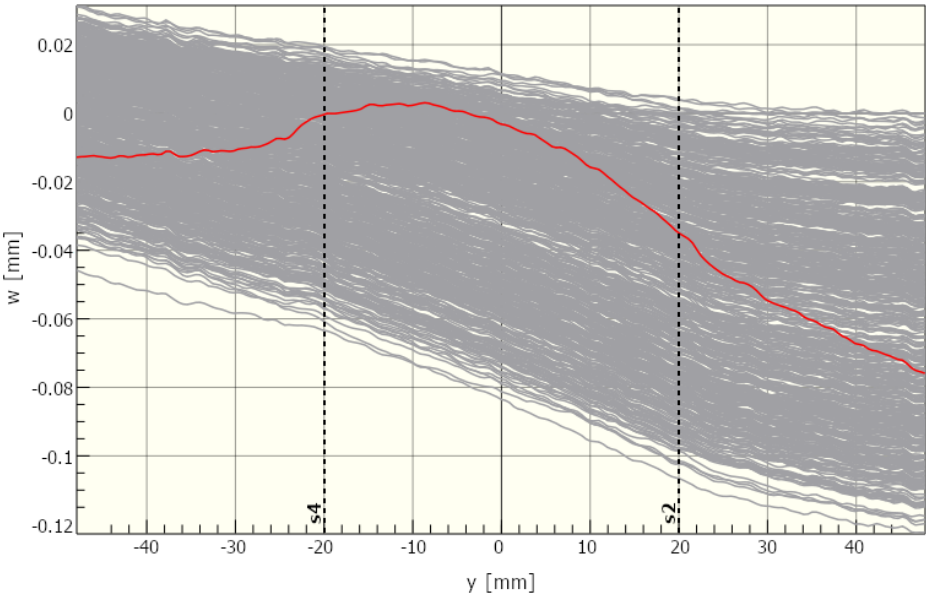


Figure 5.21: Out-of-plane displacement with time over longitudinal line (s2, s4) - S_FL1.

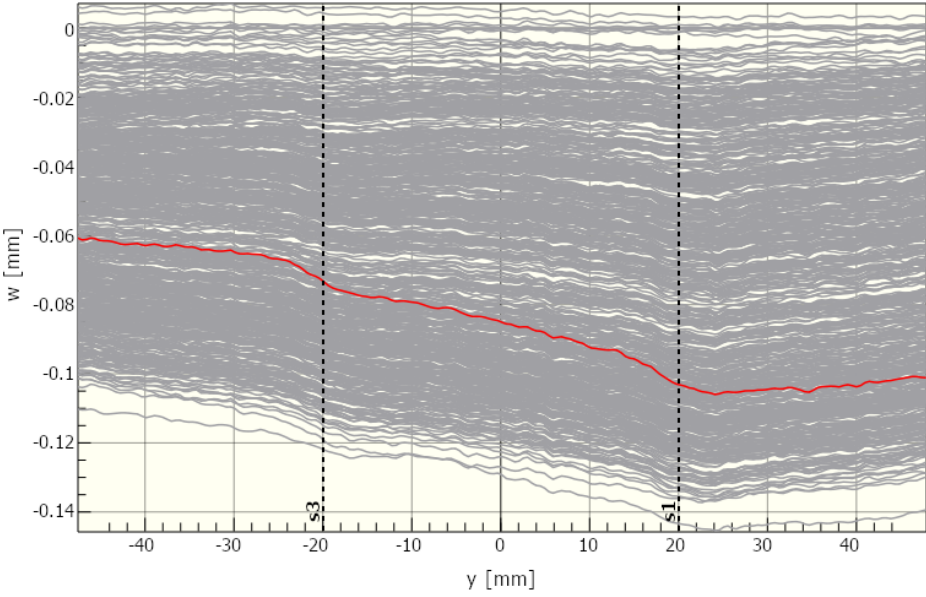


Figure 5.22: Out-of-plane displacement with time over longitudinal line (s1, s3) - S_FL1.

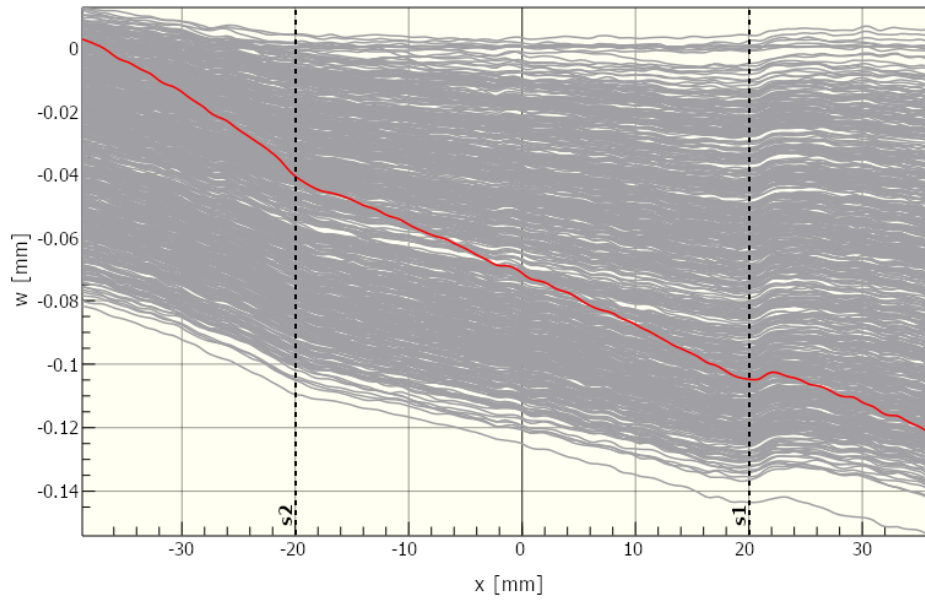


Figure 5.23: Out-of-plane displacement with time over transverse line (s1, s2) – S_FL1.

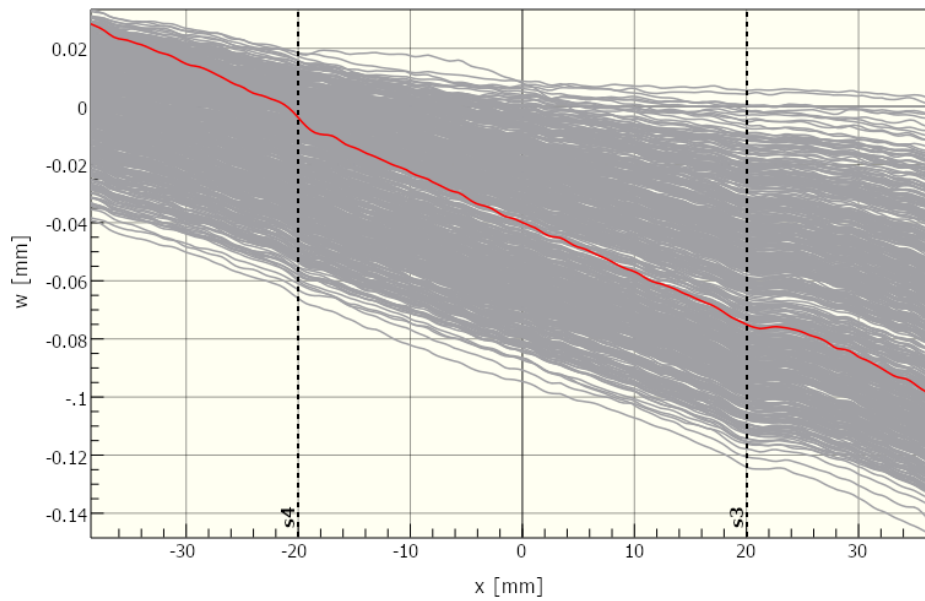


Figure 5.24: Out-of-plane displacement with time over transverse line (s3, s4) – S_FL1.

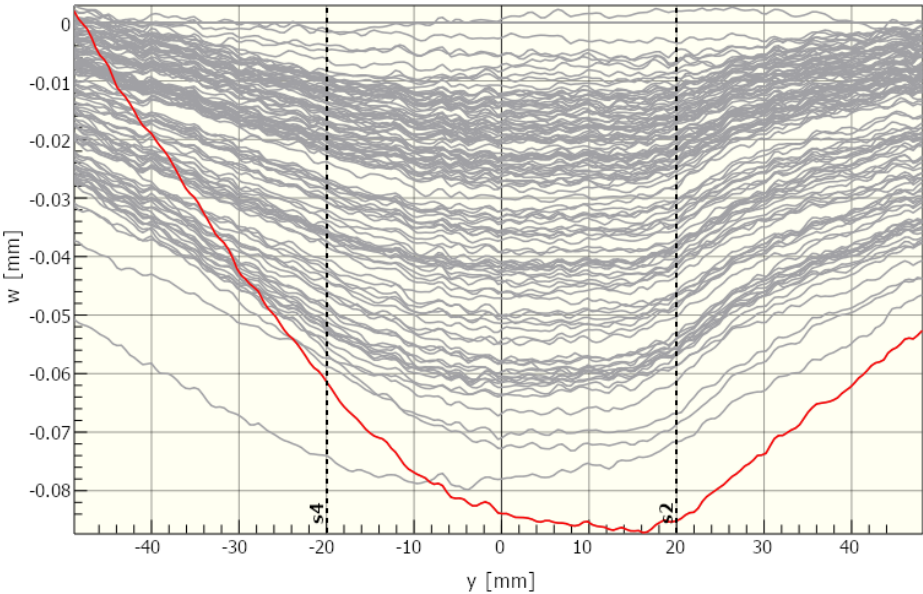


Figure 5.25: Out-of-plane displacement with time over longitudinal line (s2, s4) – S_FL2.

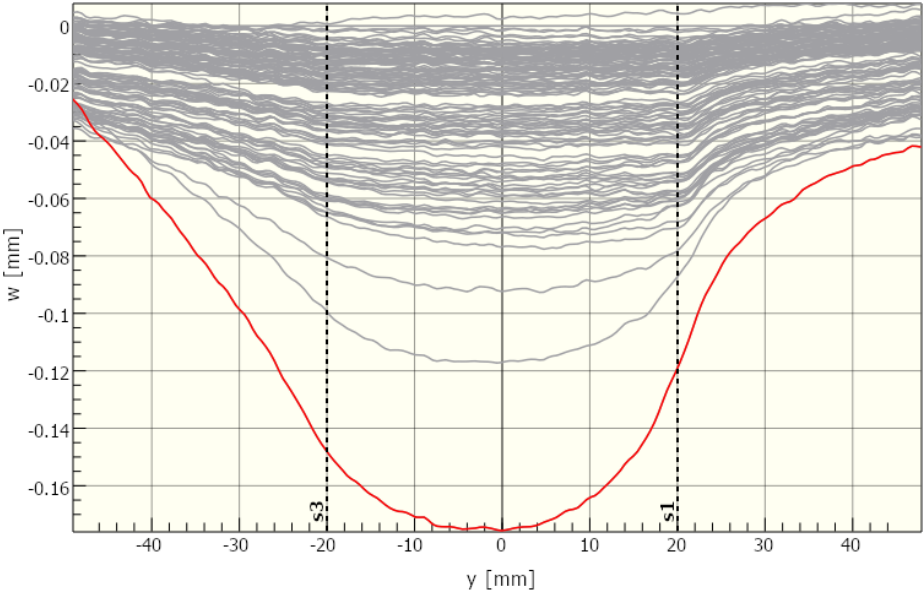


Figure 5.26: Out-of-plane displacement with time over longitudinal line (s1, s3) – S_FL2.

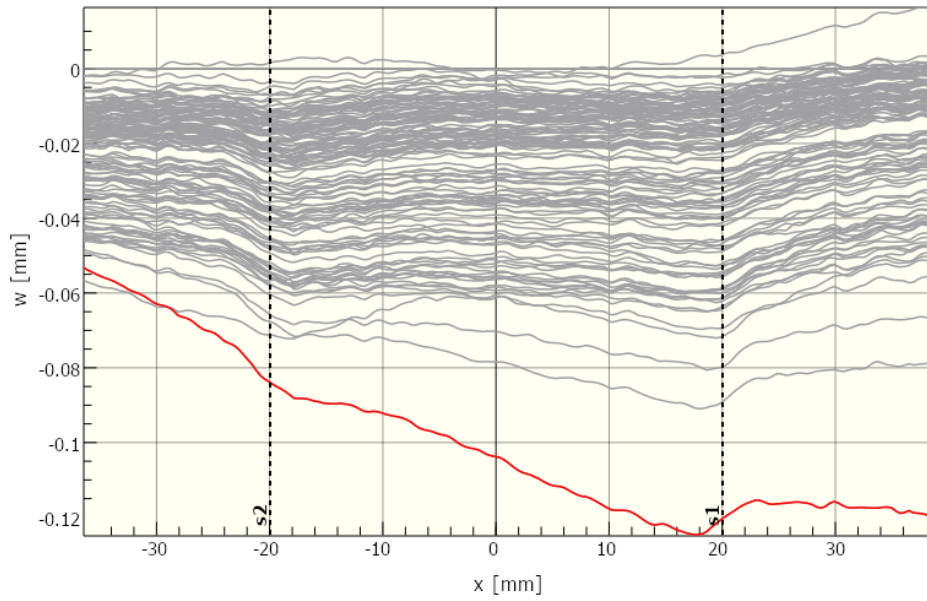


Figure 5.27: Out-of-plane displacement with time over transverse line (s1, s2) – S_FL2.

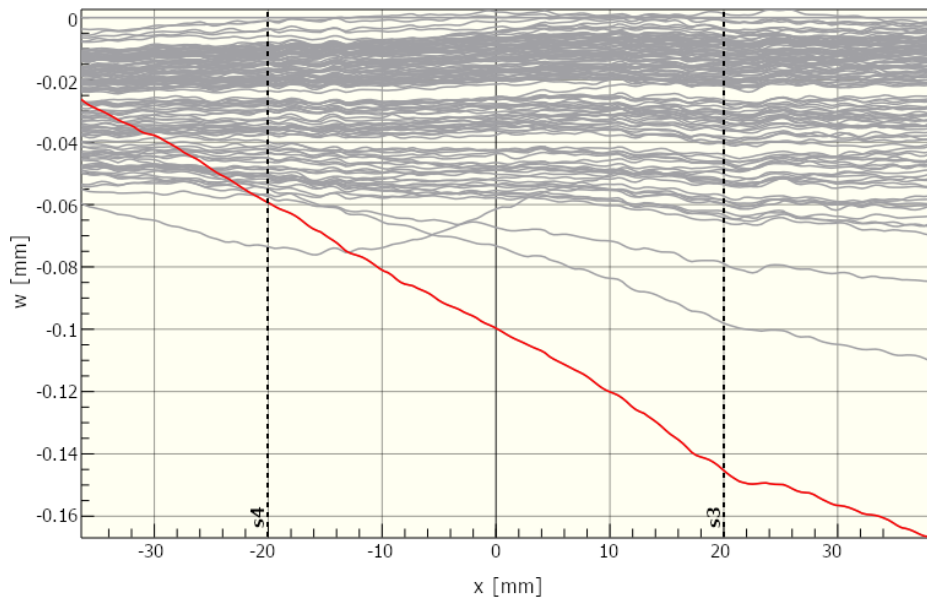


Figure 5.28: Out-of-plane displacement with time over transverse line (s3, s4) – S_FL2.

5.4. Single spot weld laminate comparison

As part of a weld quality consistency analysis, single spot welds were created on samples cut from the three laminates corresponding to column, row and square joints. All specimens were welded following the procedure described in Section 4.2.2, in single lap configuration and with overlap dimensions of 25.4 mm \times 25.4 mm. These dimensions are in accordance with earlier work from Zhao et al. [27] and were chosen sufficiently large to accommodate a single spot weld in the center of the overlap area. These welds were tested for ultimate failure load in a displacement-controlled tensile shear test at a rate of 1.3 mm/min, in accordance with ASTM standard D1002 [41].

Two forms of data acquisition were used. During the tests, applied load and cross-head displacement were monitored. After testing, the welded area was determined through image analysis of the fracture surfaces. With these combined data two weld quality parameters were calculated: the shear strength τ_{ult} , using Equation (4.1), and the joint stiffness JS , as defined in Equation (4.2).

The load-displacement data as monitored during the tests can be seen in Figure 5.29. The obtained numerical results are summarized in Table 5.6. In this table, adherend thicknesses are reported as well.

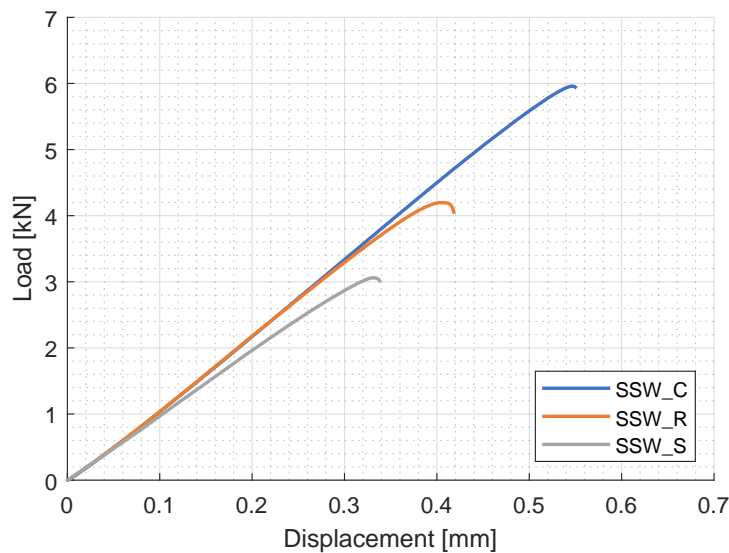


Figure 5.29: Load-displacement data of the single spot welds used for laminate comparison.

Table 5.6: Summary of single spot weld test results.

Specimen	WA [mm ²]	P_{ult} [kN]	τ_{ult} [MPa]	JS [N/mm]	t_{top} [mm]	t_{bot} [mm]
SSW_C	179.2 ¹	5.959	33.3	10,929	1.82	1.83
SSW_R	95.9 ²	4.198	43.8	10,886	1.80	1.79
SSW_S	66.5 ³	3.060	46.0	9,805	1.90	1.90

¹ Consisting of 98.3 mm² at the spot location and 80.9 mm² from secondary welding.

² Consisting of 85.8 mm² at the spot location and 10.1 mm² from secondary welding.

³ Consisting of 57.3 mm² at the spot location and 9.2 mm² from secondary welding.

6

Discussion

This chapter provides the reader with a thorough discussion of the obtained results. First of all, weld quality and consistency are addressed in Section 6.1, since this serves as an important foundation for further interpretation of the fatigue results. Next up, Section 6.2 discusses the possibility of column joints already getting damaged prior to cyclic loading due to an uneven load distribution, and how this might affect test results. Section 6.3 then discusses the obtained fatigue results based on three aspects that characterize joint fatigue behavior: fatigue life, failure modes and damage evolution through the joint. This observed fatigue behavior in TPCs is compared to that in steel and it is assessed to what extent existing knowledge on steel joints could be transferred to TPCs.

6.1. Weld quality and consistency

When analyzing the fatigue results of the four-spot welded joints, it is important to be aware of any external factors that might be affecting the obtained test results. The main focus of this section was to identify to what extent results could be compared between different joint layouts, and if different repetitions of the same test could be assumed to be similar.

In Section 6.1.1, these two questions are addressed. Section 6.1.2 then briefly reflects on the main observations in transferring a control strategy for small column joints to large four-spot welded joints with various spot arrangements. To recap, Section 6.1.3 summarizes the main findings with regard to weld quality and consistency.

6.1.1. Laminate variations and effects

All three laminates used in this research comprised the same layup and material combination and were manufactured in a theoretically identical manner, as described in Section 4.2.1. However, unidentified variations in the manufacturing process might still cause differences between the laminates. These differences could affect weld quality and subsequent joint performance.

This possibility was acknowledged and, in anticipation, each laminate was allocated to a single joint layout. The underlying assumption was that different repetitions of tests on one joint layout would now be affected by as few external variations as possible. On the other hand, more caution should be exercised when comparing test results between the different joint layouts.

In following this approach, two main questions came up regarding the validity of its underlying assumptions and the degree of consistency of geometric material properties:

1. *To what extent does using a different laminate affect subsequent weld quality?*
2. *Are the thickness and warp angle of different samples, cut from the same laminate, consistent? If not, is there a correlation between variations in these properties and observed weld quality?*

Answering these questions would allow a more informed comparison (1) between test results of the different joint layouts and (2) between results found for different test repetitions of the same layout. In the remainder of this section, both questions are addressed subsequently.

With regard to geometric properties, material thickness and warp angle were considered. Adherend length and width were not considered, since the actual overlap area is defined by the spot welds themselves rather than the exact overlap dimensions. Small differences in adherend length and width were therefore not expected to affect weld quality in any way.

1. *To what extent does using a different laminate affect subsequent weld quality?*

To answer this question, single spot welds were created on samples from all three laminates. This way, the potential effect of spot arrangement on weld quality was eliminated and a comparison could be made based solely on differences between the laminates. The joints were tested for static strength and the welded area was determined. With the acquired data two weld quality parameters were calculated: shear strength and joint stiffness. Results of this analysis were presented in Section 5.4: Figure 5.29 shows the quasi-static load-displacement curves and Table 5.6 summarizes the obtained numerical values. Warpage was not evaluated for these samples, due to the fact that the warp angle was seen to vary substantially within the laminates.

In this weld quality analysis, only a single sample from each of the laminates was considered due to limitations in time and material availability. Considering that one of the three created spot welds showed an anomalous fracture surface with a large portion of secondary welded area, it becomes clear that more test repetitions are needed to draw conclusions from the presented results with a fair degree of confidence. Still, one observation on the square sample corroborated something also seen in the four-spot joints, as will be explained in more detail below. This did serve to show that identified behavior for welds on this laminate occurred regardless of joint layout.

Figure 6.1 shows the fracture surfaces of the three welds. From these images, some differences are observed. Firstly, the spot weld on the square laminate has a notably smaller welded area than those welded on the column and row samples. This is in line with what was also observed in the four-spot square specimens: save for one identified outlier, all the square specimens had a smaller total welded area than the row and column ones. Secondly, a lot of secondary welding is observed on the column sample. It is unknown what caused this, but it is considered to be an anomaly and not related to the sample itself. It should be noted that, at the location of the spot itself, the row and column sample show a comparable amount of welded area.

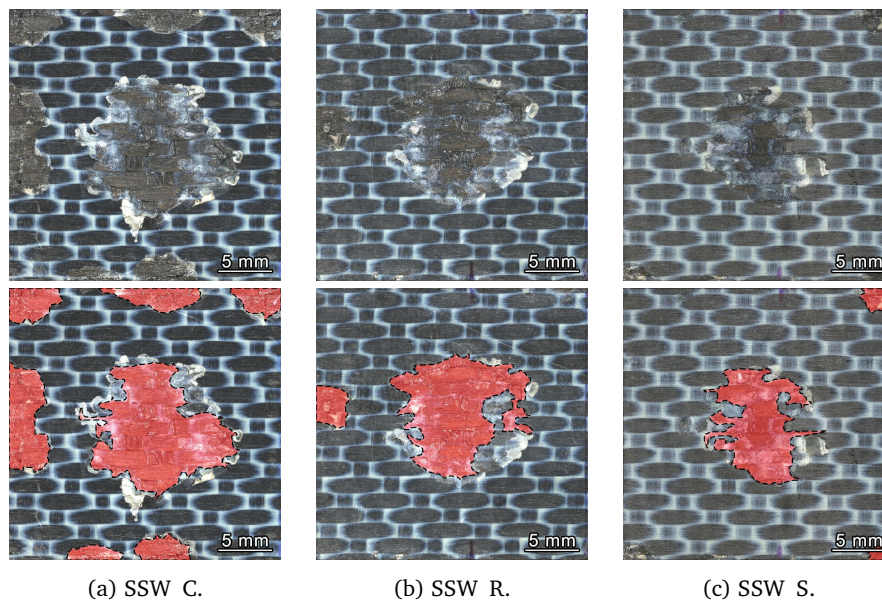


Figure 6.1: Visual comparison between single spot welds on the three laminates used for column (C), row (R) and square (S) specimens.

The shear strength was calculated taking into account not only welding at the spot weld location, but also secondary welding. However, at 33.3 MPa the shear strength of the column sample is seen to be substantially lower than that of the row and square samples (43.8 MPa and 46.0 MPa, respectively). Considering that secondary welding comprises a much larger portion of the total welded area in the column sample than it does in the other two samples, these results seem to indicate that areas of

secondary welding contribute a lot less to the shear strength than the actual spot welds do.

For both the row and the square sample, secondary welding makes up a similar percentage of the total welded area. In these cases, a similar shear strength is observed. Since secondary welding makes up such a large part of the total welded area of the column sample and it is unknown to what extent this contributes to joint strength, it is hard to judge similarity of this joint to the two others from shear strength alone.

In terms of joint stiffness the column and row samples performed very similarly. The square sample shows a lower joint stiffness, or higher flexibility, which could be a result of a thicker resin layer on the outside of the laminate. This is also suggested by the thickness that was measured for this sample: it has a thickness of 1.90 mm, whereas the other samples have a thickness of 1.83 mm and 1.80 mm, respectively. Since the square laminate was manufactured in 2017 whereas both other laminates were made in 2020, it is possible that the square laminate stems from a roll of semipreg material with a higher resin content.

In conclusion, some similarities and differences are observed between the three laminates. Most notably, welds on the square laminate show a smaller welded area than those created on the other two laminates. This phenomenon is attributed to the presence of a thicker resin layer on the outside of the square laminate, an assumption that is corroborated by its observed greater thickness and lower joint stiffness.

Due to the presence of secondary welding in the column sample it is not possible to determine how similar its shear strength is to that of the row and square samples. Since the shear strength of the row and square sample is comparable, the only identified difference between the laminates is the smaller welded area observed for square specimens. When welded area is used as a measure of weld quality, some caution should thus be exercised in comparing results directly between layouts.

2. Are the thickness and warp angle of different samples, cut from the same laminate, consistent? If not, is there a correlation between variations in these properties and observed weld quality?

To answer this question, all four-spot specimens tested in this research were considered. Split by joint layout, the thickness and warp angle were compared between specimens. The obtained values were presented in Table 5.2. In addition, the measured values of top and bottom adherend warp angle have been visualized in Figure 5.4.

Table 6.1 shows the mean and standard deviation values that correspond to this data set. It can immediately be seen that, within the individual laminates, material thickness is consistent. For all three laminates a standard deviation of only ± 0.01 mm is observed.

The warp angle, on the other hand, is clearly a lot less consistent. Upon observing the large differences in warpage across specimens, the question arose if this warpage would affect the welding process and the resulting weld quality.

Table 6.1: Thickness and warp angle of four-spot joint specimens: mean and standard deviation.

Joint layout	Thickness [mm]		Warp angle [$^{\circ}$ /m]	
	Mean	Std Dev	Mean	Std Dev
Column ¹	1.83	0.01	8.14	2.41
Row ²	1.80	0.01	7.41	4.01
Square ³	1.90	0.01	2.97	2.81

¹ Sample size: 5.

² Sample size: 3.

³ Sample size: 6 for thickness, 5 for warp angle.

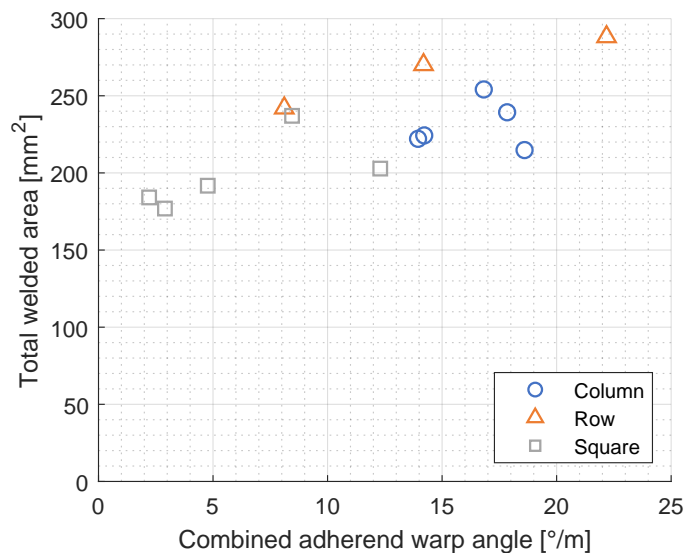


Figure 6.2: Welded area versus warp angle for all four-spot welded specimens.

To assess if a correlation existed between warp angle and weld quality, welded area was used as a measure of quality. Since the specimens in this research were tested under many different conditions (applied load levels, quasi-static vs. fatigue testing, incorrectly tested specimens) welded area was the only available independent measure of weld quality that could be used for all four-spot specimens.

Figure 6.2 shows the total welded area plotted against the combined (top and bottom adherend) warp angle. At first glance, it appears there might be a trend of increasing weld quality with a higher combined warp angle. However, it is important to recall that welds on the square laminate generally had a smaller welded area and that this difference was attributed to a higher resin content. It should also be recalled that the total welded area of the row specimens includes a portion of secondary welding, which results in a higher reported welded area compared to the other layouts. When these two things are taken into account, a clear trend can no longer be perceived.

However, if the warp angle does indeed affect weld quality in some way, it is not sufficient to look at the total welded area of the joints only. Instead, the welded area of individual spots should be considered, as the warp angle might affect weld quality of a spot differently depending on its location within the joint.

Figure 6.3 again shows welded area plotted against combined warp angle, but this time split by joint layout and individual spots within those layouts. Still, no clear trends can be observed that point towards a direct relation between warp angle and weld quality.

In conclusion, considerable differences in warp angle do exist between different samples cut from the same laminate. However, these differences in warp angle were not seen to directly affect observed weld quality. If such a relation does exist, its effect likely falls within the range of variation in weld quality inherent to the welding process itself. This means that, for all intended purposes in this report, different test repetitions of the same layout are assumed similar with regard to weld quality.

6.1.2. Control strategy transferability

To the author's knowledge, this is the first experimental work in which multi-spot welded joints were created with ultrasonic welding on larger adherends and in various layouts. Therefore, it was not yet known how the chosen process control strategy of Zhao et al. [25, 26] would translate to these larger adherends, as their work only considered two-, three- and four-spot column joints on small (25.4 mm width) adherends [26, 28]. It was unknown what the effects would be of using larger adherends and different four-spot joint layouts.

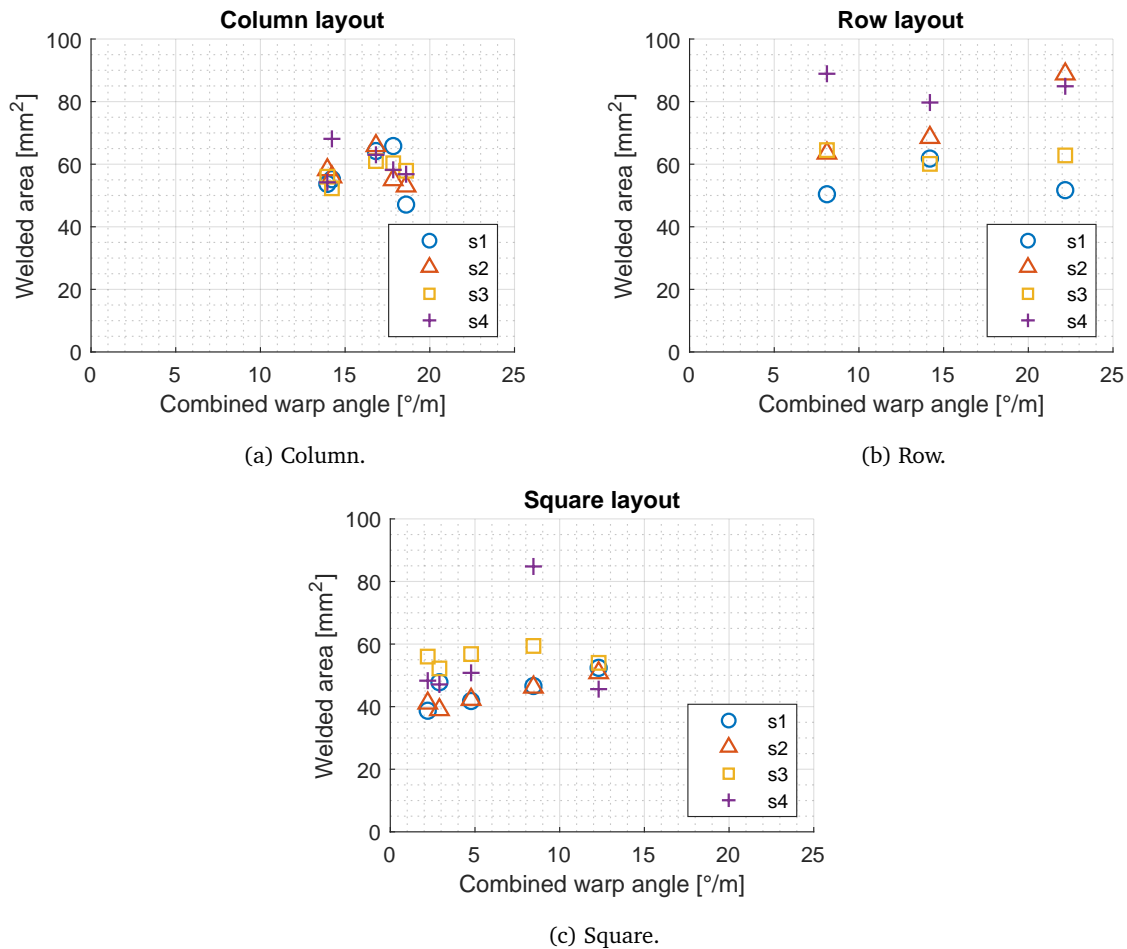


Figure 6.3: Welded area versus warp angle, split by layout and individual spots.

When evaluating the specimens that were welded for this research it was soon discovered that the variations in welded area were larger than the ones found by Zhao et al. and that their values of welded area could not be attained. Whereas Zhao et al. reported an average welded area of 81.8 mm² per spot in a four-spot column joint, the average welded area in this research was found to be approximately 57 mm². This implies that the methodology defined for column joints on small adherends cannot be straightforwardly extended to larger, more complex joint layouts.

Within the framework of this research, the methodology of Zhao et al. was followed in the creation of multi-spot welded joints. Due to limitations in research scope and time constraints, no further attempts were made to optimize this control strategy for the specific joint layouts considered in this research. However, the author believes that additional research on this subject is required in order to better understand the exact mechanisms that affect weld quality in a multi-spot welded joint.

To quickly check if one of the two other process control strategies (dissipated energy or total welding time) might result in a more consistent weld quality, monitored values of these parameters were evaluated against measured welded area for all spot welds previously welded on four-spot specimens. These results are displayed in Figures 6.4 and 6.5.

A lot of scatter is seen in both the welding energy and time when evaluated against welded area: no clear trends are seen that suggest one of these might offer an improved control strategy over displacement-controlled welding. A couple of points are seen to fall outside of the 'cloud' of data points: these correspond to spot welds that were previously identified as outliers (Section 5.1).

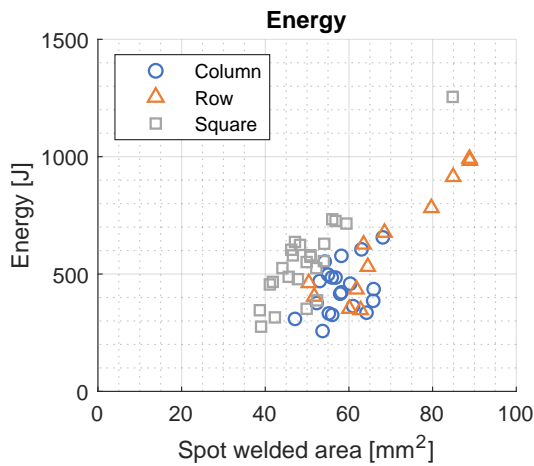


Figure 6.4: Dissipated welding energy versus welded area.

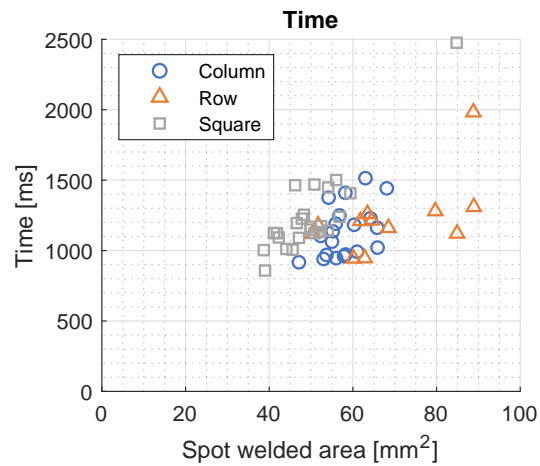


Figure 6.5: Total welding time versus welded area.

6.1.3. Main findings

In terms of weld quality and consistency, a couple of factors have been identified and discussed. Some of these are relevant to the way that fatigue and weld quality results have been interpreted. The main findings of this section are summarized briefly below.

- In general, the welded area of spots on the square specimens is smaller than that of spots on the column and row specimens. Still, a high shear strength was observed. If quality is evaluated based solely on welded area (which, in case of the fatigue specimens, is the main available independent measure of weld quality as all of them are tested under different conditions and fatigue test results are naturally subject to a high variability), the welds on square specimens appear to be of lower quality than those of the other two joint layouts. However, since the results indicate that a similar shear strength can be attained on all three laminates, it is considered valid to assume a comparable weld quality across the different layouts. In line with this assumption, stress values derived from applied load and welded area can be compared directly between layouts.
- Despite there being significant differences in warp angle across specimens, material warpage was not seen to directly affect weld quality. If there is a correlation, its effect falls within the range of variation in weld quality inherent to the welding process itself. This means that, for all intended purposes in this report, different test repetitions of the same joint layout are assumed to be similar with regard to weld quality.
- It has been found that the control strategy of Zhao et al. [25, 26] for welding multi-spot joints cannot be straightforwardly transferred to large four-spot joints. For the spots welded in this research, a lower average welded area with higher variability is observed. The monitored welding energy and time do not suggest that either energy- or time-controlled welding in which an optimum value is determined only once would be a better control strategy.

6.2. Initial damage in column joints

In Figure 5.5, the quasi-static load-displacement curves of the three four-spot specimens tested for ultimate failure load were presented. From this graph it can be seen that the load-displacement curves of the row and square specimen both progress linearly up to a point where joint stiffness starts to decrease, which is then rapidly followed by final failure. Similar joint behavior, in which no obvious changes in stiffness are observed until final failure, was consistently seen by Zhao et al. in double-lap shear and pull-through tests of single spot welds [27, 42]. For the column specimen, however, the observed stiffness behavior is a little different.

The quasi-static load-displacement curve of the column joint is again shown in Figure 6.6. Looking at this image it can be seen that the graph starts off with a linear slope (indicated by the orange trend-line), similar to what was seen for the row and square specimens. At a load level of approximately 43% the joint stiffness starts to gradually decrease. However, rather than decreasing continuously up to final failure, it can be seen that the slope of the graph increases again and that a second linear region (yellow trend-line) is observed.

It is assumed that the initial decrease in stiffness stems from failure of a single spot weld. This would be one of the outer spots of the joint: in a column joint, these outer spots transfer a larger portion of the applied load than the inner ones. It is hypothesized that, after failure of this spot, the applied load was redistributed over the three remaining spots in a more efficient way. As a result, a certain recovery in stiffness is observed, although the original joint stiffness is not reached again.

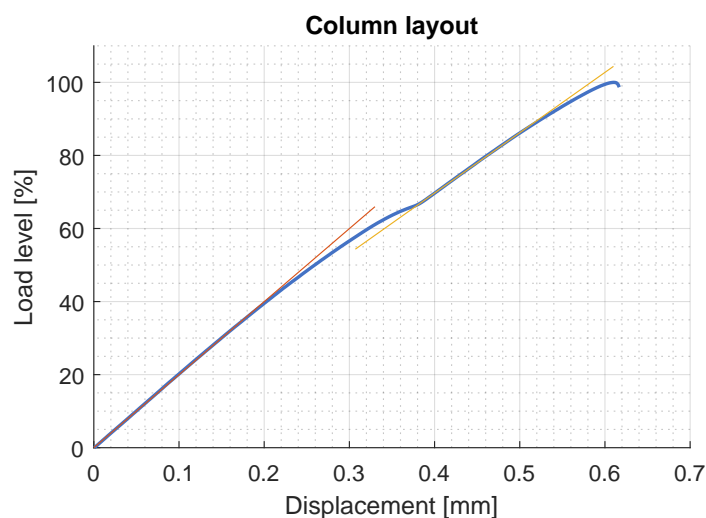


Figure 6.6: Quasi-static load-displacement graph of the column specimen.

The gradual decrease in stiffness between the two linear regions is observed approximately from 43% up to 67% of the ultimate failure load. Since fatigue tests were planned to be executed at a load level of 70%, the question arose if this behavior would consistently be seen in column joints and if, as a result, substantial initial damage would already be present in these joints after the initial load ramp-up.

To investigate this, a column specimen was subjected to a gradually increasing load in the fatigue test setup, up to a load level of 70%. During this ramp-up, DIC photos were taken at regular intervals. Since the hypothesis of existing damage in column joints was based on observations from a single specimen, this test would help determine if the observed behavior could be considered representative of the column layout or if it was more likely to be an anomaly.

Figure 6.7 shows out-of-plane displacement at the four spot locations with an increasing applied load. It can be seen that, over the entire evaluated load range, the shape of the four graphs is very similar. The main difference between the graphs is how they appear rotated compared to each other. This is in line with expectations, as secondary bending affects out-of-plane displacement differently depending on the exact location of each spot. From the similarity between the curves, it appears that all four spots still have a load-carrying capability at a load level of 70%.

The out-of-plane displacement is also evaluated over a longitudinal center-line passing through the four spots. The resulting graph is shown in Figure 6.8. Same as when individual spot locations were considered, displacement is evaluated with respect to an unloaded state. The direction of increasing load is depicted in the image: the red curve corresponds to the final load level of 70%.

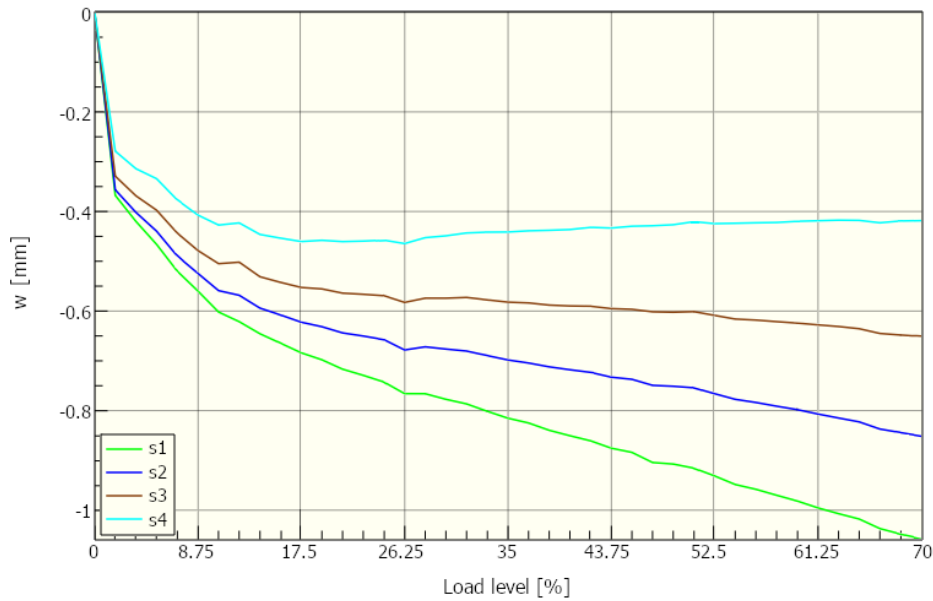


Figure 6.7: Out-of-plane displacement with increasing load at spot locations in the column layout.

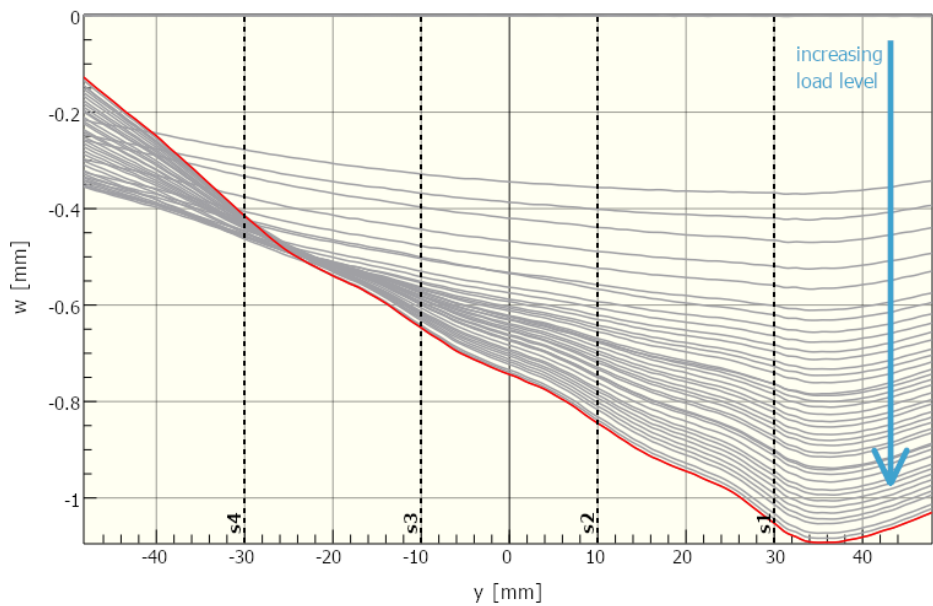


Figure 6.8: Out-of-plane displacement with increasing load over longitudinal center-line in the column layout.

Looking at the evolution of the displacement curve with increasing load level it can be seen that, after some initial settling, the specimen rotates around a stationary point between s4 and s3 as a result of secondary bending. Apart from this rotation, the shape of the curve remains mostly unaffected between the two outer spots (s1 and s4). This reinforces the assumption that, at least up to a load level of 70%, all spots still have a load-carrying capability: out-of-plane displacement of a segment in between two spots will be restricted so long as both spots are still attached.

Just above s1, at approximately $y = 35$ mm, it can be seen that a little ‘bump’ starts to form in the curve with increasing load level. This means that, at this location, a larger change in out-of-plane displacement is observed compared to the surrounding material. Considering that this location corresponds to the outer edge of s1, it is assumed that formation of this ‘bump’ indicates the evolution of damage, starting from the edge of the spot weld.

To briefly recap the information presented in this section: the multi-stage joint stiffness behavior observed during quasi-static testing fueled the question if significant damage would already exist in column joints when testing at a load level of 70%. For the specimen that originally sparked this question, a second linear stiffness stage was observed around 67% and it was hypothesized that one spot had failed at this point. In the subsequently tested joint load it was found that all spots still had a load-carrying capability at a load level of 70%. However, an increased out-of-plane displacement at the outer edge of the uppermost spot did suggest the existence of damage at this location.

Since the applied load level was defined based on the quasi-static test specimen, the exact resulting shear stress will vary from specimen to specimen. However, it seems that a substantial amount of damage will already be present in the joints at a load level of 70%. This might even go as far as one spot having failed completely prior to testing. The cyclic displacement data and DIC results seem to indicate that this happened in specimen C_FL1: this will be discussed further in Section 6.3.3. Regardless, the fact that damage will likely already exist in the column joint prior to testing and the implications this will have for further fatigue results must be acknowledged.

6.3. Fatigue behavior of four-spot welded joints

With two important subjects regarding the interpretation of the fatigue results addressed, the remainder of this chapter focuses on those results. Three aspects of fatigue behavior are addressed subsequently: fatigue life, failure modes and damage evolution. Finally, fatigue behavior of the joints is compared to that of joints with the same layouts that were welded on steel adherends.

6.3.1. Fatigue life

Fatigue lives of all considered specimens were previously reported in the form of a stress-life diagram (Figure 5.6). Due to the presence of secondary welding in all row specimens, two edge cases were presented: either full or zero contribution of secondary welding to joint strength. For the purpose of this discussion, the most conservative scenario of full contribution is assumed.

This graph is again shown in Figure 6.9. This time, a log-linear regression line has been fitted to the three column specimens and extrapolated. Considering the fact that substantial damage was likely already present in the column specimens prior to cyclic loading, as discussed in Section 6.2, it is expected that all three specimens experienced preferential loading of a single spot and, subsequently, comparable damage evolution through the joint.

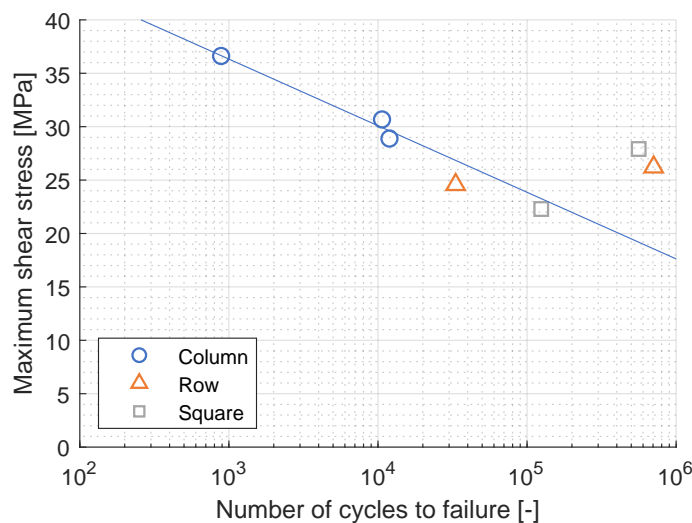


Figure 6.9: Fatigue life diagram with linear regression line for the column specimens. In the case depicted here, it is assumed that the secondary welded area in the row specimens fully contributes to joint strength.

Two row and two square specimens are also depicted in this graph. For both joint layouts, it can be seen that one specimen failed at both a lower shear stress and a lower number of cycles compared to the other specimen of that layout. It is expected that, similar to what was seen in the column joints, this poorer performance is a result of preferential loading of a single spot in those specimens. This is addressed in more detail in Section 6.3.3.

Looking at those row and square specimens that are expected to have failed after failure of a single spot, it can be seen that they both lie very close to the regression line that was fitted to the column specimens. This becomes even more pronounced when recalling that the most conservative estimate of row joint performance is shown: in reality, its maximum shear stress is higher than what is depicted here. This seems to suggest that, if existing damage results in preferential damage evolution through a single spot under cyclic loading, the layout of a four-spot joint no longer affects its performance in terms of fatigue life.

This observation can be explained by the fact that, for both a row and square layout, fracture of any spot will result in an asymmetric joint layout. This asymmetry of the remaining joint layout means that the applied load can no longer be distributed evenly over the remaining three spots. This will result in a stress concentration at one of the remaining spots, depending on which one initially failed, which will then again promote crack initiation and propagation in that one spot only. As a result crack growth will always be resisted by only one spot at a time, similar to what was observed in the column layout.

When looking at the row and square specimen that reached a fatigue life of over half a million cycles, it can be seen that both specimens fall far above the column regression line. For these specimens, it is assumed that no initial damage was present and as a result, all four spots were loaded equally. Based on these results and the fact that, in a four-spot column joint, the applied load can never be distributed across all spots equally, it can be said that the row and square joint layouts are capable of reaching higher fatigue lives than a column layout. However, this superior performance is no longer observed when damage is already present in either of these joint layouts.

With regard to the comparison between row and square performance in terms of fatigue life, the available data set is too small, and the amount of scatter inherent to fatigue testing too high, to draw any conclusions. Additional research is required to test the hypothesis that a square layout will reach a slightly higher fatigue life than a row layout, in which boundary conditions are not identical for all four spots.

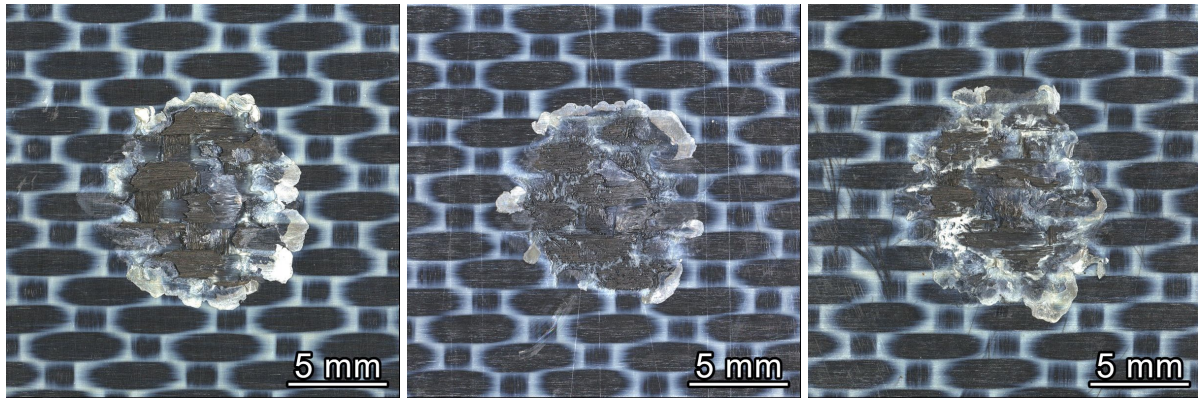
6.3.2. Failure modes

In previous research by Zhao et al. [25–28] featuring ultrasonic welds on CF/PPS adherends with a $(0/90)_{3s}$ layup (the same material as used in this research), first ply failure was consistently reported as the failure mode of the welded spots. It was expected that this same failure mode would be observed for all joints in this research.

Indeed, first ply failure was observed for all spot welds. The observed damage remained restricted to the polymer and outermost ply of the adherends at the weld interface, with damage not extending beyond the quasi-circular area of the welds.

Figure 6.10 shows the fracture surfaces of spots tested under three different conditions: (a) quasi-static testing with a continuously increasing load up to failure, (b) quasi-static testing with an increasing load up to failure while pausing at regular intervals for DIC photos, and (c) cyclic loading at a load level of 70% while pausing at regular intervals for DIC photos. All images are of the spot s1 in the column layout, taken from three different specimens.

Looking first at Figure 6.10a, multiple features that indicate a high-quality weld can be observed. This fracture surface shows bare fiber bundles laying exposed in the welded area, as well as areas of resin with clear fiber imprints. Both types of features can be seen more clearly in the surface roughness image in Figure 6.11.



(a) Quasi-static testing with a continuously increasing load.

(b) Quasi-static testing with pauses at regular intervals.

(c) Cyclic testing at a load level of 70% with pauses at regular intervals.

Figure 6.10: Fracture surfaces encountered in s1 of column joints tested under various conditions.

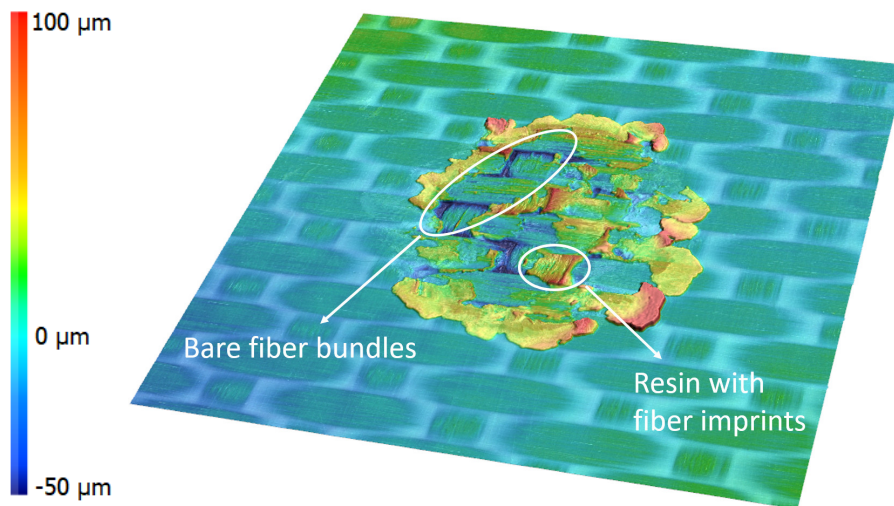


Figure 6.11: Surface roughness image of a spot that underwent quasi-static testing, during which the load was increased up to failure without interruptions. Bare fiber bundles and fiber imprints can be observed, both indications of a high-quality weld.

When looking at Figure 6.10b, the effect of pausing the test at regular intervals becomes apparent. Same as the spot shown in Figure 6.10a, this spot was not subjected to cyclic loading but instead to a strictly increasing tensile load. This time, it can be seen that the regular pausing of the tests resulted in vertical ‘ridges’, resembling beachmarks, in the polymer on the fracture surface. On the surface roughness image corresponding to this spot (Figure 6.12) this manifests itself mostly as the polymer inside the welded area having an increased roughness. In Figure 6.10b, however, the orientation of these markings transverse to the loading direction can be seen more clearly.

Finally, Figure 6.10c corresponds to a spot weld subjected to cyclic loading where DIC photos were taken at regular intervals. What stands out most in this fracture surface is the milky-white texture of the polymer at the bottom-left of this spot. This is attributed to polymer crazing, which in itself is acknowledged as a characteristic of Mode I crack opening [43, 44]. A surface roughness image of this weld is shown in Figure 6.13, in which this assumed crazing can be seen more clearly.

The fact that distinguishing features could be identified on these fracture surfaces helped greatly in identifying the assumed path of damage evolution through each of the joints. For example, in the

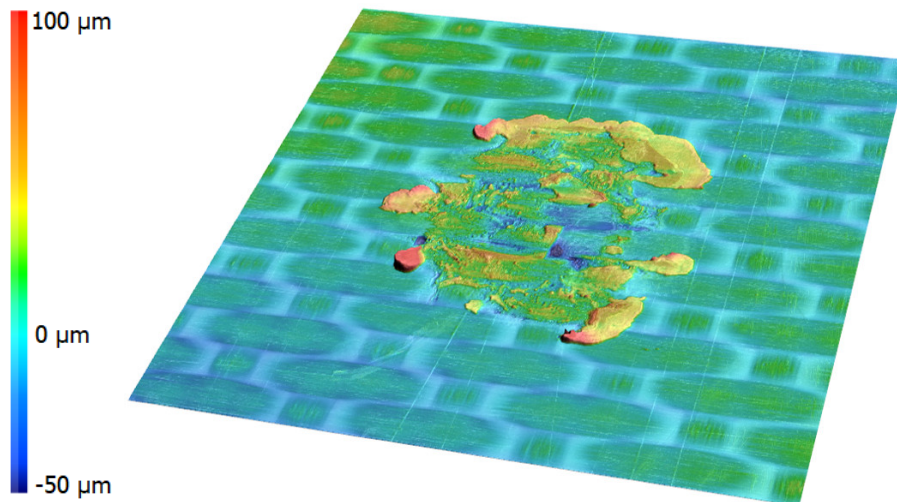


Figure 6.12: Surface roughness image of a spot that underwent quasi-static testing with regular pausing for DIC photos. On its fracture surface vertical ridges resembling beachmarks were observed: in this image, they predominantly manifest as the polymer having an increased roughness.

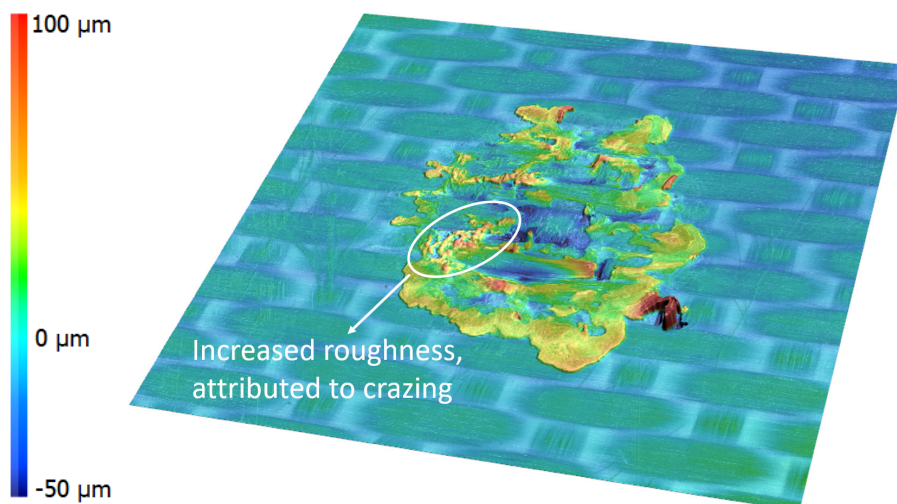


Figure 6.13: Surface roughness image of a spot that underwent cyclic testing with regular pausing for DIC photos. On its fracture surface a region with a milky-white texture and increased roughness was observed: this was attributed to crazing as a result of Mode I crack opening.

samples that reached a high fatigue life beachmarks could be observed on the spots. These marks were attributed to pausing the test at regular intervals for DIC photos, indicating the slow progression of damage through the joint. In spots that were assumed to have failed as a result of preferential crack growth, polymer crazing was frequently observed. In the spots that were assumed to have failed quickly after initial failure of a single spot, fracture surfaces closely resembled that which was found for quasi-static failure with no test interruptions.

6.3.3. Damage evolution

Up to this point, the fatigue life and failure mode aspects of joint fatigue behavior have been discussed. When evaluated individually, neither of these aspects offers much insight into the trajectory of damage evolution through the joints.

In the previous section it was discussed how various distinct features could be identified on the fracture surfaces of spots tested under different conditions. Upon combining this knowledge with cyclic peak displacement curves and DIC measurements, evaluated predominantly towards the end of each specimen's fatigue life, the path of damage evolution through all joints could be identified with a fair degree of confidence.

In this section the three joint layouts (column, row and square) will be addressed subsequently. For each layout it will be discussed how damage was found to evolve through this joint type, if this behavior can be considered representative for this layout, what the implications of these findings are and how this links back to the original hypotheses from Section 3.3.

Overview images of the fracture surfaces have been included in this section to support the discussion: for high resolution images of individual spot welds, please refer to Appendix A.

Column layout

The cyclic peak displacement curves of the column specimens are displayed in Figure 6.14, evaluated only over the final 2,000 cycles of each respective specimen's lifetime. Note that for C_FL1, a total fatigue life of only 887 cycles was observed.

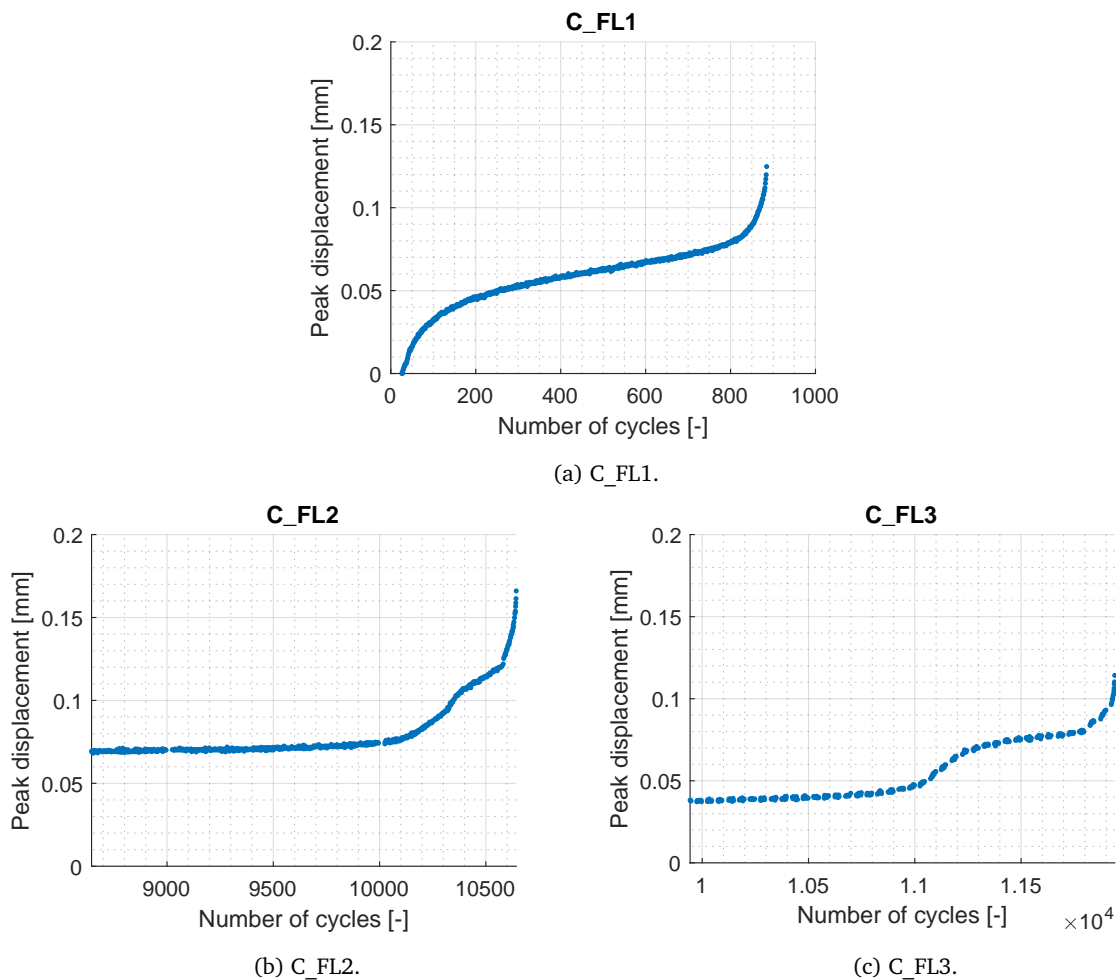


Figure 6.14: Peak displacement during the final 2,000 cycles of column specimen lifetime. Note that the total lifetime of C_FL1 is only 887 cycles.

The first point of attention here is the similarity in shape between the curves of C_FL2 and C_FL3. In both cases, it can be seen that displacement starts to rapidly increase at some point between 500 to 1,000 cycles before final failure. After this initial increase, however, the rate of displacement increase lowers again. This resembles the recovery behavior in joint stiffness that was previously identified and addressed in Section 6.2. In all three specimens, a rapid increase in displacement towards final failure is observed in the last 100 to 200 cycles.

When looking at the DIC line graph for C_FL2 (Figure 5.17), it can be seen that the unloaded out-of-plane displacement increased predominantly between s1 and s2. The final measurement, indicated by the red line, was taken at 10,000 cycles. Looking at Figure 6.14b, it can be seen that this was right before the first rapid increase in peak displacement. Since a small kink in the DIC line graph can still be seen at the location of s1 during this final measurement, it is assumed that this measurement was taken right before complete fracture of s1. From the fracture surfaces (Figure 6.15b), crazing was identified on s1 and on the side of s2 that lies adjacent to s1, whereas the fracture surfaces of s3 and s4 resembled a quasi-static fracture.

In the DIC line graph of C_FL3 (Figure 5.18), the final measurement corresponds to a much later stage in damage evolution. As seen in Figure 6.14c, at 11,900 cycles this measurement falls in the second stage of rapidly increasing displacement. In the DIC line graph it can be seen that the location of peak out-of-plane displacement has shifted to the center of s2, whereas the shape of the curve is now completely smooth at the location of s1. This seems to indicate that, during this final measurement, s1 had already failed and damage had progressed significantly through s2. Both spots s3 and s4 appeared to still be completely intact. Similar to C_FL2, crazing was observed from the fracture surfaces (Figure 6.15c) on s1 and the adjacent side of s2, whereas s3 and s4 seemed to indicate quasi-static failure.

Since C_FL1 was tested at a load level of 75% and recalling the discussion from Section 6.2, it is expected that a single spot in this specimen had already completely failed before cyclic loading.

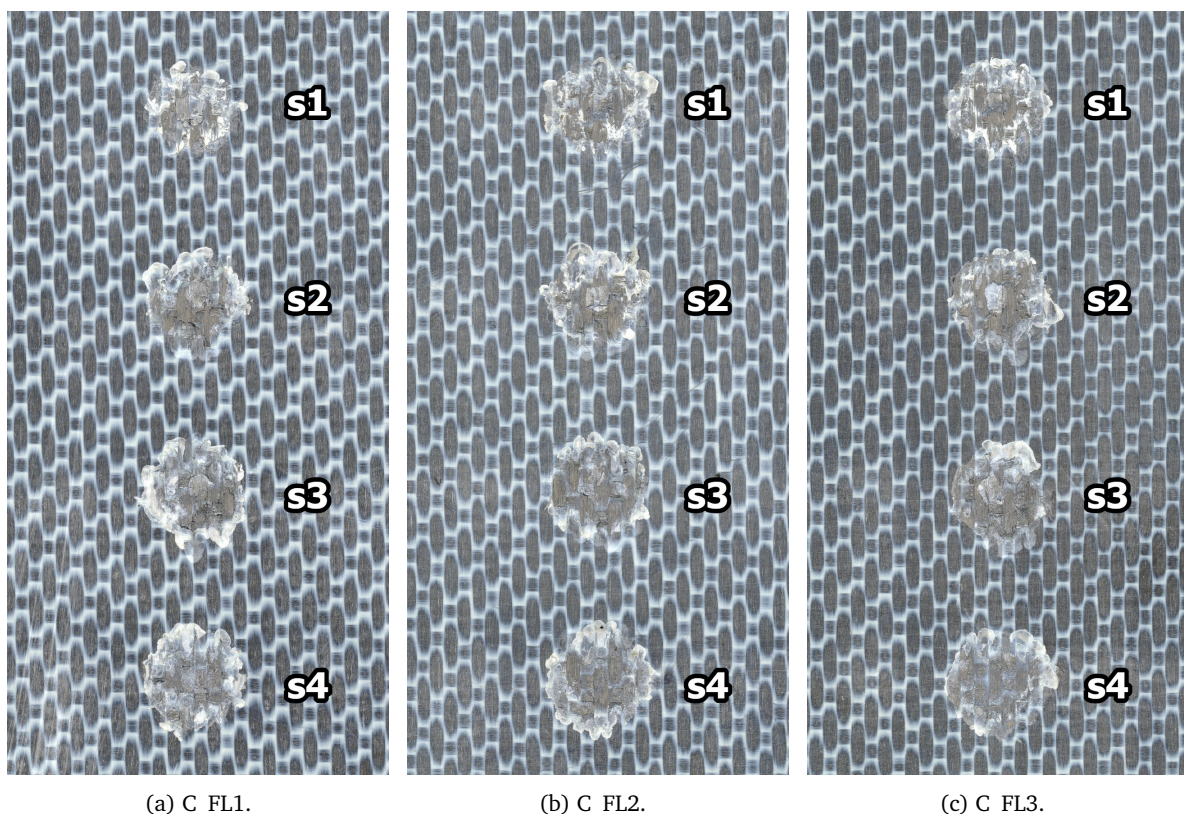


Figure 6.15: Overview images of the fracture surfaces of the column specimens. Vertical direction is the direction of applied load. For high resolution images of individual spot welds, please refer to Appendix A.

This is corroborated by the shape of its cyclic peak displacement curve, which does not show the recovery behavior observed in the other two specimens. The fracture surfaces (Figure 6.15a) also show crazing on s1, suggesting this spot experienced mode I crack opening and was thus likely the first spot to fail.

In all three column specimens, it appeared that damage originated from s1. Whether this is a direct result of the original welding sequence or of different clamping boundary conditions in the test setup is unknown. In C_FL1 this spot is visibly smaller than the other three spots, suggesting this might be the reason for preferential damage initiation and evolution through this spot. However, in the other two specimens this is not the case. In fact, in both specimens C_FL2 and C_FL3 s4 has a smaller welded area than s1. These test results do seem to indicate that, contrary to what was hypothesized in Section 3.3, damage in a column joint tends to initiate and evolve in a single spot rather than from both overlap edges simultaneously. This preferential damage evolution through a single spot results in a low total fatigue life but, at the same time, the identifiable failure of a single spot does provide a warning that complete failure of the joint is imminent in around 500 to 1,000 cycles.

Row layout

The final 2,000 cycles in the lives of the row specimens are shown in Figure 6.16. As was already identified in Section 6.3.1, R_FL2 failed at both a lower maximum stress and a lower number of cycles than R_FL1 did. This observation led to the assumption that initial damage was already present in R_FL2, leading to preferential crack growth through a single spot and therefore faster overall damage evolution through the joint. This theory is supported by the peak displacement curves: little variation is observed for R_FL1 right up to final failure, whereas multiple changes in slope are seen for R_FL2. This indicates that the four spots in R_FL2 likely did not fail simultaneously.

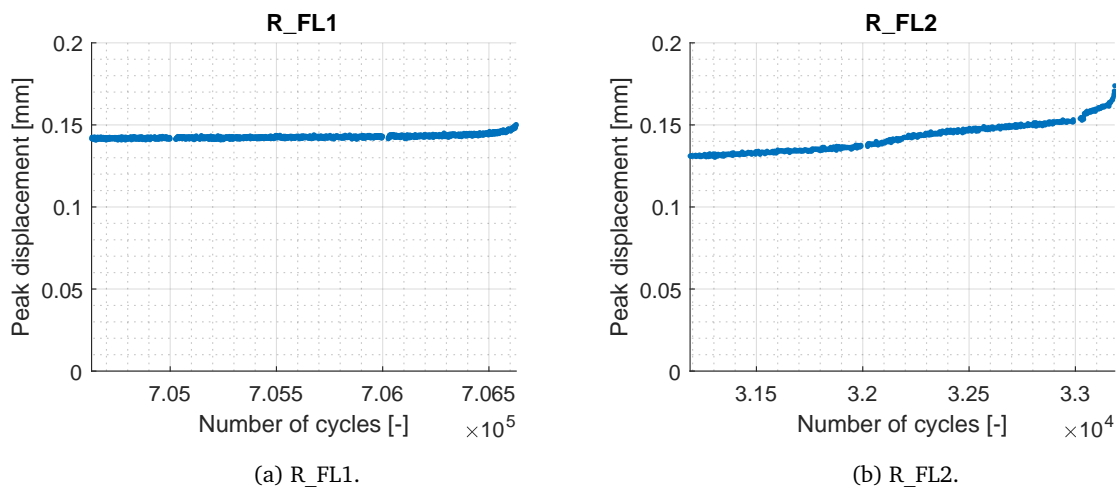


Figure 6.16: Peak displacement during the final 2,000 cycles of row specimen lifetime.

Looking at the DIC line graph of specimen R_FL1 (Figure 5.19) it can be seen that, apart from the observed rotation, the segments in between spots remain completely straight up to the final measurement. This reinforces the assumption that all four spots in this specimen retained a load-carrying capability right up to the moment of failure. In addition, beachmarks were observed on the fracture surfaces of all four spots (Figure 6.17a).

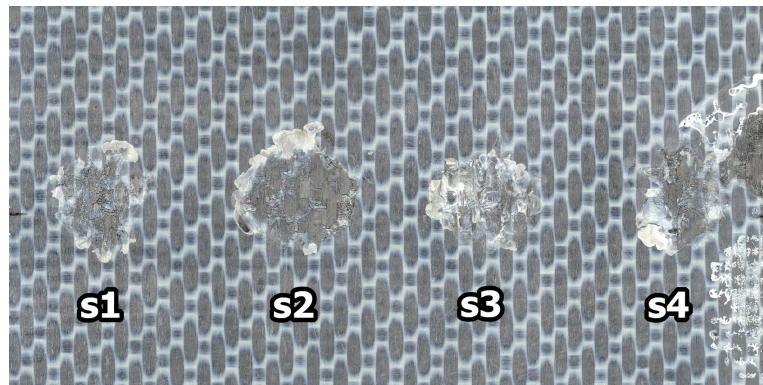
When considering R_FL2 on the other hand, the final measurement in the DIC line graph (Figure 5.20) seems to indicate failure of s3 at this point. Looking at Figure 6.16b it can be seen that this final measurement was taken at 33,000 cycles, where a sudden kink in the displacement curve is observed. Another slight change in slope can be seen at the location of the previous DIC measurement (32,000 cycles): it is assumed that this is where s4 failed. Since a cracking sound was heard at the start of this test, it is expected that the secondary welded area at the edge next to s4 had already

failed when cyclic loading was first applied. Its sudden fracture, combined with the lower quality of s4 due to the occurrence of secondary welding in the first place, likely led to preferred damage evolution at this location.

Assuming a more tailored process control strategy in which high-quality welds can be created without secondary welding, R_FL1 is definitely the case that is more representative of expected row layout fatigue behavior. The results discussed in this section show that a row layout is capable of reaching a high fatigue life due to equal load distribution across all its four spots. However, final failure will be sudden without any prior indication. An indication of imminent failure can be observed when the joint fails as a result of preferential loading of a single spot. This does, however, severely decrease the total fatigue life of the joint. These findings are in line with what was hypothesized in Section 3.3.



(a) R_FL1.



(b) R_FL2.

Figure 6.17: Overview images of the fracture surfaces of the row specimens. Vertical direction is the direction of applied load. For high resolution images of individual spot welds, please refer to Appendix A.

Square layout

Figure 6.18 shows the cyclic peak displacement curves of the two square specimens. Contrary to the graphs used earlier in this section to evaluate column and row damage evolution, these graphs are evaluated over the final 5,000 cycles of specimen lifetime. This way, a slight change in slope is captured that occurred in S_FL2 between 122,000 and 123,000 cycles.

From Section 6.3.1, it is known that S_FL2 failed at a lower maximum stress and lower number of cycles than S_FL1 did. It was therefore expected that preferential damage evolution had taken place in S_FL2. On the other hand, in S_FL1 it was assumed that all four spots had been loaded equally. This hypothesis is supported by the data shown in Figure 6.18a: no apparent change in slope is observed right up to final failure.

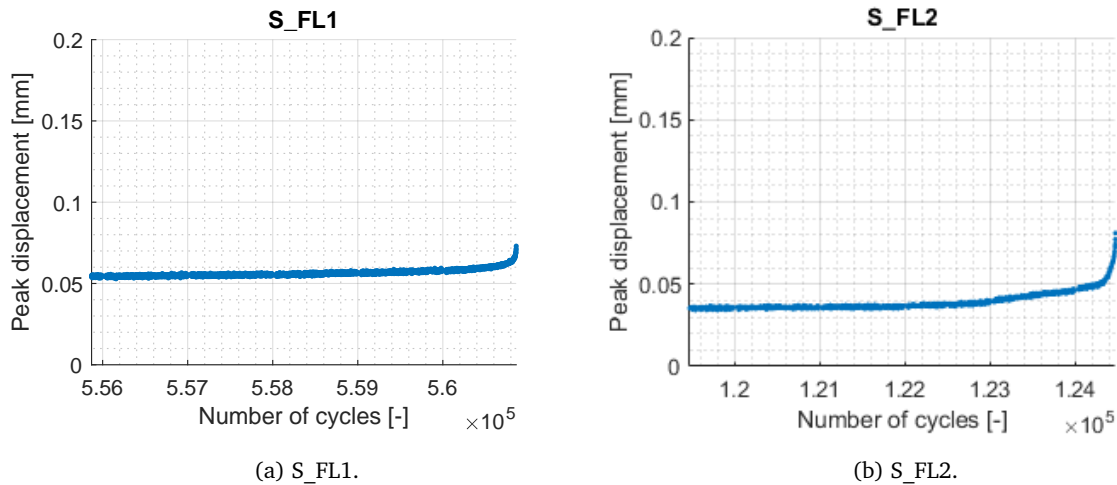


Figure 6.18: Peak displacement during the final 5,000 cycles of square specimen lifetime.

When looking at the DIC graphs corresponding to S_FL1, and Figure 5.21 in particular, it is seen that during the final measurement (560,000 cycles) a notable change in shape with respect to the large scatter band of previous data had occurred. Combined with Figure 5.23, in which a rotation can be observed with respect to previous measurements, it is assumed that s2 ultimately failed first. However, up to this point all four spots are expected to have been loaded equally. It is expected that, when this spot did fail, its fracture was directly followed by complete joint failure as the total load-carrying area of the joint had already decreased significantly under cyclic loading. This is corroborated by what is seen on the fracture surfaces (Figure 6.19a): beachmarks can be seen on all four spots, and the spots are all similar in size with s4 being the smallest of the four by a small margin.

For S_FL2, DIC measurements were taken in a loaded state. The out-of-plane displacement displayed in these graphs was evaluated with respect to the very first measurement, which was also in a loaded state. Looking at Figures 5.27 and 5.28, it can be seen that during the final measurement (124,000 cycles) a rotation had occurred in which a notable change in out-of-plane displacement is

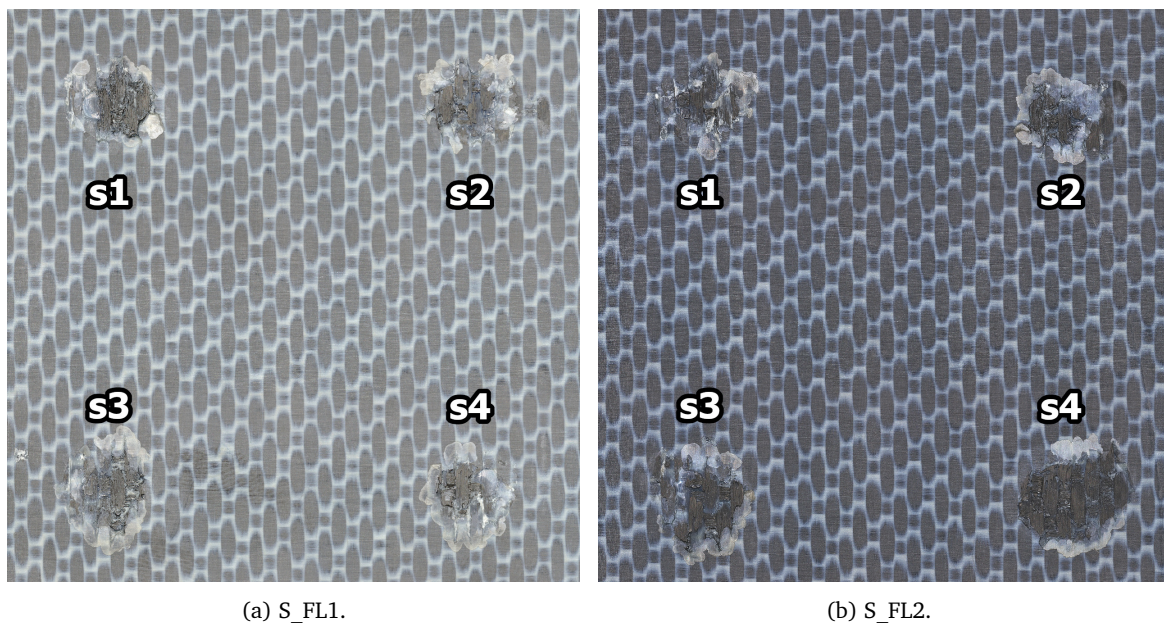


Figure 6.19: Overview images of the fracture surfaces of the square specimens. Vertical direction is the direction of applied load. For high resolution images of individual spot welds, please refer to Appendix A.

seen on the side of s1 and s3. This change is most pronounced for s3: it is assumed that this spot failed between 122,000 and 123,000 cycles, where the slope of the peak displacement curve first changed. It is expected that damage subsequently evolved predominantly through s1, ultimately resulting in fracture of this spot and immediate subsequent failure of the complete joint. Looking at the fracture surfaces it can be seen that s4 is significantly bigger than the other three spots and has a fracture surface that is indicative of quasi-static failure. s1 shows clear indications of what is expected to be crazing; for s2 and s3, no clear markings can be observed on the fracture surfaces that support the theory of damage evolution through this joint.

A similar conclusion can be drawn as was done for the row layout. Assuming a welding control strategy that results in high-quality welds of consistent size and shape, the behavior of S_FL1 is considered more representative of square layout fatigue behavior. A high fatigue life can be reached if all spots are equally loaded, but again, final failure will come sudden and without any prior indicator. It is interesting to see that, in S_FL2, the supposed failure of a single spot resulted only in a slight change in stiffness and the joint retained its load-carrying capability for almost 2,000 more cycles. This is a longer period of time than what was seen for the column and row layouts.

6.3.4. Comparison to steel joints

Figure 6.20 shows the stress-life curves obtained for four-spot welded joints on steel (Figure 6.20a) [33] and TPC (Figure 6.20b) adherends side by side. For the sake of this discussion, the TPC row and square specimens in which initial damage is assumed to have led to preferential damage evolution through a single spot have been omitted.

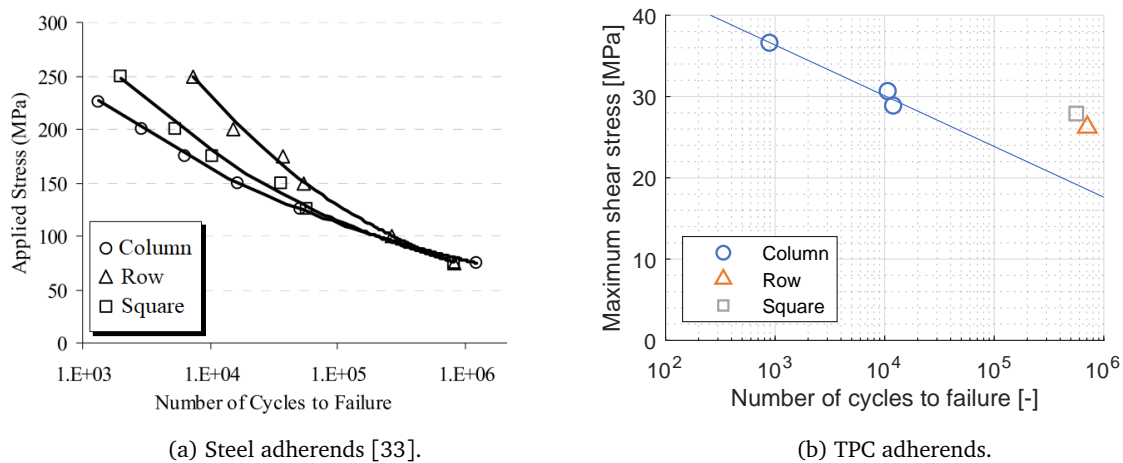


Figure 6.20: Side-by-side stress-life diagrams for steel and TPC adherends. For the TPC adherends, specimens in which preferential damage evolution through a single spot is assumed to have occurred have been omitted.

In both steel and TPC joints, the column layout shows the lowest performance out of the three layout types. This result is in line with expectations, as in a four-spot column joint layout the applied load cannot be distributed evenly across all four spots. In general, adding spots beyond three in a column joint layout has been known to offer little improvement in terms of load-carrying capability.

An interesting observation lies in the fact that, in steel joints, the improvement in performance of a row layout over a square layout is much more significant than what is seen in TPCs. In TPCs, the results found for a row and square specimen in which all four spots could be equally loaded lie close together. Moreover, both the square and row specimen show a larger improvement in fatigue life over the column layout here than what is seen in steel joints.

It can be seen that, towards a higher number of cycles, the stress-life results found in steel adherends for the different layouts start to converge. This is a result of a change in failure mode: whereas

the steel joints at lower fatigue lives consistently showed spot fracture, in the high-cycle regime all specimens failed as a result of sheet fracture. Since TPC joints are expected to always fail from spot fracture due to the presence of reinforcing fibers in the adherends, it is assumed that the observed interrelation between layout type performances in TPCs will remain the same over the entire applied stress range.

Multiple differences between behavior in steel and TPC adherends indicate that existing knowledge on fatigue behavior in steel joints cannot be readily transferred to TPCs. Most notably, the interrelation between performance of the three joint layouts is not the same.

In metals, welding of a spot typically results in residual stresses and a heat-affected zone of a certain size surrounding that weld. Considering the superior fatigue life that was observed for the row layout and the fact that the spots in this layout lie closer together than they do in a square layout, it is assumed that the welds in this layout fall within the heat-affected zone of the adjacent spots and that welding was done in such a way that adjacent spots were actually strengthened in this process. This type of interference between spot welds has not been observed in TPCs and, as a result, the superior performance of the row layout is not expected to be seen in TPC joints.

Conclusions and Recommendations

7.1. Conclusions

Prior to evaluating the experimental fatigue results, weld quality and consistency were discussed. From this analysis it became apparent that welded area does not always provide an accurate measure of weld quality. Spots with a smaller welded area were seen to still achieve high shear strength values, indicative of a high-quality welded bond. A clear distinction should be made between weld *quality* on one hand (meaning, how well polymer chains have diffused across the interface) and weld *performance* on the other hand (this takes into account the actual load that can be carried by the joint: here, a larger welded area is obviously better).

It was discovered that an existing welding control strategy for four-spot column joints on small adherends [25, 26] could not be readily transferred to welding on larger adherends in various four-spot layouts. It was seen that the average resulting welded area was smaller and showed a larger variability. Additional research is needed to define a more effective and consistent process control strategy for multi-spot welding with various spot arrangements.

Conclusions regarding the fatigue behavior of the four-spot welded joints have been structured according to the original research questions. Recall that the main research question was formulated as follows: *What are the effects of spot arrangement on fatigue behavior in a four-spot welded TPC joint?*

a. In what way is the fatigue life affected?

First of all, it was concluded that a row and square layout are both capable of reaching a considerably higher fatigue life than a column layout. However, if existing damage results in preferential damage evolution through a single spot, the layout of the joint does no longer seem to have an effect on joint performance in terms of fatigue life. From the limited data set available in this research, it was not possible to determine if either the row or square layout would consistently show superior performance over the other in terms of fatigue life.

b. What failure modes are observed?

For all four-spot joints tested in this research, first ply failure was observed as the failure mode. This is in line with expectations and was consistently observed in quasi-static testing by Zhao et al. [25–28] as well. For all welds, observed damage remained restricted to the originally welded area: no damage was seen to extend beyond the spots.

c. How does damage evolve through the joint?

In the column layout it was found that, at the evaluated load level of 70%, substantial damage was already present in the joint prior to cyclic loading. In all column specimens, this damage was found to evolve through a single (outer) spot. Failure typically occurred in two steps: first, fracture of the single spot that had experienced preferential damage evolution. After this single spot failure, the applied load was redistributed over the remaining three spots and the joint retained its load-carrying capability for about 500 to 1,000 more cycles before final failure.

For the row and square layout, the results that were found were very comparable to each other. In both cases, one specimen was tested in which damage appeared to have evolved through all four spots simultaneously. For both layout types, one specimen was also tested in which it seemed that

preferential damage evolution through a single spot had occurred. It was concluded that, in case of damage evolution through all spots simultaneously, both layout types were capable of reaching a high fatigue life, substantially higher than the column layout. However, for these specimens final failure occurred sudden and without any previous indication.

For the row and square specimen that experienced preferential damage evolution through a single spot, the observed fatigue life was considerably lower. However, the fracture of a single spot and subsequent change in joint stiffness did provide an indication that complete joint failure was imminent. For the row specimen this single spot fracture was seen approximately 1,000 cycles before final failure, whereas in the square specimen it was seen approximately 2,000 cycles before joint failure and resulted only in a small change in joint stiffness.

Based on these conclusions, it appears that there is indeed potential for damage tolerant design in multi-spot welded joints. However, when tested at a load level of 70% the remaining lifetime of a joint after fracture of a single spot is understandably low, since the joint now only retains 75% of its initial load-carrying welded area. As a result, no fracture of individual spots was seen after fracture of the first spot, since final failure of the complete joint had already occurred at this point. To be able to better evaluate the damage-arresting potential of multi-spot welded joints, it would be interesting to repeat this research at a lower load level (for example, 30%), artificially introduce damage in a single spot and monitor the trajectory of damage evolution as it progresses from spot to spot.

The second research question related to the comparison of fatigue behavior in steel and TPC adherends and was formulated as follows: *To what extent can existing knowledge about the effects of spot arrangement on fatigue behavior in steel joints be transferred to four-spot welded joints in TPCs?*

- a. How do the effects of spot arrangement on fatigue life compare between steel and TPCs?

It was seen that the interrelation between performance of the three layouts is not the same in steel and TPC adherends. In both materials a column layout results in the lowest fatigue life. For steel joints, a square layout offers some improvement whereas a row layout is seen to reach much higher fatigue lives consistently. This superior performance of the row layout might be a result of material strengthening due to interference between spot welds and the heat-affected zone of adjacent spots.

In TPC joints, it seems that both a row and square layout offer a distinct improvement in fatigue life over a column layout. Between those two layouts, however, there does not immediately seem to be a clear distinction. These results indicate that established design rules for multi-spot welded joints in steel cannot be readily transferred to multi-spot welded joints in TPCs.

- b. What similarities and differences are observed in failure modes across load levels?

In steel joints, failure modes varied with different load levels. At high load levels (low-cycle regime) the predominant failure mode was nugget fracture, which resembles the typical failure mode in TPC welded joints. Towards the high-cycle end of the spectrum this failure mode changed to sheet fracture of the steel adherends. At intermediate load levels, various failure modes were observed.

In TPCs, the only failure mode that was observed across the entire spectrum of specimens tested in this research was first ply failure, meaning that fracture always occurred through the spots at the weld interface. In reference work by Zhao et al. [25–28] considering ultrasonic spot welding of the same material combination, this failure mode was also reported consistently.

For steel joints, it was seen that fatigue life results of the three layout types converged towards the high-cycle end of the spectrum, which is to be expected considering the fact that the dominant failure mode changed to sheet fracture. Since, in TPCs, multi-spot welded joints are expected to always fail from spot fracture regardless of load level, it is expected that the interrelations between layout performance in terms of fatigue life for TPCs will stay the same across the entire spectrum.

7.2. Recommendations

With regard to recommendations, first there are some practical aspects of this research that could be improved upon if the experiments were to be repeated. These are as follows:

- DIC images should be taken in a loaded condition, with a proper image in unloaded condition available for reference. This way, proper 3D strain fields can be derived.
- It was seen that there was a certain flexibility in the fatigue clamps, predominantly the upper one. As a result, some horizontal movement of the clamps was observed during cyclic loading due to the eccentricity in the applied load path. An improvement would be to increase the rigidity of the test setup.
- Initially, it was planned to use acoustic emission monitoring to capture the acoustic events relating to damage initiation and evolution. Unfortunately, this equipment was unavailable at the time of testing. It would be interesting to see if the moment of damage initiation in one or multiple spots can be captured through this data acquisition method, as this information could not be derived from other sources in this research.

During the research, some questions and gaps in existing knowledge came up that unfortunately could not yet be addressed in this thesis report. These are presented here as recommendations for future work:

- It became clear that the used welding process control strategy was sub-optimal for the large, four-spot joints created in this research. Additional research is required in order to arrive at a process control strategy that results in consistent high-quality, high-performance welds. Interesting aspects to consider in this research would be the effects of welding sequence and material warpage on weld quality and performance.
- As was mentioned before, at the evaluated load level of 70% considerable damage was already present in the column joint specimens. It would be interesting to perform these tests at a lower load level, say 30%, and evaluate if damage would still initiate in the same spot and progress in the same way as it did in this research.
- Related to this, testing at a load level of 70% prevented proper evaluation of the damage evolution through a joint from spot to spot, as after fracture of a single spot the tests would progress rapidly towards final failure when the true shear strength of the joint was exceeded. It would be interesting to test at a lower load level, artificially introduce damage in the joint, and evaluate the way in which damage progresses through the joint from spot to spot. This way, the damage-arresting potential of these joints could be properly explored.
- It was frequently observed that a change in joint stiffness, attributed to failure of a spot weld, occurred right after the test had been paused to take DIC pictures. It might be interesting to investigate if, and how, pausing the tests at regular intervals affects the obtained test results.

Bibliography

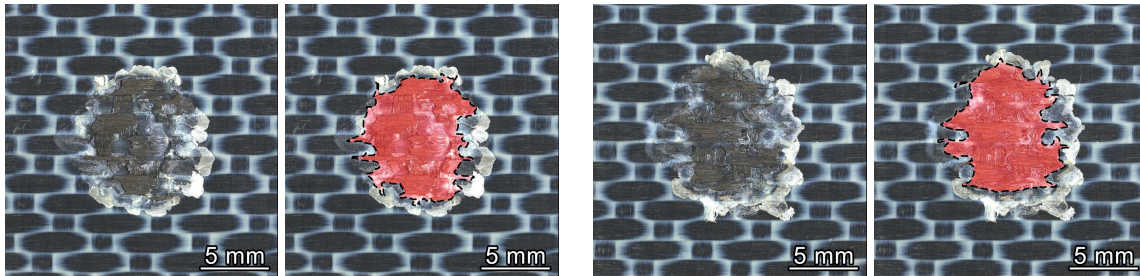
- [1] The International Council on Clean Transportation. CO₂ emissions from commercial aviation, 2018. September 2019. [Working paper] Available from: <https://theicct.org/publications/co2-emissions-commercial-aviation-2018>. [Accessed 1 October 2020].
- [2] Piquet, B. and Blumenfeld, L. A350XWB: Special edition. *Airbus Technical Magazine*, 2013.
- [3] Hale, J. Boeing 787: From the ground up. *Aero*, 2006, pp. 17–23.
- [4] Ageorges, C., Ye, L., and Hou, M. Advances in fusion bonding techniques for joining thermoplastic matrix composites: a review. *Composites: Part A*, 2001, **32**, pp. 839–857.
- [5] Yousefpour, A., Hojjati, M., and Immarigeon, J. P. Fusion bonding/welding of thermoplastic composites. *Journal of Thermoplastic Composite Materials*, 2004, **17**(4), pp. 303–341.
- [6] da Costa, A. P., Botelho, E. C., Costa, M. L., Narita, N. E., and Tarpani, J. R. A review of welding technologies for thermoplastic composites in aerospace applications. *Journal of Aerospace Technology and Management*, 2012, **4**(3), pp. 255–265.
- [7] Villegas, I. F. Ultrasonic welding of thermoplastic composites. *Frontiers in Materials*, 2019, **6**, pp. 1–10.
- [8] Thoppul, S. D., Finegan, J., and Gibson, R. F. Mechanics of mechanically fastened joints in polymer-matrix composite structures - A review. *Composites Science and Technology*, 2009, **69**(3-4), pp. 301–329.
- [9] Zeiler, T., Pfeffer, P., Kürner, M., and Münstedt, H. Improvement of adhesive bonding of thermoplastic polymers by different surface treatments. *Macromolecular Symposia*, 1997, **126**, pp. 267–281.
- [10] Jeenjitkaew, C. and Guild, F. J. The analysis of kissing bonds in adhesive joints. *International Journal of Adhesion and Adhesives*, 2017, **75**, pp. 101–107.
- [11] Hu, W., Jones, R., and Kinloch, A. J. Computing the growth of naturally-occurring disbonds in adhesively-bonded joints. In: Jones, R., Baker, A., Matthews, N., and Champagne, V. (ed.), *Aircraft Sustainment and Repair*. Elsevier Ltd., 2018, pp. 745–762.
- [12] Mitschang, P., Yousefpour, A., Villegas, I. F., Bersee, H. E., and Moser, L. Process and performance evaluation of ultrasonic, induction and resistance welding of advanced thermoplastic composites. *Journal of Thermoplastic Composite Materials*, 2012, **26**(8), pp. 1007–1024.
- [13] Hamerton, I. and Kratz, J. The use of thermosets in modern aerospace applications. In: Guo, Q. (ed.), *Thermosets: Structure, Properties, and Applications*. 2nd edition. Elsevier Ltd., 2018, pp. 303–340.
- [14] Gardiner, G. TPCs on the Boeing 787 and Airbus A350. *CompositesWorld*. May 2011. [Blog entry] Available from: <https://www.compositesworld.com/articles/tpcs-on-the-boeing-787-and-airbus-a350>. [Accessed 1 October 2020].
- [15] Mathijssen, D. Leading the way in thermoplastic composites. *Reinforced Plastics*, 2016, **60**(6), pp. 405–407.
- [16] Villegas, I. F. In situ monitoring of ultrasonic welding of thermoplastic composites through power and displacement data. *Journal of Thermoplastic Composite Materials*, 2015, **28**(1), pp. 66–85.
- [17] Ageorges, C. Experimental investigation of the resistance welding of thermoplastic-matrix composites. Part II: optimum processing window and mechanical performance. *Composites Science and Technology*, 2002, **60**(8), pp. 1191–1202.

- [18] Levy, A., Le Corre, S., and Villegas, I. F. Modeling of the heating phenomena in ultrasonic welding of thermoplastic composites with flat energy directors. *Journal of Materials Processing Technology*, 2014, **214**(7), pp. 1361–1371.
- [19] Benatar, A. and Gutowski, T. G. Ultrasonic welding of PEEK graphite APC–2 composites. *Polymer Engineering & Science*, 1989, **29**(23), pp. 1705–1721.
- [20] Zongbo Zhang, Xiaodong Wang, Yi Luo, Zhenqiang Zhang, and Liding Wang. Study on heating process of ultrasonic welding for thermoplastics. *Journal of Thermoplastic Composite Materials*, 2009, **23**(5), pp. 647–664.
- [21] Palardy, G., Shi, H., Levy, A., Le Corre, S., and Villegas, I. F. A study on amplitude transmission in ultrasonic welding of thermoplastic composites. *Composites Part A: Applied Science and Manufacturing*, 2018, **113**, pp. 339–349.
- [22] Villegas, I. F. and Palardy, G. Ultrasonic welding of CF/PPS composites with integrated triangular energy directors: melting, flow and weld strength development. *Composite Interfaces*, 2017, **24**(5), pp. 515–528.
- [23] Villegas, I. F., Grande, B. V., and Benedictus, R. A comparative evaluation between flat and traditional energy directors for ultrasonic welding. *Composite Interfaces*, 2015, **22**, pp. 717–729.
- [24] Villegas, I. F. Strength development versus process data in ultrasonic welding of thermoplastic composites with flat energy directors and its application to the definition of optimum processing parameters. *Composites Part A: Applied Science and Manufacturing*, 2014, **65**, pp. 27–37.
- [25] Zhao, T., Palardy, G., Villegas, I. F., and Benedictus, R. Towards high-quality multi-spot-welded joints in thermoplastic composite structures. *Proceedings of the 21st International Conference on Composite Materials*, 2017.
- [26] Zhao, T., Broek, C., Palardy, G., Villegas, I. F., and Benedictus, R. Towards robust sequential ultrasonic spot welding of thermoplastic composites: Welding process control strategy for consistent weld quality. *Composites Part A: Applied Science and Manufacturing*, 2018, **109**, pp. 355–367.
- [27] Zhao, T., Palardy, G., Villegas, I. F., Rans, C., Martinez, M., and Benedictus, R. Mechanical behaviour of thermoplastic composites spot-welded and mechanically fastened joints: A preliminary comparison. *Composites Part B: Engineering*, 2017, **112**, pp. 224–234.
- [28] Zhao, T., Rans, C., Villegas, I. F., and Benedictus, R. On sequential ultrasonic spot welding as an alternative to mechanical fastening in thermoplastic composite assemblies: A study on single-column multi-row single-lap shear joints. *Composites Part A: Applied Science and Manufacturing*, 2019, **120**, pp. 1–11.
- [29] Duncan, B. Developments in testing adhesive joints. In: Dillard, D. A. (ed.), *Advances in Structural Adhesive Bonding*. Woodhead Publishing Limited, 2010, pp. 389–436.
- [30] Ewalds, H. and Wanhill, R. *Fracture Mechanics*. Edward Arnold, 1984.
- [31] Dilger, K. Selecting the right joint design and fabrication techniques. In: Dillard, D. A. (ed.), *Advances in Structural Adhesive Bonding*. Woodhead Publishing Limited, 2010, pp. 295–315.
- [32] Schijve, J. *Fracture Mechanics*. Springer Science+Business Media, B.V., 2nd edition, 2009, pp. 273–275.
- [33] Hassanifard, S., Zehsaz, M., and Esmaeili, F. Spot weld arrangement effects on the fatigue behavior of multi-spot welded joints. *Journal of Mechanical Science and Technology*, 2011, **25**(3), pp. 647–653.
- [34] Hangx, R. *Disbond arrest in fibre metal laminates*. MSc Thesis, Delft University of Technology,

- 2017.
- [35] Shenoy, V., Ashcroft, I. A., Critchlow, G. W., and Crocombe, A. D. Unified methodology for the prediction of the fatigue behaviour of adhesively bonded joints. *International Journal of Fatigue*, 2010, **32**(8), pp. 1278–1288.
- [36] Bloom, L. D. *On the relationship between layup time, material properties and mould geometry in the manufacture of composite components*. PhD Thesis, University of Bristol, 2015.
- [37] Dubé, M., Hubert, P., Gallet, J. N., Stavrov, D., Bersee, H. E., and Yousefpour, A. Fatigue performance characterisation of resistance-welded thermoplastic composites. *Composites Science and Technology*, 2008, **68**, pp. 1759–1765.
- [38] De Baere, I., Van Paepegem, W., and Degrieck, J. Assessment of the interlaminar behaviour of a carbon fabric reinforced thermoplastic lap shear specimen under quasi-static and tension-tension fatigue loading. *Polymer Testing*, 2013, **32**(7), pp. 1273–1282.
- [39] Dubé, M., Chazerain, A., Hubert, P., Yousefpour, A., and Bersee, H. E. Characterization of resistance-welded thermoplastic composite double-lap joints under static and fatigue loading. *Journal of Thermoplastic Composite Materials*, 2015, **28**(6), pp. 762–776.
- [40] Rasband, W. ImageJ 1.52d. U.S. National Institutes of Health, Bethesda, Maryland, USA. 1997–2020. <https://imagej.nih.gov/ij/>.
- [41] ASTM International. *D 1002 – 10: Standard test method for apparent shear strength of single-lap-joint adhesively bonded metal specimens by tension loading (metal-to-metal)*, 2019.
- [42] Zhao, T., Palardy, G., Villegas, I. E., Rans, C., and Benedictus, R. Comparative analysis of in-plane and out-of-plane mechanical behaviour of spot-welded and mechanically fastened joints in thermoplastic composites. *Proceedings of the 17th European Conference on Composite Materials*, 2016.
- [43] Purslow, D. Matrix fractography of fibre-reinforced thermoplastics, Part 1. Peel failures. *Composites*, 1987, **18**(5), pp. 365–374.
- [44] Barbosa, L. C. M., de Souza, S. D. B., Botelho, E. C., Cândido, G. M., and Rezende, M. C. Fractographic study of welded joints of carbon fiber/PPS composites tested in lap shear. *Engineering Failure Analysis*, 2018, **93**(November 2017), pp. 172–182.

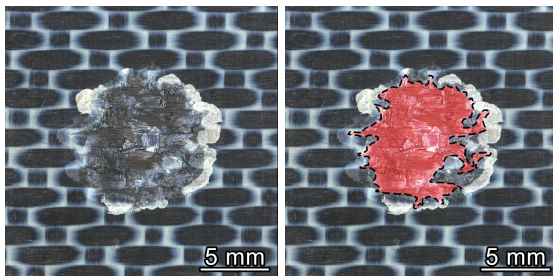
A

Fracture Surfaces and Welded Areas



s1: 55.2 mm².

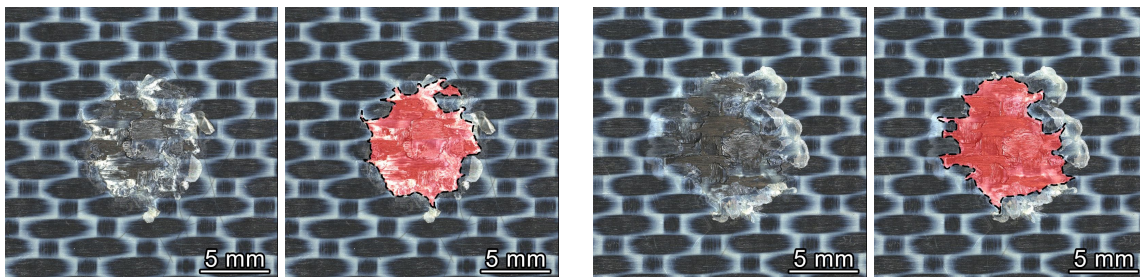
s2: 55.9 mm².



s3: 52.3 mm².

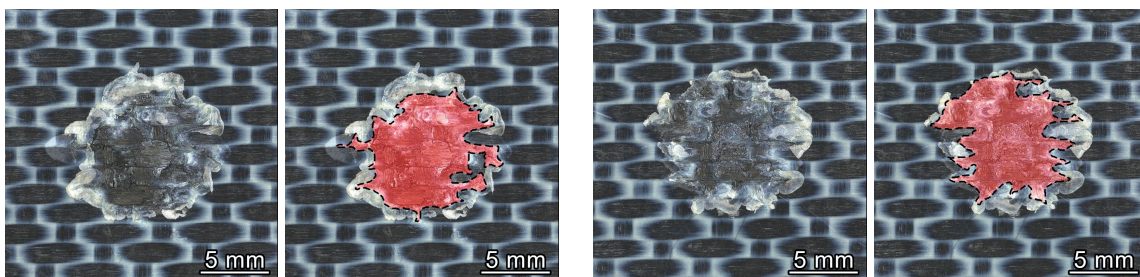
s4: 68.1 mm².

Figure A.1: Fracture surfaces and welded areas – C_SF.



s1: 47.1 mm².

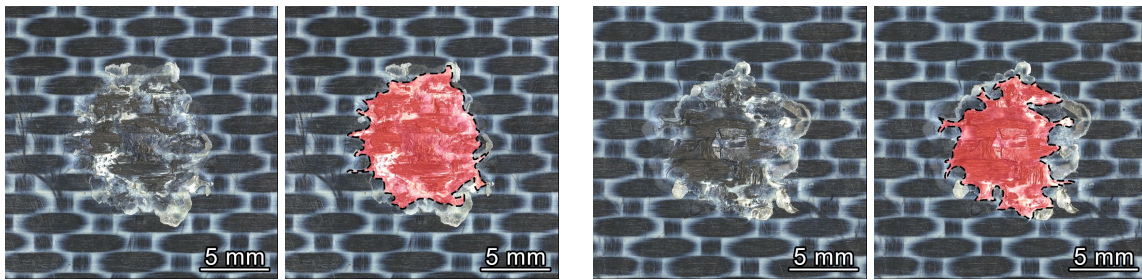
s2: 53.0 mm².



s3: 57.9 mm².

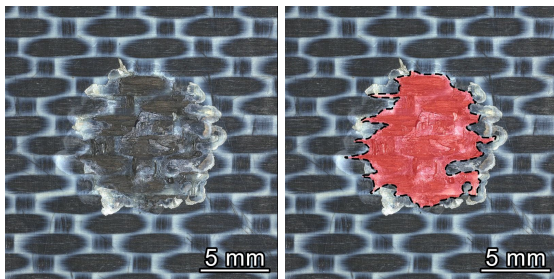
s4: 56.8 mm².

Figure A.2: Fracture surfaces and welded areas – C_FL1.



s1: 65.8 mm².

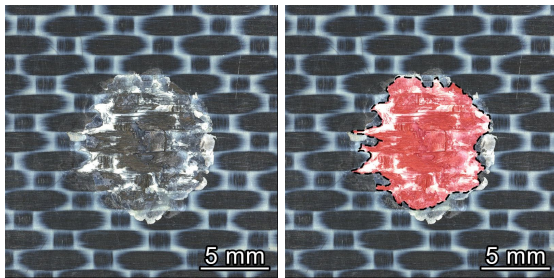
s2: 55.0 mm².



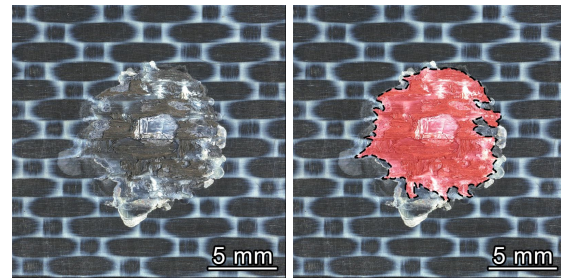
s3: 60.3 mm².

s4: 58.2 mm².

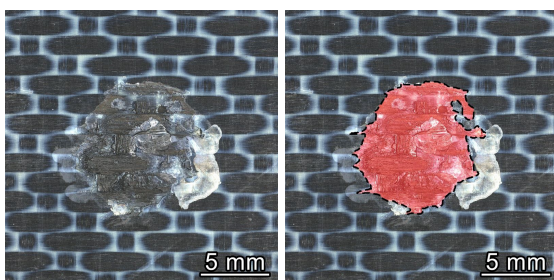
Figure A.3: Fracture surfaces and welded areas – C_FL2.



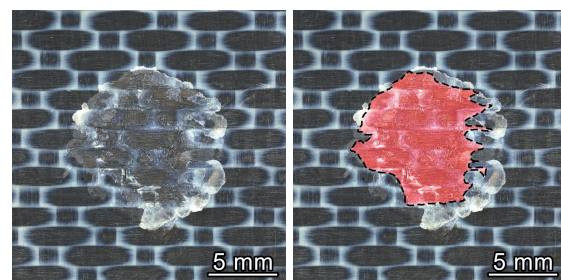
s1: 64.2 mm².



s2: 65.9 mm².

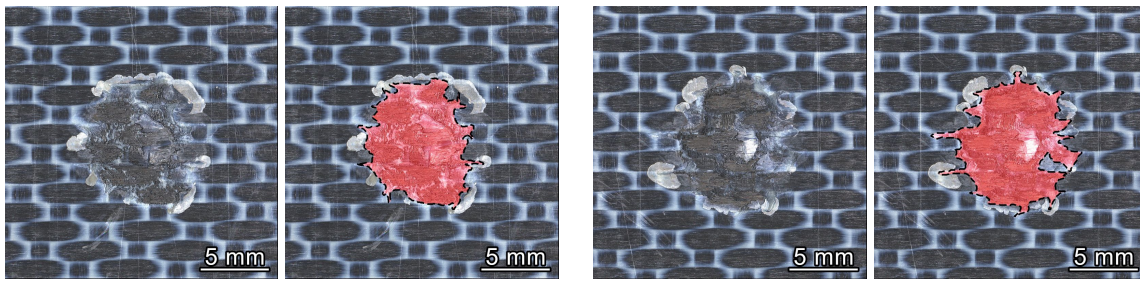


s3: 61.0 mm².



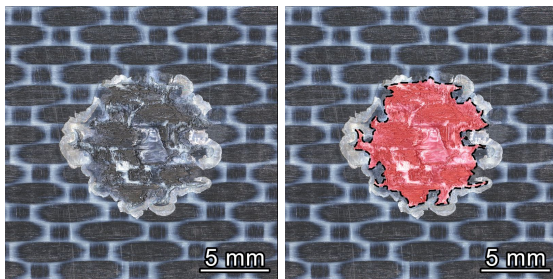
s4: 63.0 mm².

Figure A.4: Fracture surfaces and welded areas – C_FL3.



s1: 53.7 mm².

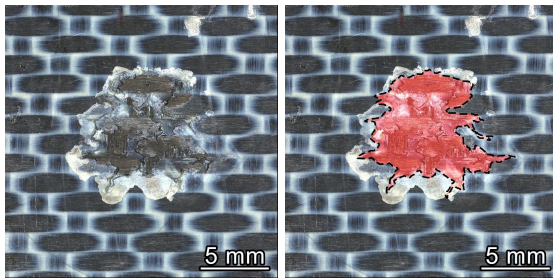
s2: 58.2 mm².



s3: 56.0 mm².

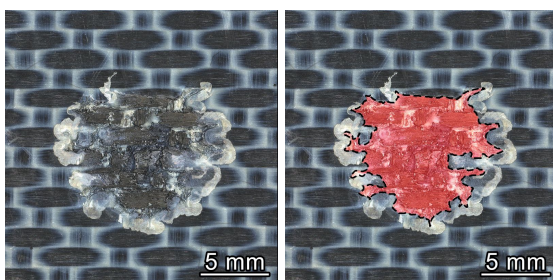
s4: 54.2 mm².

Figure A.5: Fracture surfaces and welded areas – C_FLx1.



s1: 50.4 mm².

s2: 63.5 mm².



s3: 64.5 mm².

s4: 88.9 mm².

Figure A.6: Fracture surfaces and welded areas – R_SF.

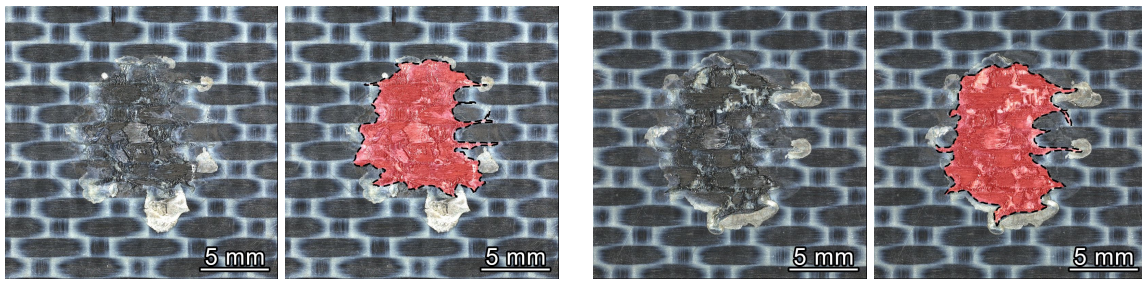
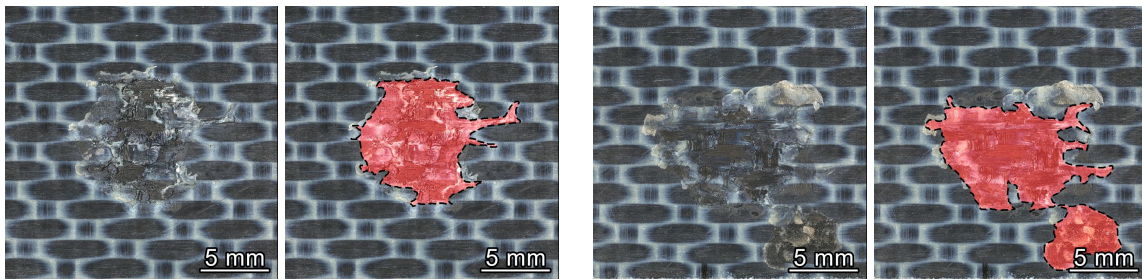
s1: 61.8 mm².s2: 68.5 mm².s3: 60.1 mm².s4: 79.7 mm².

Figure A.7: Fracture surfaces and welded areas – R_FL1.

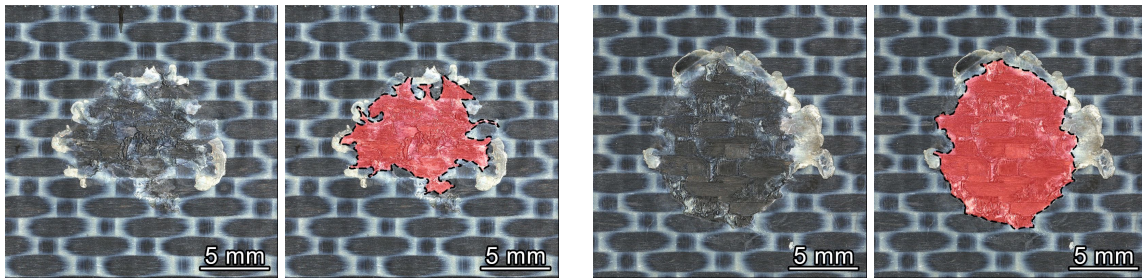
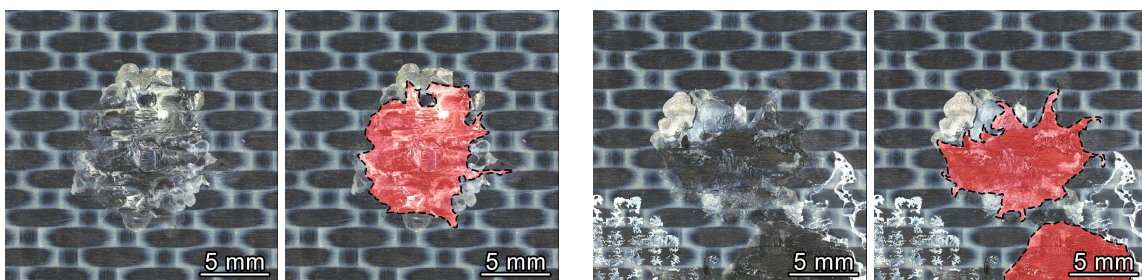
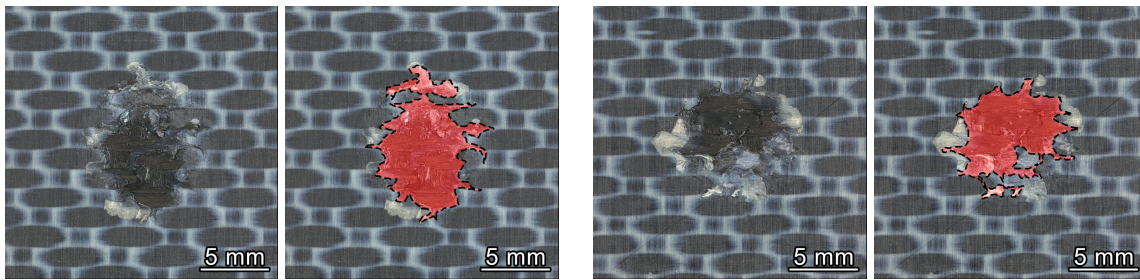
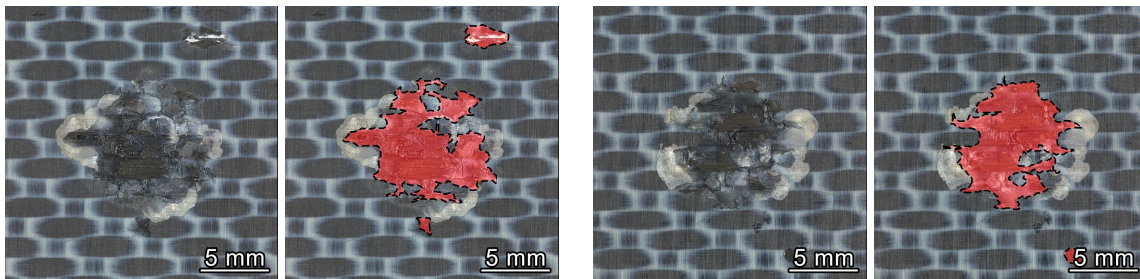
s1: 51.7 mm².s2: 88.8 mm².s3: 62.8 mm².s4: 84.9 mm².

Figure A.8: Fracture surfaces and welded areas – R_FL2.



s1: 47.8 mm².

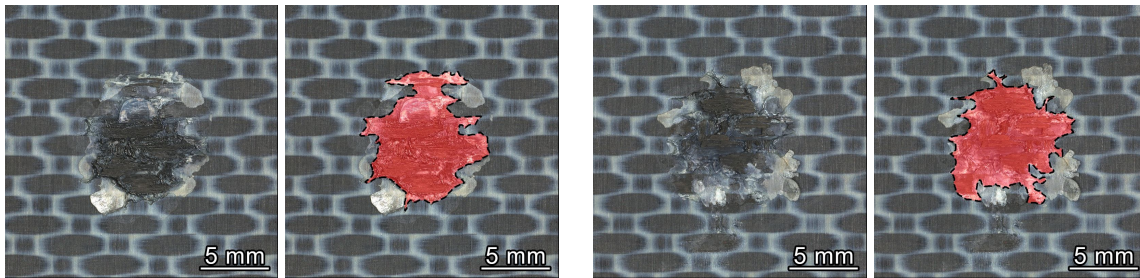
s2: 39.0 mm².



s3: 52.2 mm².

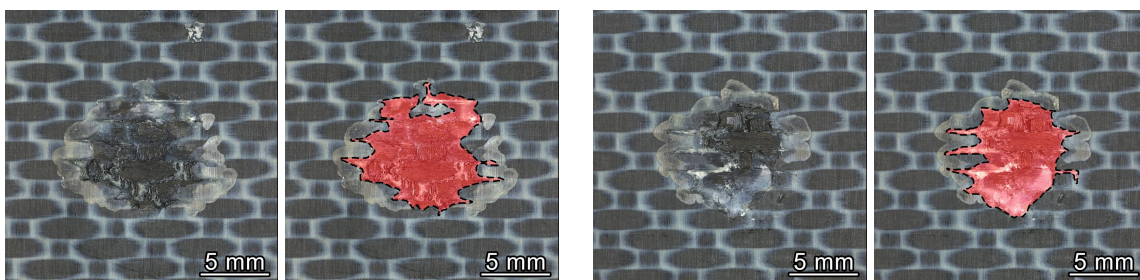
s4: 47.1 mm².

Figure A.9: Fracture surfaces and welded areas – S_SF



s1: 52.4 mm².

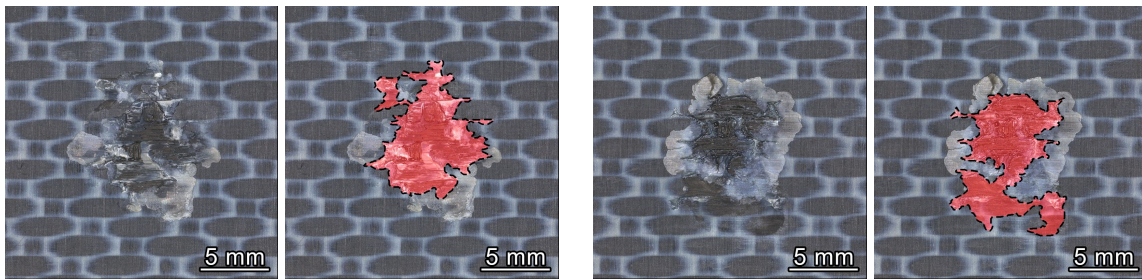
s2: 50.8 mm².



s3: 54.0 mm².

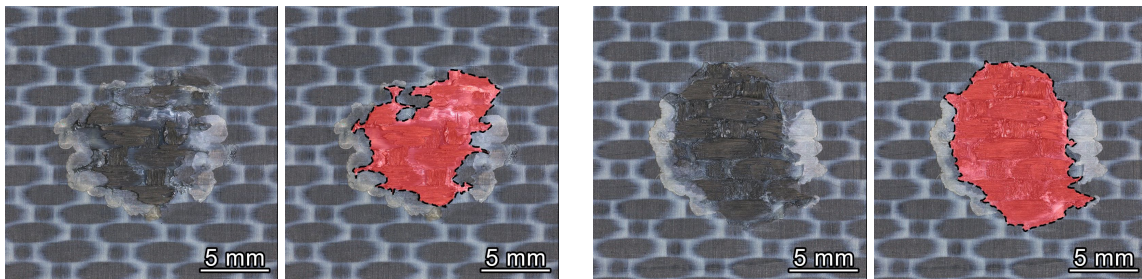
s4: 45.6 mm².

Figure A.10: Fracture surfaces and welded areas – S_FL1.



s1: 46.6 mm².

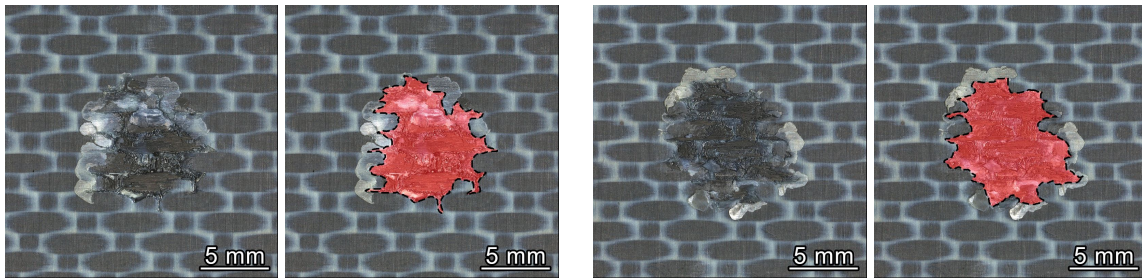
s2: 46.2 mm².



s3: 59.4 mm².

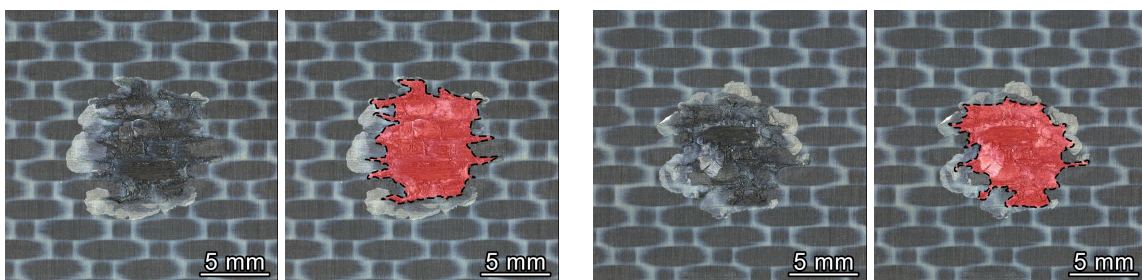
s4: 84.8 mm².

Figure A.11: Fracture surfaces and welded areas – S_FL2.



s1: 49.9 mm².

s2: 54.1 mm².



s3: 49.9 mm².

s4: 44.1 mm².

Figure A.12: Fracture surfaces and welded areas – S_FLx1.

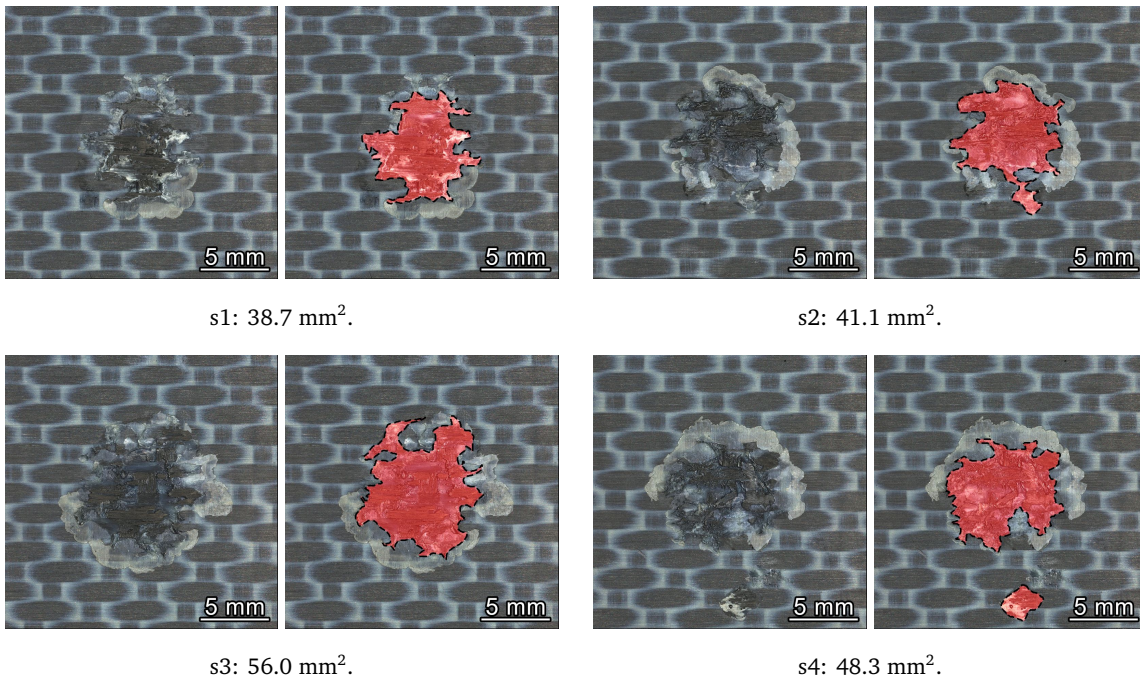


Figure A.13: Fracture surfaces and welded areas – S_FLx2.

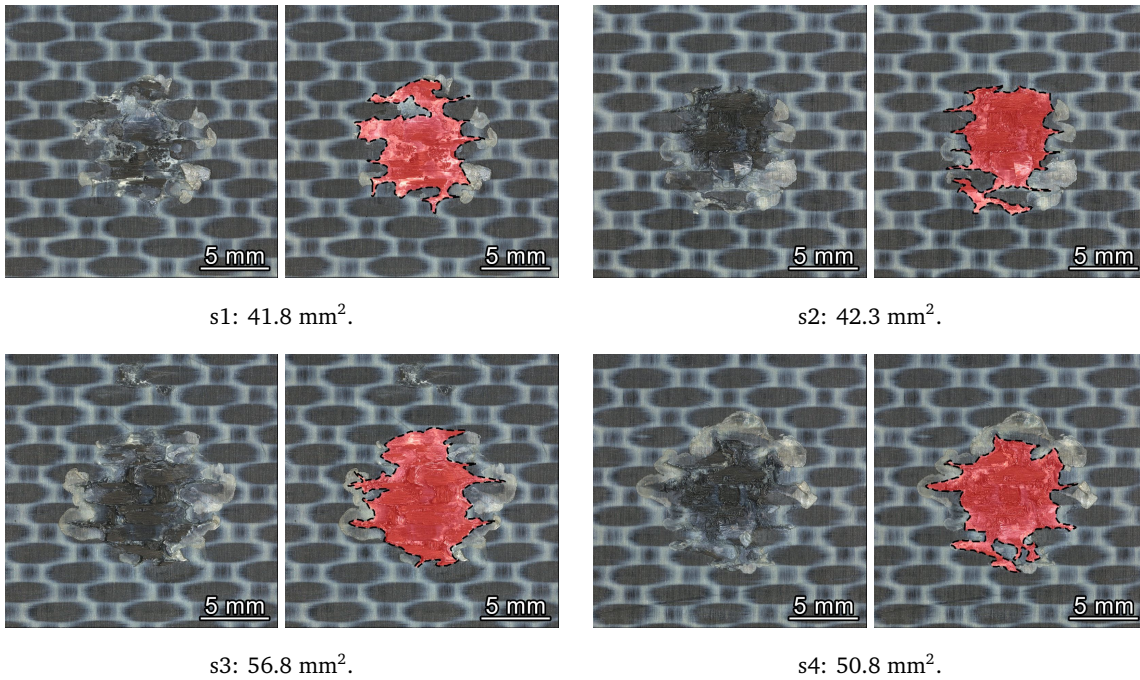


Figure A.14: Fracture surfaces and welded areas – S_TU.

B

Out-of-Plane Displacement at Spot Locations over Time

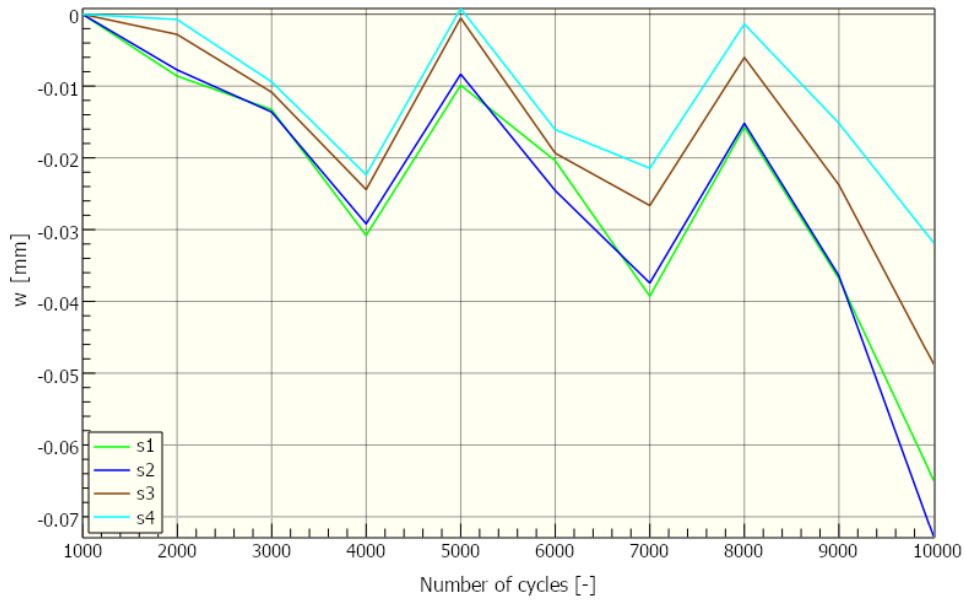


Figure B.1: Out-of-plane displacement at spot locations over time – C_FL2.

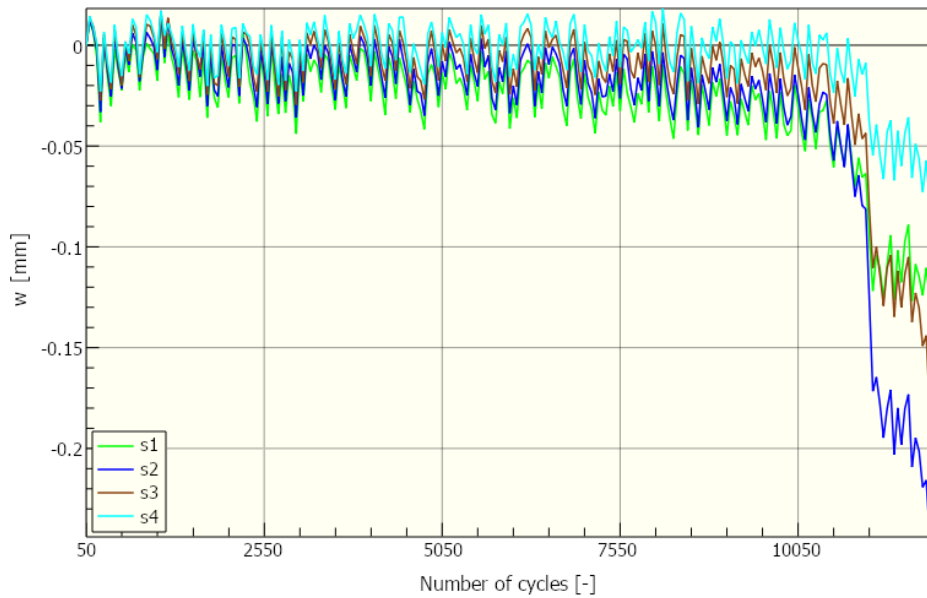


Figure B.2: Out-of-plane displacement at spot locations over time – C_FL3.

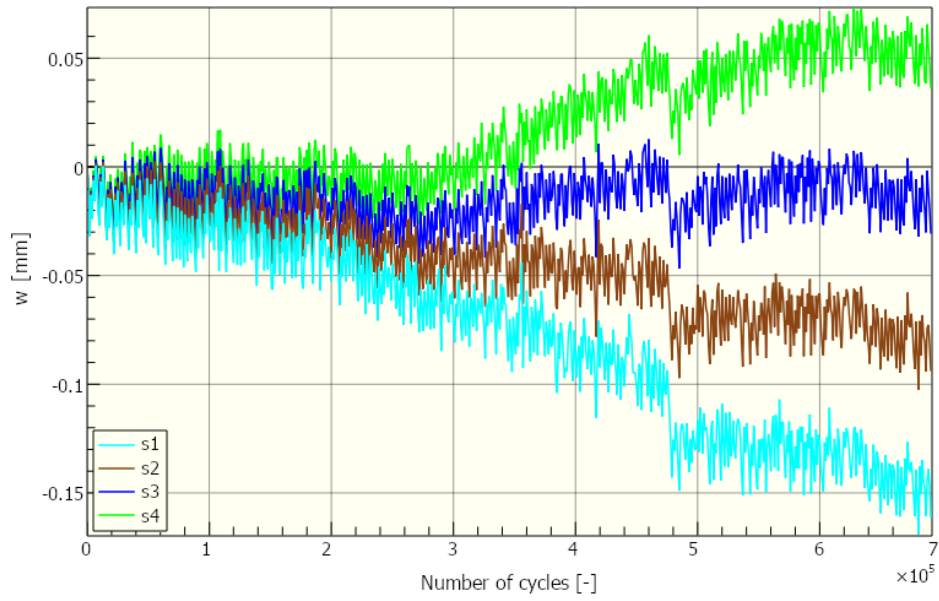


Figure B.3: Out-of-plane displacement at spot locations over time – R_FL1.

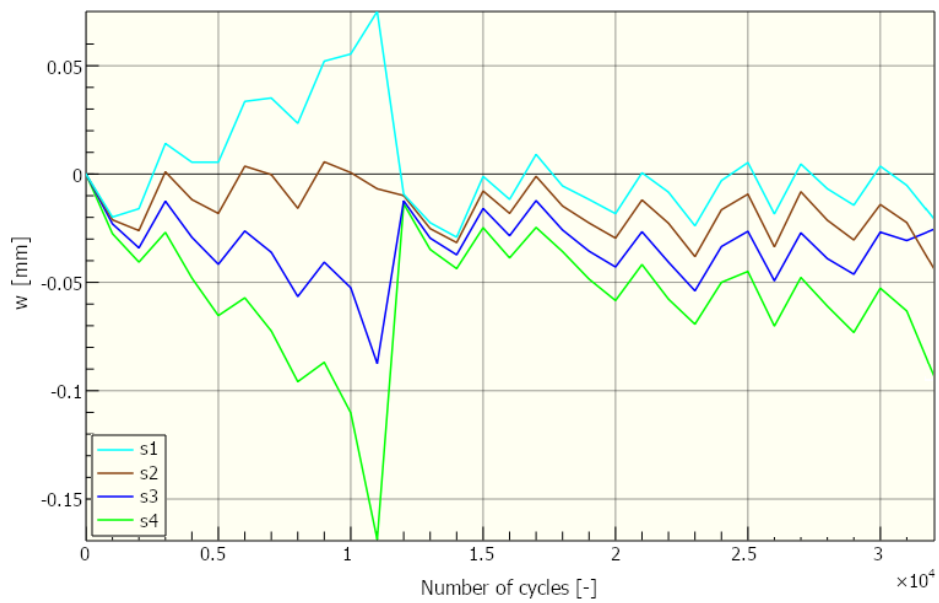


Figure B.4: Out-of-plane displacement at spot locations over time – R_FL2.

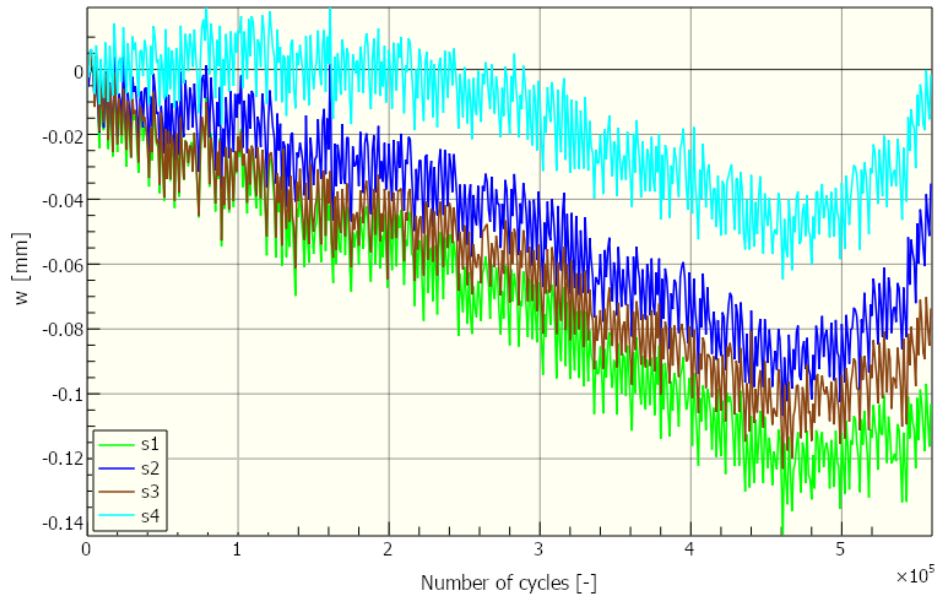


Figure B.5: Out-of-plane displacement at spot locations over time – S_FL1.

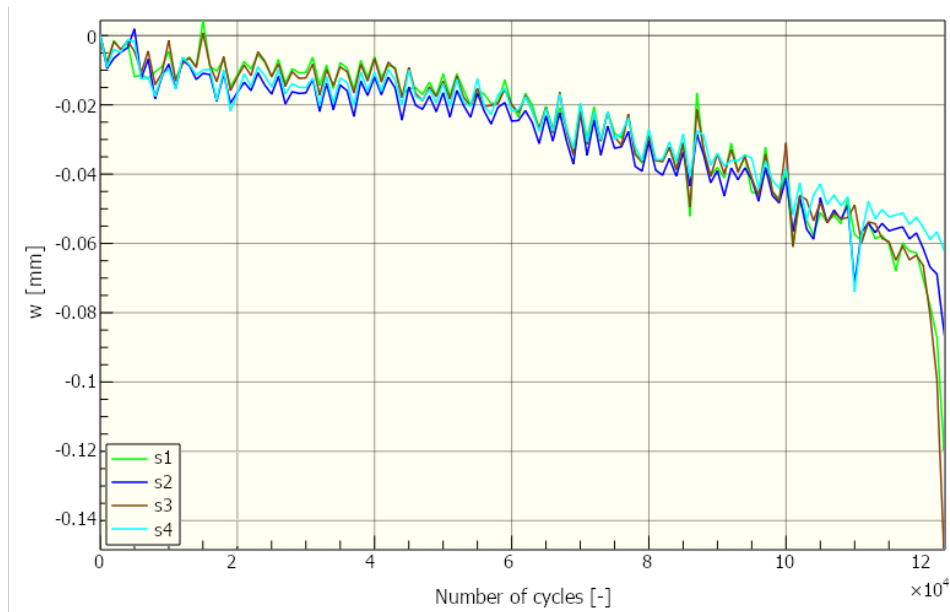


Figure B.6: Out-of-plane displacement at spot locations over time – S_FL2.